NUCLEOSYNTHESIS IN EXPLOSIVE ENVIRONMENTS: NEUTRON STAR MERGERS AND CORE-COLLAPSE SUPERNOVAE

Inauguraldissertation

zur

Erlangung der Würde eines Doktors der Philosophie
vorgelegt der
Philosophisch–Naturwissenschaftlichen Fakultät
der Universität Basel

von

Marius Andreas Eichler

aus Basel, BS

Darmstadt, 2017

Genehmigt von der Philosophisch-Naturwissenschaftlichen Fakultät

auf Antrag von

Prof. Dr. Friedrich-Karl Thielemann, Prof. Dr. Stefan Rosswog

Basel, den 22. März 2016

Prof. Dr. Jörg Schibler

There is a theory that if ever anybody discovers exactly what
the Universe is for and why it is here, it will instantly disappear
and be replaced by something even more bizarre and inexplicable.
There is another theory which states that this has already happened.
– Douglas Adams, *"The hitchhiker's guide to the galaxy"*

Abstract

Several nucleosynthesis processes are responsible for the production of the chemical elements in the universe. Explosive ejecta in core-collapse supernovae typically produce intermediate-mass elements up to the iron-group nuclei, although the exact compositions depend on the parameters of the supernova, such as the structure of the pre-supernova progenitor, the explosion energy and neutrino luminosities. Understanding the connection between these parameters and the nuclear composition of the ejecta is an ongoing field of research in nuclear astrophysics. Open questions also remain surrounding the late-time ejecta (*the neutrino-driven wind*), which could host either a weak r-process or the *ν*p-process.

Research on the *rapid neutron-capture process* requires the knowledge of the properties of exotic nuclei far from stability. Since these nuclei cannot be produced under laboratory conditions, we have to rely on theoretical predictions (e.g., mass models), introducing large uncertainties. In addition, the astrophysical environment of the r-process is still unknown, although recent observational data support mergers of two neutron stars as a promising site. Furthermore, observations of metal-poor stars enriched with r-process material suggest a robust abundance pattern for the strong r-process, which provides a solid benchmark to test our models against.

In this thesis, several aspects of explosive nucleosynthesis are studied. In the first part, the theoretical framework of nucleosynthesis calculations is discussed, with a focus on the r-process and fission reactions. The second part highlights the role of fission on r-process calculations. Finally, we report on nucleosynthesis calculations for core-collapse supernova models, on the one hand in spherical symmetry in order to contrain the so-called PUSH method, as well as in axisymmetric models.

II

Contents

Acknowledgments

I am grateful to the following persons, who all contributed to this thesis in one way or another:

- F.-K. Thielemann for giving me the opportunity to work in his group and encouraging (and enabling) me to go to many interesting conferences and meetings.
- Almudena Arcones, Gabriel Martínez-Pinedo, Igor Panov, Oleg Korobkin, Stephan Rosswog, Matthias Hempel, Albino Perego, Carla Fröhlich, Ko Nakamura, Tomoya Takiwaki, and Kei Kotake for valuable work-related advice and collaborations.
- Kevin Ebinger for PUSHing hard.
- Julia Reichert, Kevin Ebinger, Benjamin Wehmeyer and Maik Frensel for proof-reading parts of this thesis.
- The Basel Postdocs Matthias Hempel, Ruben Cabezón, Takami Kuroda, Andreas Lohs, Kuo-Chuan Pan, Nobuya Nishimura, Marco Pignatari, Assistant Professors Thomas Rauscher and Matthias Liebendörfer as well as visiting scientists Igor Panov and Nils Paar for advice and a good atmosphere in the group.
- My officemates Kevin Ebinger, Julia Reichert, Maik Frensel, Benjamin Wehmeyer, Albino Perego, Christian Winteler, Roger Käppeli for work-related and -unrelated talks and many coffee breaks.
- All other Basel PhD students past or present Oliver Heinimann, David Gobrecht, Umberto Battino, Chiara Biscaro, Sofie Fehlmann, Arkaprabha Sarangi.
- My parents Norbert and Gabriele, my brother Alexander and my sister Martina for support and being a great family.
- My godchild Livia (* 12.2.2016) and nephew Thierry (* 13.1.2016) for being cute and making me smile.
- My dear girlfriend Helen for her understanding, support and affection.
- Everyone else who I might have forgotten (sorry!).

Chapter 1

Introduction

The four fundamental forces in our universe are gravity, the electromagnetic force, the weak force and the strong force. Although they operate at very different scales, both in terms of coupling strengths and distances, they are all brought together in the field of nuclear astrophysics: For instance, gravity is the driving force behind stellar core collapse (the stage immediately preceding a core-collapse supernova) and the reason for the energy loss of binary neutron star systems via emission of gravitational waves, ultimately leading to a collision of the two neutron stars. The strong force is highly attractive but only operates on extremely small distances, enabling the formation and existence of hadrons and nuclei of higher complexity. In a fissioning nucleus, the electromagnetic Coulomb repulsion between protons becomes too strong for the strong force to counteract, and the nucleus splits into fragments. It is also responsible for the potential barrier in reactions between charged particles. Finally, nuclear β-decays and interactions with leptons have a lasting effect on nuclear compositions and are described by the weak force.

One of the main goals of nuclear astrophysics is to explain the elemental and isotopic compositions observed in stars. Of course, the abundance distribution of the solar system is particularly well studied, and we understand that it is the result of a complicated interplay of different nuclear processes that occurred in our galactic neighbourhood before the sun was born. Since the elements around iron are the tightest bound elements, the synthesis of the heavier elements with $Z > 28$ is non-trivial and their origin is of special interest. The production of the majority of these elements are attributed to two nucleosynthesis processes: the slow (s-) and the rapid (r-) neutron capture process. Due to its nature, the s-process reaction path proceeds along the stable nuclei in the nuclear chart. Therefore, the nuclei that are involved are well studied, and the biggest remaining challenge surrounding it is the supply of free neutrons over a large enough period of time. R-Process studies require the knowledge of nuclear properties far from stability, where no experimental

data are available. This means that theoretical predictions of nuclear masses and reaction rates have to be used. In addition, the astrophysical sites of the r-process have not yet been found, all of which means that r-process calculations are still bearing large uncertainties, both from the nuclear and the hydrodynamical side. Within the scope of this thesis, we address some of these uncertainties and explore the sensitivities of our results to some aspects of nuclear theory.

In Chapter 2 we will discuss the ingredients for nuclear networks, the computational tools utilized in nucleosynthesis calculations, with a chapter dedicated to nuclear mass models. Chapter 3 will give a short overview on Galactic Chemical Evolution, the study of stellar compositions and their change in time due to (explosive) nuclear processes.

One main focus of this thesis lies on the r-process. Its operating mechanism will be discussed in chapter 4. Moreover, possible astrophysical sites will be introduced and briefly discussed, before moving on to the description of fission and its treatment in nuclear networks in chapter 5. After covering these points, we will be able to tackle the issues connected with neutron star mergers as a probable r-process site (chapter 6). In chapter 7 we will present our results from nucleosynthesis calculations in core-collapse supernovae (in both spherical symmetry and multi-D simulations), the second main focus of this thesis. Finally, we will end with a summary and some conclusive remarks in chapter 8.

Chapter 2

Nuclear Networks

The origin of chemical elements and their isotopes is an issue that has kept astrophysicists busy for centuries. As of today, we know that a complex interplay of many different nucleosynthesis processes have been operating at various stages and environments in our universe. Our understanding of these processes (and their working sites) continually grows, not least because of our efforts to develop theoretical models and learn from the comparison of our results to observations. This chapter gives a short overview on the theoretical description of nuclear reactions and their implementation into a *nuclear network*, a tool that can be used for nucleosynthesis calculations. For more detailed explanations see, e.g., Iliadis (2007); Cowan et al. (in preparation).

2.1 Towards a Nuclear Network – Nuclear Reaction Rates

2.1.1 Transmission probabilities

Forces generated by nucleons and nuclei are usually described by potential fields, where the gradient of the potential is equal to the vector force. When a particle hits a potential barrier (e.g., a nucleus), it can either overcome the potential (corresponding to forming a compound state in a nuclear reaction) or be reflected by it. In a classical treatment these two cases can easily be distinguished by comparing the energy of the particle E with the height of the potential barrier V:

$$\begin{aligned} E > V &\longrightarrow \text{penetration} \\ E < V &\longrightarrow \text{reflection}\,. \end{aligned} \tag{2.1.1}$$

In quantum mechanics, however, there is a possibility for penetration even when $E < V$ or for reflection when $E > V$ (even though it is exponentially decreasing).

In nuclear physics, it is therefore necessary to define a transmission coefficient that describes the penetration probability. Considering a particle beam hitting a target, it can be defined as the ratio of the outgoing and ingoing plane wave fluxes:

$$T = \frac{k_f |\phi_f|^2}{k_i |\phi_i|^2} \,, \tag{2.1.2}$$

where k_f, k_i are the wave numbers ($k_{f,i} = \sqrt{2m_{f,j}E_{f,i}}/\hbar$) and ϕ_f, ϕ_i are the wave functions of the outgoing (f) wave and the initial (i) wave, respectively. Considering a central collision of a neutron with energy E and a nucleus with a simple one-dimensional square well-potential, continuity requirements at the edge of the potential lead to

$$T = \frac{4k_i k_f}{|k_i + k_f|^2} \approx \frac{4k_i}{k_f} \,. \tag{2.1.3}$$

The last relation comes from the fact that in a nuclear reaction, $k_f > k_i$ due to the large negative potential within the nucleus. Note that equation (2.1.3) is only valid for neutrons. Charged particles will have to overcome a Coulomb potential first, leading to the expression

$$\begin{aligned} T &= \exp(-2\pi\eta) \,, \text{ where} \\ \eta &= \left(\frac{m}{2E}\right)^{1/2} \frac{Z_1 Z_2 e^2}{\hbar} \end{aligned} \tag{2.1.4}$$

is the so-called *Sommerfeld parameter*. The mass and energy of the projectile are denoted as m and E, while Z_1 and Z_2 are the charge numbers of the nucleus and the projectile, respectively. A detailed derivation of equation (2.1.4) can be found for example in Iliadis (2007). Note that these expressions are only valid for central collisions, i.e., without any transfer of angular momentum.

2.1.2 The nuclear cross section

When a projectile particle hits a target particle (here we assume the target particle is at rest), there is a possibility that a nuclear reaction occurs. The probability for an occurrence of the reaction depends on many factors, as we will see later. As a starting point, we define the cross section as follows:

$$\sigma = \frac{\text{number of reactions per target per second}}{\text{flux of projectile particles}} \,. \tag{2.1.5}$$

In the following, we will focus on possibilities to theoretically predict the nuclear cross section. It can be shown that the cross section for the production of a compound nucleus is the sum of transmission coefficients over all possible angular

momenta l:

$$\sigma = \frac{\pi}{k^2} \sum_{l}^{\infty} (2l + 1) T_l \,. \tag{2.1.6}$$

The wave number k is that of the incoming projectile particle. For target and projectile particles with spins I_i and I_j, we can define the channel spin $\vec{S} = \vec{I_i} + \vec{I_j}$, with possible values ranging from $|I_i - I_j|$ to $I_i + I_j$. The number of allowed channel spin orientations is equal to the product of the individual spin orientations, i.e.,

$$\sum_{S=|I_i-I_j|}^{I_i+I_j} (2S + 1) = (2I_i + 1)(2I_j + 1) \,. \tag{2.1.7}$$

If target and projectile are identical particles, only even channel spins are allowed, i.e., the amount of possible orientations are halved. We therefore include a factor $(1 + \delta_{ij})$, such that the Eq. (2.1.7) becomes

$$\sum_{S=|I_i-I_j|}^{I_i+I_j} (2S + 1) = \frac{(2I_i + 1)(2I_j + 1)}{1 + \delta_{ij}} \,. \tag{2.1.8}$$

The channel spin and the angular momentum determine the spin J of the compound nuclear state ($\vec{J} = \vec{S} + \vec{l}$). By replacing the summation over l in Eq. (2.1.6) with a sum over J, we can write for the cross section

$$\begin{aligned} \sigma &= \frac{\pi}{k^2} \sum_{J} \sum_{S=|I_i-I_j|}^{I_i+I_j} \sum_{l=|J-S|}^{J+S} \frac{(2J_n + 1)(1 + \delta_{ij})}{(2I_i + 1)(2I_j + 1)} T_{lS}(E) \\ &= \frac{\pi}{k^2} \sum_{J} \frac{(2J_n + 1)(1 + \delta_{ij})}{(2I_i + 1)(2I_j + 1)} \sum_{S=|I_i-I_j|}^{I_i+I_j} \sum_{l=|J-S|}^{J+S} T_{lS}(E) \\ &= \frac{\pi}{k^2} \sum_{J,\pi} \frac{(2J_n + 1)(1 + \delta_{ij})}{(2I_i + 1)(2I_j + 1)} T(E, J, \pi) \,. \end{aligned} \tag{2.1.9}$$

The factor $(1 + \delta_{ij})/(2I_i + 1)(2I_j + 1)$ is needed to ensure that the cross section is the average over all possible initial spin states of target and projectile. In the last transformation we replaced the sums over all T_{lS}, i.e., the transmission coefficients for all possible spin and angular momentum configurations, with one total transmission coefficient $T(E, J, \pi)$, which describes the probability to produce the compound nuclear state with energy E, spin J, and parity π.

2.1.3 Resonances

In a two-body reaction $i + j$, a compound nucleus in an excited state is formed, which after a short time decays into the end products $o + m$. The probability for

the reaction to occur is a function of the energy of the incoming particle and also depends on the positions of the excited states in the compound nucleus. In other words, if the total energy of the particle-target system matches the energy level of an excited state in the compound nucleus, the probability for the reaction to take place can increase by several orders of magnitude. This phenomenon is called *resonance*.

In a quantum-mechanical description, each excited state has a certain energy width against decay Γ, which is a measure of the state's stability against decay. The energy width of the state and the lifetime of the compound nucleus τ are connected via the Heisenberg uncertainty principle, $\Gamma = \hbar/\tau$. Often, the nucleus can decay via different decay channels (e.g., deexcitation via γ- or neutron emission). In this case the total width of the resonance state n is given by the sum of all the individual partial widths:

$$\Gamma_n = \Gamma_a + \Gamma_b + ... \tag{2.1.10}$$

Therefore, an energy width $f(E)$ can be associated with each state:

$$f(E) = \frac{\Gamma_n^2}{(E - E_n)^2 + (\Gamma_n/2)^2}\,, \tag{2.1.11}$$

where E_n is the mean energy of the state. The resonance cross section can now be constructed based on the following considerations:

- the closer the energy of the incoming particles to the resonance energy E_n, the larger the cross section: $\sigma \propto f(E)$
- the probability to produce the exact compound state is $\Gamma_{j,n}/\Gamma_n$
- the probability for the compound nucleus to decay into the products $o + m$ is $\Gamma_{o,n}/\Gamma_n$
- the theoretical upper limit to the nuclear reaction cross section is (see Eq. (2.1.9))

  $$\sigma = \frac{\pi}{k^2}\frac{(2J_n + 1)(1 + \delta_{ij})}{(2I_i + 1)(2I_j + 1)}\,, \tag{2.1.12}$$

  where k is the wave number of the projectile, J_n is the total angular momentum of the compound state, and I_i and I_j are the total angular momenta of the target and projectile nuclei, respectively.

This leads to the *Breit-Wigner* resonance formula:

$$\sigma_{i,n}(j,o) = \frac{\pi}{k^2}\frac{(2J_n+1)(1+\delta_{ij})}{(2I_i+1)(2I_j+1)}\frac{\Gamma_{j,n}\Gamma_{o,n}}{(E-E_n)^2+(\Gamma_n/2)^2}\,. \tag{2.1.13}$$

Most resonances are so narrow that the $(E-E_n)^2$ term in the denominator effectively acts as a delta function around the resonance energy E_n.

2.1.4 Hauser-Feshbach Theory

At low energies, a single resonance can dominate the transition probabilities completely. Knowledge of the low-energy resonances is therefore very important. At higher excitation energies, however, the level density in the compound nuclei is usually much larger and resonances become broader and more frequent. Single resonances can even overlap, causing the cross section to appear as a smooth function of energy. In this case, a good description of the averaged cross section can be achieved by a statistical approach, e.g., the *Hauser-Feshbach* Theory (Gadioli & Hodgson, 1992), which is based on the assumption that the formation of the compound nucleus and its decay are independent from each other. Cross sections derived by this model have the form

$$\sigma^{HF} = \sigma_{form} b_{dec}\,, \tag{2.1.14}$$

where σ_{form} is the cross section for the formation of the compound nucleus, and b_{dec} is the branching ratio for the specific decay channel. The cross section for the formation of the compound nucleus is given by Equation (2.1.9):

$$\sigma_{form}(E) = \frac{\pi}{k^2}\frac{1+\delta_{ij}}{(2I_i+1)(2I_j+1)}\sum_{J,\pi}(2J_n+1)T_j(E,J,\pi)\,. \tag{2.1.15}$$

The branching probability for the decay channel o is $b_{dec} = T_o/T_{tot}$, where T_{tot} is the sum over all possible decay channels. This leads to the Hauser-Feshbach formula:

$$\sigma^{HF} = \frac{\pi}{k^2}\frac{(1+\delta_{ij})}{(2I_i+1)(2I_j+1)}\sum_{J,\pi}(2J_n+1)\frac{T_j(E,J,\pi)T_o(E,J,\pi)}{T_{tot}(E,J,\pi)} \tag{2.1.16}$$

2.1.5 The S-factor

Charged particle reaction cross sections are highly energy-dependent due to the Coulomb repulsion of the reacting nuclei. In particular, they drastically drop to very low values at low energies. This makes comparisons of theoretical and experimental values very difficult, since small uncertainties in the nuclear structure can translate to large uncertainties in the theoretical derivation of nuclear cross sections. At low energies, central collisions with no angular momentum transfer are dominant ($l = 0$ for the incoming projectiles). In this case, the transmission coefficient (for charged particle reactions) is $T_{l=0} = e^{-2\pi\eta}$ (see section 2.1.1). Thus, we get for the cross section

$$\sigma = \frac{\pi}{k^2} T_{l=0} = \frac{\pi}{k^2} e^{-2\pi\eta} = \frac{\hbar^2 \pi}{2\mu E} e^{-2\pi\eta} \,. \tag{2.1.17}$$

Note that we are using center-of-mass coordinates, thus μ is the reduced mass of the projectile-target system and E is the center-of-mass energy. In this case, the *astrophysical S-factor*, defined as $S(E) = \sigma(E) E e^{2\pi\eta}$, is a constant. Moreover, it varies much less with energy than the cross section also at higher energies, making it a useful tool for theoretical extrapolations to low and high energies. The cross section can then be written in the form

$$\sigma(E) = \frac{S(E)}{E} e^{2\pi\eta} \,. \tag{2.1.18}$$

2.1.6 Velocity integrated cross section

Let us consider a reaction $i + j \rightarrow o + m$, where the nuclei i and j react to produce the nuclei o and m. If we denote the number densities of particles i and j as n_i and n_j, respectively, we can rewrite Eq. 2.1.5 as

$$\sigma = \frac{r/n_i}{n_j v} \,. \tag{2.1.19}$$

Here v is the relative velocity between the projectile j and the target i, $|\vec{v_i} - \vec{v_j}|$, and r is the *reactivity* (i.e., number of reactions per volume and time, usually in $cm^{-3}\,s^{-1}$). In reality, nuclei in an astrophysical plasma do not all have the exact same (kinetic) energy, but their energies instead follow a Maxwell-Boltzmann distribution, and therefore the number densities n_i & n_j have to be replaced by the expressions

$$\begin{aligned} dn_x &= n_x \frac{4\pi p_x^2}{(2\pi m_x kT)^{3/2}} \exp\left(-\frac{p_x^2}{2m_x kT}\right) dp_x \\ &= n_x \left(\frac{m_x}{2\pi kT}\right)^{3/2} \exp\left(-\frac{m_x v_x^2}{2kT}\right) d^3 v_x \\ &= n_x \phi(\vec{v}_x) d^3 v_x \,. \end{aligned} \tag{2.1.20}$$

Rewriting Eq. (2.1.19) and using (2.1.20) we get for the number of reactions in $cm^{-3}s^{-1}$

$$\begin{aligned} r_{i;j} &= n_i n_j \int \sigma(|\vec{v}_i - \vec{v}_j|)|\vec{v}_i - \vec{v}_j| \phi(\vec{v}_i)\phi(\vec{v}_j) d^3 v_i d^3 v_j \\ &= n_i n_j \langle \sigma v \rangle_{i;j} \,. \end{aligned} \tag{2.1.21}$$

If the projectile particle species is identical to the target species, a factor of $1/2$ has to be introduced in order to avoid double counting:

$$r_{i;i} = \frac{n_i^2}{2} \langle \sigma v \rangle_{i;i} \quad , \tag{2.1.22}$$

leading to the general expression

$$r_{i;j} = \frac{n_i n_j \langle \sigma v \rangle_{i;j}}{1 + \delta_{ij}} \,. \tag{2.1.23}$$

The term $\langle \sigma v \rangle_{i;j}$ is the velocity integrated cross section. A better understanding of its meaning can be obtained by replacing the individual coordinates of particles i and j with center-of-mass and relative coordinates. To that end, we introduce the center-of-mass velocity $\vec{V}$ and the relative velocity $\vec{v}$ as follows:

$$\begin{aligned} \vec{V} &= \frac{m_i \vec{v}_i + m_j \vec{v}_j}{M} \,, \\ \vec{v} &= \vec{v}_i + \vec{v}_j \,. \end{aligned} \tag{2.1.24}$$

The total kinetic energy E of the system can be written as

$$E = \frac{m_i v_i^2}{2} + \frac{m_j v_j^2}{2} = \frac{1}{2} M V^2 + \frac{1}{2} \mu v^2 \,. \tag{2.1.25}$$

Here $M = m_i + m_j$ is the total mass and $\mu = (m_i m_j)/(m_i + m_j)$ is the reduced mass of the two-particle system. The velocity distributions can now be expressed as follows:

$$\phi(\vec{v}_i)\phi(\vec{v}_j) = \frac{(M\mu)^{3/2}}{(2\pi kT)^3} \exp\left(-\frac{MV^2 + \mu v^2}{2kT}\right) . \tag{2.1.26}$$

Finally this leads to

$$\begin{aligned} \langle\sigma v\rangle &= \int \sigma(v) v \left(\frac{\mu}{2\pi kT}\right)^{3/2} \exp\left(-\frac{\mu v^2}{2kT}\right) d^3v \\ &= \left(\frac{8}{\mu\pi}\right)^{1/2} \frac{1}{(kT)^{3/2}} \int_0^\infty E\sigma(E) \exp\left(-\frac{E}{kT}\right) dE . \end{aligned} \tag{2.1.27}$$

The last transformation follows from using the relations $d^3v = 4\pi v^2 dv$ and $E = \mu v^2/2$ (assuming that the center of mass of the system is in rest; $\vec{V} = 0$). In this final form, it becomes obvious that $\langle\sigma v\rangle$ is only dependent on the temperature T.

Between the cross section of a reaction $i(j, o)m$ and its inverse (backwards) reaction $m(o, j)i$ a relation can be found using the Hauser-Feshbach formalism (see equation (2.1.16)):

$$\frac{\sigma_i(j, o)_J}{\sigma_m(o, j)_J} = \frac{1 + \delta_{ij}}{1 + \delta_{om}} \frac{(2I_o + 1)(2I_m + 1)}{(2I_i + 1)(2I_j + 1)} \frac{k_o^2}{k_j^2} , \tag{2.1.28}$$

where the subscript J denotes a single populated state in the compound nucleus with spin J. Equation (2.1.28) is also known as the principle of *detailed balance*. As this relation holds true for all individual states in the compound nucleus, we easily obtain an expression for the total cross sections at energies E_{ij} and E_{om}, where $E_{ij} = E_{om} + Q_{o,j}$ with $Q_{o,j}$ being the Q-value of the reaction $m(o, j)i$:

$$\frac{\sigma_i(j, o; E_{ij})}{\sigma_m(o, j; E_{om})} = \frac{1 + \delta_{ij}}{1 + \delta_{om}} \frac{g_o g_m}{g_i g_j} \frac{k_o^2}{k_j^2} . \tag{2.1.29}$$

The $g_x = 2I_x + 1$ are the ground state degeneracy factors. In an astrophysical plasma, g_i and g_m have to be replaced by $G_x = \sum_n g_{x,n} \exp(-E_n/kT)$, the so-called partition functions, which also account for thermally populated excited states n (see Fowler et al. 1967). Equations (2.1.27) and (2.1.29) lead to

$$\langle\sigma v\rangle_{ij} = \frac{1 + \delta_{ij}}{1 + \delta_{om}} \frac{g_o G_m}{g_j G_i} \left(\frac{\mu_{om}}{\mu_{ij}}\right)^{3/2} \exp(-Q_{o,j}/kT) \langle\sigma v\rangle_{mo} . \tag{2.1.30}$$

This relation is immensely useful in nuclear networks, since many unknown reaction rates can be determined from the (known) inverse reaction. It also warrants a

proper balance of forward and reverse rates, which is not guaranteed when different predictions or even different sources are used.

2.1.7 Decays, photodisintegrations, lepton captures

So far, we have only looked at reactions of the type $i(j,o)m$, where both projectile j and target i are nuclei. Before we can perform full nucleosynthesis calculations, we have to derive terms for the reactivity in nuclear decays, reactions between nuclei and leptons, and photodissociations. In the classical picture, a nucleus can decay to a state in a neighbouring nucleus lower than its initial state and emit an electron, positron, or α-particle in the process (note: γ-decays are included as part of capture reactions which populate excited states in the compound nucleus, such as (n,γ) or (p,γ) reactions). The Q-value again is the difference between the energy levels of the initial and final states and is always positive for decays. The reactivity is inversely proportional to the half-life:

$$r_i = \frac{\ln 2}{\tau_{1/2}} n_i = \lambda_i n_i \,, \tag{2.1.31}$$

where i denotes the decaying nucleus. Under laboratory conditions, i.e., for decay from the ground state only, λ_i is constant. However, in a stellar plasma, excited states n with individual decay constants $\lambda_{i,n}$ can be thermally populated, leading to a temperature-dependent total decay "constant"

$$\lambda_i(T) = \frac{\sum_n \lambda_{i,n}(2J_n+1)\exp(-E_n/kT)}{\sum_n (2J_n+1)\exp(-E_n/kT)} \,. \tag{2.1.32}$$

For photodisintegrations, too, a temperature-dependent decay term can be introduced, similarly to equation (2.1.32):

$$\begin{aligned} r_{i,\gamma} &= \lambda_{i;\gamma,o}(T) n_i \text{ , with} \\ \lambda_{i;\gamma,o}(T) &= \frac{1}{\pi^2 c^2 \hbar^3} \int_0^\infty \frac{\sigma_i(\gamma,o;E_\gamma) E_\gamma^2}{\exp(E_\gamma/kT)-1} dE_\gamma \,. \end{aligned} \tag{2.1.33}$$

This expression can be found by taking into consideration that photons follow a Planck distribution and the relative velocity between target and projectile is the speed of light. The photodisintegration cross section $\sigma_i(\gamma,o)$ can be determined via detailed balance (see equation (2.1.28)) from the capture cross section of the reverse reaction $m(o,\gamma)i$. Finally, under special circumstances, nuclei will capture electrons, positrons, or neutrinos. As those leptons have a smaller mass than nuclei by several magnitudes, the nucleus can be considered at rest and the relative velocity becomes the velocity of the lepton. In the case of electron capture, the reaction is $e^- + (Z,A) \rightarrow (Z-1,A) + \nu$ and the reactivity can be expressed as

$$\begin{aligned} r_{i,e} &= n_i \int \sigma_e(v_e) v_e dn_e \\ &= \lambda_{i,e}(\rho Y_e, T) n_i \,. \end{aligned} \tag{2.1.34}$$

This time, the term $\lambda_{i,e}(\rho Y_e, T)$ is temperature- and density-dependent, since $n_e = \rho N_A Y_e$, where Y_e denotes the number of electrons per baryon or *electron fraction*. If the temperature is high enough for photons to produce electron-positron pairs via $\gamma + \gamma \rightarrow e^+ + e^-$, then the positrons are in thermal equilibrium with photons and electrons and a similar treatment can be utilized for positron capture (Fuller et al., 1980, 1982, 1985):

$$e^+ + (Z, A) \rightarrow (Z + 1, A) + \overline{\nu}\,. \tag{2.1.35}$$

At very high densities, e.g., close to the proto-neutron star in a supernova, the neutrino scattering cross section becomes large enough for neutrinos to become thermalized. In this case, also neutrino and antineutrino captures can occur, which are the reverse reactions of electron and positron captures, respectively. As such, the neutrino capture rate $\lambda_{\nu/\overline{\nu}}(\rho Y_e, T)$ can be determined via detailed balance.

2.2 Nuclear Networks and Their Numerical Implementation

As stated before, the reactivity r is the number of reactions per volume and time. It is therefore directly related to the change in number densities of the participating nuclear species:

$$r_{i;j} = -\left(\frac{\partial n_i}{\partial t}\right)_\rho = -\left(\frac{\partial n_j}{\partial t}\right)_\rho = +\left(\frac{\partial n_o}{\partial t}\right)_\rho = +\left(\frac{\partial n_m}{\partial t}\right)_\rho . \tag{2.2.1}$$

The above relation is valid for the reaction $i(j, o)m$, if the density stays constant, i.e., the only change in number densities n_k is due to the reaction. However, for most astrophysical applications it is impossible to assume constant density, especially for explosive events. Equation (2.2.1) then must be modified using $n_i = \rho N_A Y_i$, with Avogadro's constant $N_A = 6.022 \times 10^{23}$ mol^{-1}:

$$\begin{aligned} \dot{n}_i &= \left(\frac{\partial n_i}{\partial t}\right)_\rho + \left(\frac{\partial n_i}{\partial t}\right)_{Y_i} \\ &= \rho N_A \dot{Y}_i + n_i \frac{\dot{\rho}}{\rho}\,. \end{aligned} \tag{2.2.2}$$

It is much more practical to use the abundance Y_i, defined as

$$Y_i = \frac{n_i}{\rho N_A}\,, \quad \dot{Y}_i = \frac{\dot{n}_i}{\rho N_A} - \frac{n_i}{\rho N_A}\frac{\dot{\rho}}{\rho}\,. \tag{2.2.3}$$

The balance equations (2.2.2) then become

$$\begin{aligned}
\dot{Y}_i &= \frac{1}{\rho N_A}\left(\frac{\partial n_i}{\partial t}\right)_\rho = -\frac{r_{i;j}}{\rho N_A} = -\frac{1}{1+\delta_{ij}}\rho N_A \langle\sigma v\rangle_{i;j} Y_i Y_j \,, \\
\dot{Y}_j &= -\frac{1}{1+\delta_{ij}}\rho N_A \langle\sigma v\rangle_{i;j} Y_i Y_j \,, \\
\dot{Y}_o &= \dot{Y}_m = \frac{1}{1+\delta_{ij}}\rho N_A \langle\sigma v\rangle_{i;j} Y_i Y_j \,.
\end{aligned} \tag{2.2.4}$$

The same procedure can be applied to decays, photodisintegrations, and lepton captures which destroy nucleus i and produce nucleus m:

$$\begin{aligned}
\dot{Y}_i &= \frac{1}{\rho N_A}\left(\frac{\partial n_i}{\partial t}\right)_\rho = -\frac{r_i}{\rho N_A} \\
&= -\frac{\lambda_i n_i}{\rho N_A} = -\lambda_i Y_i \,, \\
\dot{Y}_m &= \lambda_i Y_i \,.
\end{aligned} \tag{2.2.5}$$

Equations (2.2.4) and (2.2.5) describe the change in abundance due to a two-particle reaction and a decay-type reaction, respectively. In a full nuclear network, the nuclear species i can be affected by many different reactions, which are all treated simultaneously. Therefore, $\dot{Y}_i$ is the sum of all decays, two-particle and three-particle reactions destroying or producing the species i:

$$\begin{aligned}
\dot{Y}_i = &\sum_j N_j^i \lambda_j Y_j + \sum_{j,k} \frac{N_{j,k}^i}{1+\delta_{jk}} \rho N_A \langle\sigma v\rangle_{j;k} Y_j Y_k \\
&+ \sum_{j,k,l} \frac{N_{j,k,l}^i}{1+\Delta_{jkl}} \rho^2 N_A^2 \langle\sigma v\rangle_{j;k;l} Y_j Y_k Y_l \,.
\end{aligned} \tag{2.2.6}$$

In order to account for reactions where more than one nucleus of the same species is involved, the coefficients N^i are introduced. Their sign also specifies if the reaction destroys or produces species i. The last term in equation (2.2.6) describes three-particle reactions. The factor Δ_{jkl} prevents multiple counting and is defined as

$$\Delta_{jkl} = \delta_{jk} + \delta_{kl} + \delta_{jl} + 2\delta_{jkl} \,. \tag{2.2.7}$$

In a nuclear network, equation (2.2.6) needs to be solved for each isotope at each timestep. Rewriting the set of differential equations in vector notation and replacing the time derivatives with finite steps (Euler's method) leads to

$$\vec{Y}_{n+1} = \vec{Y}_n + h\vec{f}(t_{n+1}, \vec{Y}_{n+1}) \,, \tag{2.2.8}$$

where n is the iteration index and h denotes the timestep. Nuclear rates usually span over many different orders of magnitude, making the system of differential

equations extremely stiff (Hix & Thielemann, 1999). Therefore, it is advantageous to use the implicit method, i.e., evaluate the function f at t_{n+1} instead of t_n. The solution to this equation can now be found by moving all terms on the left-hand side and finding the zeroes of the resulting term via the Newton-Raphson method, which eventually requires the inverse of the Jacobian matrix

$$\mathbf{J} = \frac{1}{\Delta t} - \frac{\partial \dot{\vec{Y}}(t + \Delta t)}{\partial \vec{Y}(t + \Delta t)} \,. \tag{2.2.9}$$

This is computationally the most time-consuming process while solving a nuclear reaction network. However, a few considerations can help simplify the Jacobian matrix substantially. In particular, any given nucleus will not react with all other species, but will instead have only a few possible reaction channels, such as neutron captures, proton captures, alpha captures, or photodisintegrations. Consequently, the vast majority of matrix entries are zeroes, and the matrix is called *sparse* (see figure 2.1). In our network (Winteler, 2011), we use the PARDISO matrix solver (Schenk & Gärtner, 2004), which in addition also makes use of the so-called *compressed sparse column format* in order to store only the non-zero entries of the Jacobian matrix.

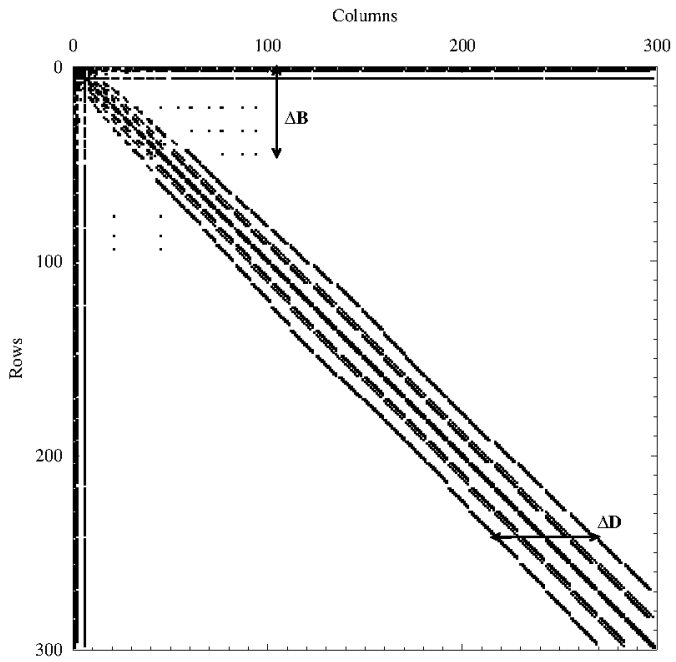

Figure 2.1: Example of a sparse Jacobian matrix for a network with 300 nuclear species. The black dots mark the non-zero entries. Figure from Hix & Thielemann (1999).

2.3 Nuclear Statistical Equilibrium

At large temperatures, the photons carry high energies and photodissociations become so efficient that they establish an equilibrium with their respective inverse capture reaction. If this condition is met throughout the nuclear chart, the whole composition is in a state of *nuclear statistical equilibrium* (NSE). In such a global equilibrium, the added chemical potentials of target and projectile are equal to those of the reaction products, i.e.,

$$\bar{\mu}(Z,N) = \bar{\mu}_n + \bar{\mu}(Z,N-1) = \bar{\mu}_p + \bar{\mu}(Z-1,N)\,. \tag{2.3.1}$$

Similarly, assembling a nucleus (Z,N) can be considered in equilibrium to complete photodissociation into protons and neutrons. Therefore, its chemical potential is equal to the added potentials of Z protons and N neutrons:

$$\bar{\mu}(Z,N) = Z\bar{\mu}_p + N\bar{\mu}_n\,. \tag{2.3.2}$$

Since nuclei and nucleons obey Maxwell-Boltzmann statistics, the chemical potentials are given by

$$\bar{\mu}_i = kT \ln\left[\frac{\rho N_A Y_i}{G_i}\left(\frac{2\pi\hbar^2}{m_i kT}\right)^{3/2}\right] + m_i c^2\,, \tag{2.3.3}$$

which together with Eq. (2.3.2), and solved for the abundance $Y(Z,N)$ gives

$$Y(Z,N) = G_{Z,N}(\rho N_A)^{A-1}\frac{A^{3/2}}{2^A}\left(\frac{2\pi\hbar^2}{m_u kT}\right)^{\frac{3}{2}(A-1)} \exp\left(\frac{B_{Z,N}}{kT}\right) Y_n^N Y_p^Z\,. \tag{2.3.4}$$

For simplification, the proton and neutron masses are set to m_u in Eq. (2.3.4). The factor $G_{Z,N}$ denotes the partition function and $B_{Z,N}$ is the binding energy of nucleus (Z,N). Additional relations for the determination of Y_n and Y_p can be introduced, namely the conservation of mass and the charge neutrality (i.e., the assumption that the proton density n_p is equal to the electron density n_e):

$$\begin{aligned} \sum_i A_i Y_i &= 1 \\ \sum_i Z_i Y_i &= Y_e\,. \end{aligned} \tag{2.3.5}$$

The second relation also serves as the definition of the electron fraction Y_e. Using Equations (2.3.4) & (2.3.5), the individual NSE abundances can therefore be directly calculated in dependence of temperature, density, and electron fraction (provided that the partition functions and binding energies are known), and it is not required to solve the full reaction network. Furthermore, some trends can be seen in Eq. (2.3.4): in high temperature conditions, the term $(kT)^{-\frac{3}{2}(A-1)}$ dominates, and nuclei with small mass numbers are preferred. High densities, on the

other hand, favour nuclei with large mass number because of the ρ^{A-1} term. Whenever these two terms are equally strong, the term $\exp(B_{Z,N}k^{-1}T^{-1})$ guarantees that tightly bound nuclei are most abundant. Those are found around $Z = 26$ (generally referred to as *iron group nuclei*).

2.4 Nuclear Mass Models

Nuclear masses are an important ingredient for nuclear networks, as the Q-value can be determined solely by comparing the summed-up binding energies of the products with those of the initial reactants. For neutron captures, for example, the neutron separation energy S_n corresponds to the difference in binding energies between the isotopes (Z, N) and $(Z, N + 1)$. The binding energy B is directly linked to the nuclear mass $m_{Z,N}$ in the following way:

$$B(Z, N) = (Zm_p + Nm_n - m_{Z,N})c^2 \,. \tag{2.4.1}$$

Wherever possible, experimentally determined values are taken for the nuclear masses. However, most of the neutron-rich isotopes that lie on the r-process path cannot (yet) be produced under laboratory conditions, and no experimental data are available for them. For these nuclei, theoretically predicted masses have to be used. Nuclear mass models usually comprise several free parameters which are fitted on existing (experimental) mass data. From there, an extrapolation is made for the nuclei with unknown masses. Moreover, mass models make predictions for the internal nuclear structure of nuclei which cannot be studied experimentally. Approaches for the development of mass models include:

- parametrized models with empirical shell terms whose parameters are fitted to experimentally known masses
- macroscopic-microscopic theories including corrections for shell closures and pairing
- fully self-consistent microscopic theories derived from nucleon-nucleon interaction.

2.4.1 The Bethe–Weizsäcker Mass Formula

The Bethe–Weizsäcker mass formula (Bethe & Bacher, 1936) provides a method to derive the binding energy (and with it, the effective mass) of all nuclei by means of some basic physical considerations. First, consider the bound nucleons sitting

in a potential well with depth v_0. If the nucleus is in its ground state, the energy of the least bound nucleon corresponds to the Fermi energy E_F. It can be shown that the average energy of the bound nucleons in a nucleus is $\bar{E} = 3/5 E_F$. Thus, each nucleon has an average binding energy of $v_0 - \bar{E}$, and in order to unbind an ensemble of N nucleons, a total energy of $E = N(v_0 - \bar{E})$ is required. This means that for a nucleus with $A = N + Z$ nucleons, the first and most important term for the total binding energy can be written as

$$B_V = (v_0 - \bar{E})A = a_V A \,. \tag{2.4.2}$$

Note that a_V is an approximate constant for all nuclei. The next term is a correction for the nucleons close to the surface of the nucleus. They are not surrounded by other nucleons and are therefore less bound. The surface term reduces the total binding energy accordingly:

$$B_S = -a_s A^{2/3} \,. \tag{2.4.3}$$

Since the mass number A is proportional to the volume of the nucleus ($A \propto V$), the surface term is proportional to the surface of the nucleus. So far, Coulomb repulsion between the protons has been neglected. Obviously, this effect decreases the effective binding strength. We can treat the nucleus as a uniformly charged sphere with electrostatic energy $E_{Coul} = 3/5\ Q^2/R$, where $Q = Ze$ and $R \propto A^{1/3}$. This gives

$$B_C = 3/5\ Z^2 A^{-1/3} \tag{2.4.4}$$

for the Coulomb term. In fact, since every proton only experiences the repulsion of the other $Z-1$ protons, Z^2 should be replaced by $Z(Z-1)$. However, for the purpose of obtaining an approximative mass formula, usually the simpler expression Z^2 is used. The next term describes the quantum-mechanical notion that a nucleus with $N = Z$ is energetically more bound than an asymmetric one. In Equation (2.4.2) we assumed that all nucleons have an average energy of $\bar{E} = 3/5\ E_F$. For $N \neq Z$, however, the Fermi energy is not the same for neutrons and protons. Instead, we should rewrite Equation (2.4.2):

$$\begin{aligned} B_V^{corr} &= N(v_0 - \bar{E}_N) + Z(v_0 - \bar{E}_Z) \\ &= N(v_0 - \bar{E}) + N(\bar{E} - \bar{E}_N) + Z(v_0 - \bar{E}) + Z(\bar{E} - \bar{E}_Z) \\ &= a_V A + A\bar{E} - N\bar{E}_N - Z\bar{E}_Z \\ &= a_V A + B_{sym} \,. \end{aligned} \tag{2.4.5}$$

Plugging in the expressions for $\bar{E}_N = 3/5\ E_{F,N}$ and $\bar{E}_Z = 3/5\ E_{F,Z}$ and expanding in a Taylor series at $A/2$ one gets

$$\begin{aligned} B_{sym} &= -a_{sym}\frac{(N-Z)^2}{A} \,, \text{with} \\ a_{sym} &= \frac{5h^2}{9m_u}\left(\frac{3}{16\pi}\right)^{2/3} \,. \end{aligned} \tag{2.4.6}$$

Finally, as both neutrons and protons are fermions with spin $1/2$, they can form pairs with a total spin of 0 or 1, with the former case increasing the total binding energy. Therefore, nuclei with an even number of protons and an even number of neutrons have all their nucleons stored in pairs and, as a consequence, are stronger bound. In contrast, a nucleus with an odd-odd configuration has a decreased stability, since one proton as well as one neutron do not find a pairing partner. The pairing term B_{pair} contributes around $12/\sqrt{A}$ MeV. Thus,

$$B_{pair} = \begin{cases} +\frac{12}{\sqrt{A}} & \text{if N even \& Z even} \\ 0 & \text{if A odd} \\ -\frac{12}{\sqrt{A}} & \text{if N odd \& Z odd}\,. \end{cases} \tag{2.4.7}$$

The sum of all these terms generally gives a good estimate for the binding energy of all nuclei:

$$B(A,Z) = a_V A - a_S A^{2/3} - a_C Z^2 A^{-1/3} - a_{sym}\frac{(N-Z)^2}{A} + B_{pair}\,. \tag{2.4.8}$$

The coefficients are determined by comparing to experimentally known binding energies. A common choice for the coefficients is

$$a_V = 16\text{ MeV},\quad a_S = 18.5\text{ MeV},\quad a_C = 0.72\text{ MeV},\quad a_{sym} = 23.4\text{ MeV}\,. \tag{2.4.9}$$

Equation (2.4.8) demonstrates several fundamental characteristics of nuclei throughout the nuclear chart. First of all, the symmetry term establishes that $N = Z$ nuclei are energetically favoured. However, as Z increases, there is a deviation from the $N = Z$ rule as the Coulomb term becomes more important (since Z increases proportional to A, therefore $B_C \propto A^{5/3}$, while the leading term $B_V \propto A$). This means that stable nuclei with higher masses generally have more neutrons than protons. Furthermore, from the pairing term we can see that nuclei with even proton and neutron numbers are stronger bound than those with odd Z and N. In fact, above $Z = 7$ most odd-odd nuclei are β-unstable, decaying into an even-even nucleus.

2.4.2 The Finite–Range Droplet Model

The Bethe–Weizsäcker model introduced in the last section is useful to discuss the basic terms that have an influence on the binding energy (and thus the mass) of a nucleus. In reality, however, many more structural effects need to be taken into account in order to obtain an accurate mass model. For instance, shell effects have a large influence on the nuclear potential energy. Moreover, the shape of the nucleus is also important, and for many nuclei the ground-state configuration is not spherical. Mass models that are used in nowadays nucleosynthesis calculations are therefore much more complex than the formalism discussed in the last section.

The Finite-Range Droplet Model (FRDM) is a macroscopic-microscopic approach. Here the macroscopic potential energy term is based on an improvement of the droplet model (Myers & Swiatecki, 1969, 1974), while the microscopic corrections are calculated using Strutinsky's method (Strutinsky, 1967, 1968) in a realistic, diffuse-surface, folded Yukawa single-particle potential. The total nuclear potential energy can be written as the sum of the macroscopic and the microscopic energy terms:

$$E_{pot}(Z, N, shape) = E_{mac}(Z, N, shape) + E_{mic}(Z, N, shape)\,. \tag{2.4.10}$$

For a given deformation ε_a, it is convenient to define the microscopic term as follows:

$$E_{mic}(Z, N, \varepsilon_a) = E_{s+p}(Z, N, \varepsilon_a) + E_{mac}(Z, N, \varepsilon_a) - E_{mac}(Z, N, \varepsilon_{sphere})\,, \tag{2.4.11}$$

where E_{s+p} is the term accounting for the shell and pairing corrections. This allows equation (2.4.10) to be rewritten as

$$E_{pot}(Z, N, \varepsilon_a) = E_{mac}(Z, N, \varepsilon_{sphere}) + E_{mic}(Z, N, \varepsilon_a)\,. \tag{2.4.12}$$

The terms introduced in the Bethe–Weizsäcker mass formula (in section 2.4.1) reappear in the macroscopic term of the FRDM in slightly different form, but with the same dependencies from A. In its current form (Möller et al., 2016) it reads

$$
\begin{aligned}
&E_{mac}(Z,N,shape) = \\
&ZM_p + NM_n && \text{summed-up mass excess of protons and neutrons} \\
&+\left(-a_1 + J\overline{\delta}^2 - \frac{1}{2}K\overline{\varepsilon}\right)A && \text{volume energy} \\
&+\left(a_2 B_1 + \frac{9}{4}\frac{J^2}{Q}\overline{\delta}^2\frac{B_s^2}{B_1}\right)A^{2/3} && \text{surface energy} \\
&+ a_3 A^{1/3} B_k && \text{curvature energy} \\
&+ a_0 A^0 && A^0 \text{ energy} \\
&+ c_1 \frac{Z^2}{A^{1/3}} B_3 && \text{Coulomb energy} \\
&- c_2 Z^2 A^{1/3} B_r && \text{volume redistribution energy} \\
&- c_4 \frac{Z^{4/3}}{A^{1/3}} && \text{Coulomb exchange correction} \\
&- c_5 Z^2 \frac{B_w B_s}{B_1} && \text{surface redistribution energy} \\
&+ f_0 \frac{Z^2}{A} && \text{proton form-factor correction to the Coulomb energy} \\
&- c_a (N-Z) && \text{charge-asymmetry energy} \\
&+ W\left(|I| + \begin{cases} 1/A & , Z \text{ and } N \text{ odd and equal} \\ 0 & , \text{otherwise} \end{cases}\right) && \text{Wigner energy} \\
&+ \begin{cases} +\overline{\Delta}_p + \overline{\Delta}_n - \delta_{np} & , Z \text{ and } N \text{ odd} \\ +\overline{\Delta}_p & , Z \text{ odd and } N \text{ even} \\ +\overline{\Delta}_n & , Z \text{ even and } N \text{ odd} \\ +0 & , Z \text{ and } N \text{ even} \end{cases} && \text{average pairing energy} \\
&- a_{el} Z^{2.39} && \text{energy of bound electrons}
\end{aligned}
\tag{2.4.13}
$$

Here M_p and M_n are the proton and neutron mass excess, $a_1, a_2, a_3, a_0, a_{el}, K, J, Q$, and c_a are all coefficients and constants that are determined from experimental data, while c_1, c_2, c_4, and c_5 are physically motivated constants:

$$\begin{aligned} c_1 &= \frac{3}{5}\frac{e^2}{r_0}\,, \\ c_2 &= \frac{1}{336}\left(\frac{1}{J}+\frac{18}{K}\right)c_1^2\,, \\ c_4 &= \frac{5}{4}\left(\frac{3}{2\pi}\right)^{2/3} c_1\,, \\ c_5 &= \frac{1}{64Q}c_1^2\,. \end{aligned} \tag{2.4.14}$$

Furthermore, W is the Wigner constant (with a value of 30 MeV) and $I = (N-Z)/A$ is the relative neutron excess. The form factor coefficient f_0 is defined as

$$f_0 = -\frac{1}{8}\left(\frac{145}{48}\right)\frac{r_p^2 e^2}{r_0^3}\,, \tag{2.4.15}$$

where $r_p = 0.80$ fm is the proton root-mean-square radius and $r_0 = 1.16$ fm is the nuclear-radius constant. The average bulk nuclear asymmetry $\overline{\delta}$ is given by

$$\overline{\delta} = \left(I + \frac{3}{16}\frac{c_1}{Q}\frac{Z}{A^{2/3}}\frac{B_v B_s}{B_1}\right)\left(1+\frac{9}{4}\frac{J}{Q}\frac{1}{A^{1/3}}\frac{B_s^2}{B_1}\right)^{-1} \tag{2.4.16}$$

and the average relative deviation in the bulk of the density $\overline{\varepsilon}$ by

$$\overline{\varepsilon} = \left(Ce^{-\gamma A^{1/3}} - 2a_2\frac{B_2}{A^{1/3}} + L\overline{\delta}^2 + c_1\frac{Z^2}{A^{4/3}}B_4\right)K^{-1}\,. \tag{2.4.17}$$

The density-symmetry constant L, the constant C, and the range constant γ in the exponential term are again adjusted to experimental data. The quantities B_1 and B_3 are the relative generalized surface energy and the relative Coulomb energy, respectively:

$$\begin{aligned} B_1 &= \frac{A^{-2/3}}{8\pi^2 r_0^2 a^4}\int\int_V \left(2-\frac{|\mathbf{r}-\mathbf{r}'|}{a}\right)\frac{e^{-|\mathbf{r}-\mathbf{r}'|/a}}{|\mathbf{r}-\mathbf{r}'|/a}d^3r d^3r'\,, \\ B_3 &= \frac{15}{32\pi^2}\frac{A^{-5/3}}{r_0^5}\int\int_V \frac{d^3r d^3r'}{|\mathbf{r}-\mathbf{r}'|}\left[1-\left(1+\frac{1}{2}\frac{|\mathbf{r}-\mathbf{r}'|}{a_{den}}\right)e^{-|\mathbf{r}-\mathbf{r}'|/a_{den}}\right]\,, \end{aligned} \tag{2.4.18}$$

where a is a range constant for the Yukawa potential and the diffuseness constant a_{den} is a constant with a slightly different value than a used for the diffuse-surface nucleus. Both B_1 and B_3 are calculated for a spherical volume with nuclear radius $R_0 = r_0 A^{1/3}$. In order to describe the response of the nucleus to a change in size

(e.g., compression), the derivatives of B_1 and B_3 have already been introduced above as B_2 and B_4. They are defined as

$$\begin{aligned} B_2 &= \frac{1}{2x_0}\left[\frac{d}{dx}(x^2 B_1)\right]_{x=x_0} ; x = R/a \text{ and } x_0 = r_0 A^{1/3} a^{-1} , \\ B_4 &= -y_0^2\left[\frac{d}{dy}\left(\frac{B_3}{y}\right)\right]_{y=y_0} ; y = R/a_{den} \text{ and } y_0 = r_0 A^{1/3} a_{den}^{-1} . \end{aligned} \tag{2.4.19}$$

Further energy terms used in Eq. (2.4.13) are

$$\begin{aligned} B_s &= \frac{A^{-2/3}}{4\pi r_0^2}\int_S dS && \text{surface energy,} \\ B_v &= -\frac{15A^{-4/3}}{16\pi^2 r_0^4}\int_S \tilde{W}(\mathbf{r}) dS && \text{neutron skin energy,} \\ B_w &= \frac{225A^{-2}}{64\pi^3 r_0^6}\int_S \left[\tilde{W}(\mathbf{r})\right]^2 dS && \text{surface redistribution energy,} \\ B_k &= \frac{A^{-1/3}}{8\pi r_0}\int_S \left(\frac{1}{R_1}+\frac{1}{R_2}\right) dS && \text{curvature energy,} \\ B_r &= \frac{1575A^{-7/3}}{64\pi^3 r_0^7}\int_V \left[\tilde{W}(\mathbf{r})\right]^2 d^3 r && \text{volume redistribution energy,} \end{aligned} \tag{2.4.20}$$

where

$$\begin{aligned} W(\mathbf{r}) &= \int_V \frac{1}{|\mathbf{r}-\mathbf{r}'|} d^3 r' , \\ \tilde{W}(\mathbf{r}) &= W(\mathbf{r}) - \overline{W} , \end{aligned} \tag{2.4.21}$$

with

$$\overline{W} = \frac{3A^{-1}}{4\pi r_0^3}\int_V W(\mathbf{r}) d^3 r . \tag{2.4.22}$$

The pairing energy terms in equation (2.4.13) are given by

$$\begin{aligned} \overline{\Delta}_n &= \frac{r_{mac} B_s}{N^{1/3}} , \\ \overline{\Delta}_p &= \frac{r_{mac} B_s}{Z^{1/3}} , \\ \delta_{np} &= \frac{h}{B_s A^{2/3}} , \end{aligned} \tag{2.4.23}$$

where $r_{mac} = 4.80$ MeV is the average pairing-gap constant and $h = 6.6$ MeV is the neutron-proton interaction constant.

The microscopic correction term $E_{s+p}(Z, N, shape)$ from equation (2.4.11) can be split up into individual shell terms and pairing terms for neutrons and protons,

respectively:

$$\begin{aligned} E_{s+p}(Z,N,shape) =& E^{n}_{shell}(N,shape) + E^{p}_{shell}(Z,shape) \\ &+ E^{n}_{pair}(N,shape) + E^{p}_{pair}(Z,shape)\,. \end{aligned} \tag{2.4.24}$$

For the shell correction terms Strutinsky's method is used (Strutinsky, 1967, 1968):

$$E^{n}_{shell}(N,shape) = \sum_{i=1}^{N} e_i - \tilde{E}^{n}(N,shape)\,, \tag{2.4.25}$$

where e_i are the calculated single-particle energies for all neutrons and $\tilde{E}(N, shape)$ is the smooth single-particle energy sum obtained by means of Strutinsky's method. The shell correction term for the protons is calculated analogously. The pairing correction term has a similar form, as it is the difference between the pairing correlation energy and the average pairing correlation energy, the detailed formula of which can be found in Möller et al. (2016).

The FRDM is not well-suited to describe large deformations, and therefore cannot give reliable predictions on fission data (e.g., fission barriers, scission points, etc.). In order to obtain these data (consistent with the FRDM), it is necessary to make use of the related *finite-range liquid-drop model* (FRLDM) which has a larger average error through the nuclear chart, but is designed to treat deformed nuclei due to a different parametrization within the folded Yukawa potential.

The FRDM(2012) has a substantially lower theoretical error compared to previous versions, as it has seen a decrease in error from $\sigma = 0.6140$ MeV in 1992 to $\sigma = 0.5595$ MeV (Möller et al., 2016) when both are compared to the atomic mass data set AME2003 (Audi et al., 2003). If not specified, our results are obtained using reaction rates based on the FRDM (1992) model.

Figure 2.2 shows a comparison of the FRDM(2012) (top) and FRDM(1992) (bottom) mass predictions compared to the AME2012 atomic mass evaluation. It is evident that the error has decreased for the newer model, especially for the heavier nuclei above the $N = 50$ neutron shell closure.

2.4.3 The Extended Thomas Fermi Model with Strutinsky Integral

The Extended Thomas Fermi Model with Strutinsky Integral (ETFSI) model is an approximation of the Hartree-Fock-Bogoliubov (HFB) model. Like HFB, it assumes a Skyrme-like nucleon-nucleon interaction. The shell corrections are derived from single-particle levels corresponding to a Skyrme force by use of a Strutinsky integral method, and the pairing correction is calculated for a δ-function pairing interaction by use of the Bardeen-Cooper-Schrieffer (BCS)-approximation

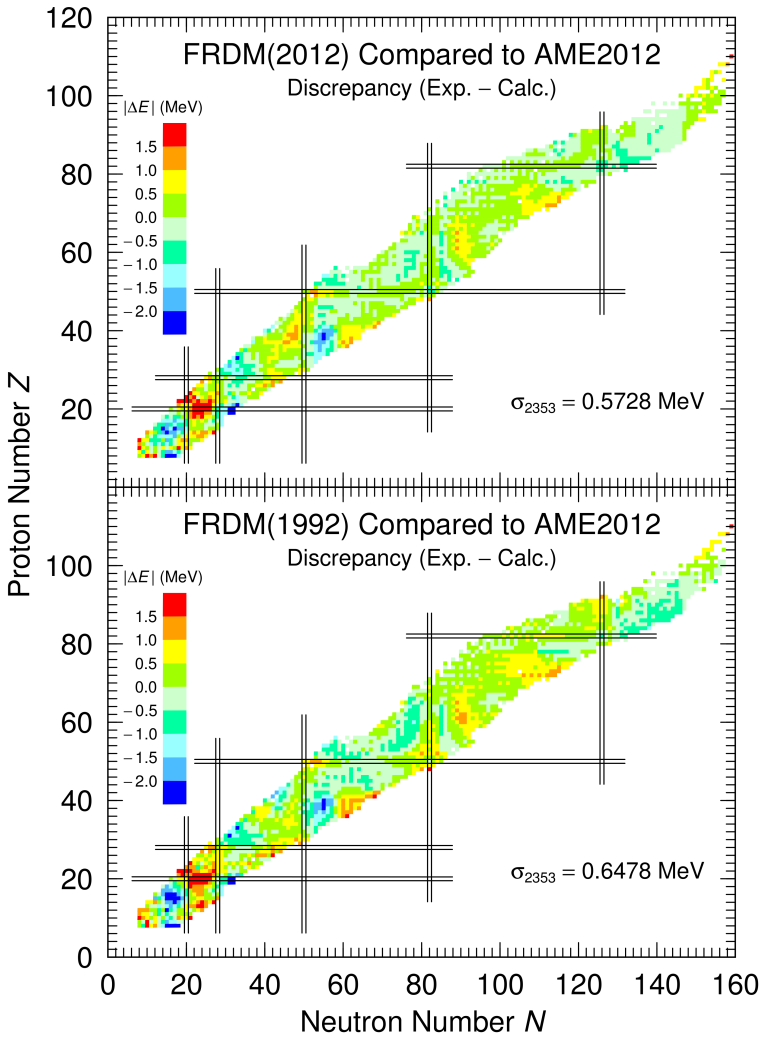

Figure 2.2: Theoretical mass predictions from the FRDM(2012) (top) and the previous FRDM(1992) version (bottom) compared to the experimental mass database AME2012. Note that the parameters of the FRDM(2012) have been adjusted to the AME2003 evaluation, and for the FRDM(1992) an even earlier version (i.e., AME1989) was used. Figure from Möller et al. (2016).

(Bardeen et al. 1957; in contrast to the Bogoliubov approximation which is used in the HFB model). For the initial model, the reported error was 0.736 MeV (Aboussir et al., 1995). The ETFSI model was established specifically to predict masses of r-process nuclei and although it is an approximation to the HFB model, it is not significantly less accurate, but much more efficient. The Skyrme force describes the interaction between two nucleons and has the form

$$\begin{aligned} v_{ij} &= t_0(1 + x_0P_\sigma)\delta(\vec{r_i} - \vec{r_j}) \\ &+ t_1(1 + x_1P_\sigma)\frac{1}{2\hbar^2}\{p_{ij}^2\delta(\vec{r_i} - \vec{r_j}) + h.c.\} \\ &+ t_2(1 + x_2P_\sigma)\frac{1}{\hbar^2}\vec{p}_{ij} \cdot \delta(\vec{r_i} - \vec{r_j})\vec{p}_{ij} \\ &+ \frac{1}{6}t_3(1 + x_3P_\sigma)\{\rho_{q_i}(\vec{r_i}) + \rho_{q_j}(\vec{r_j})\}^\gamma\delta(\vec{r_i} - \vec{r_j}) \\ &+ \frac{i}{\hbar^2}W_0(\sigma_i + \sigma_j) \cdot \vec{p}_{ij} \times \delta(\vec{r_i} - \vec{r_j})\vec{p}_{ij}. \end{aligned} \tag{2.4.26}$$

Here $\vec{p}_{ij} = -(i\hbar/2)(\nabla_i - \nabla_j)$ is the relative momentum, $P_\sigma = 1/2(1 + \sigma_1 \cdot \sigma_2)$ is the two-body spin-exchange operator, q is the index for n or p, depending on whether the term in question relates to neutrons or protons, and $\rho_q(\vec{r})$ is the density of the corresponding species at $\vec{r}$. The quantities t_i, x_i, γ and W_0 are parameters that are fitted to existing mass data, although a physically motivated relation between (t_1, x_1) and (t_2, x_2) can be found.
The pairing force is described by the following equation:

$$v_{pair}(\vec{r}_{ij}) = V_\pi\delta(\vec{r}_{ij}), \tag{2.4.27}$$

The single pairing-strength parameter V_π is also fitted to mass data, thus leading to nine independent parameters in the whole model. The initial ETFSI model has also been updated, with the newer version called ETFSI–2.

2.4.4 Quenching Effect at Shell Closures: the ETFSI–Q Model

It has been found in HFB calculations that the shell effects associated to magic neutron numbers are quenched, as the drip line is approached. This can of course have large consequences for r-process calculations, as the r-process path runs close to the neutron drip line. In order to account for this effect, the ETFSI model has been modified and the result has been labelled ETFSI–Q (Pearson et al., 1996). Here, instead of

$$E_{tot} = E_{ETF} + E_{mic}\,, \tag{2.4.28}$$

the total energy is calculated by

$$E_{tot} = E_{ETF} + \frac{1}{q(N,Z)}E_{mic}\,, \tag{2.4.29}$$

where

$$q(N,Z) = 1 + \exp\left[\left(\frac{a}{Z} + b\right)N + \frac{c}{Z} + d\right] \tag{2.4.30}$$

is a quenching factor with fitting parameters a, b, c and d. The introduction of a quenching factor effectively reduces the deformation energy of highly neutron-rich nuclei, smoothing out troughs in the abundance distribution that arise from highly deformed neutron-rich nuclei in the ETFSI mass model.

2.4.5 The Hartree-Fock-Bogoliubov Model

The ETFSI model discussed in the previous section is based on the Hartree-Fock-Bogoliubov (HFB) model (see Goriely 2015b and references therein), which also relies on the skyrme force presented in equation (2.4.26). The exact HF energy E_{HF} depends on both the kinetic-energy density τ_q and the spin-current density $\vec{J}_q$, both of them in turn depending on the diagonal ($\rho_q(\vec{r})$) and the off-diagonal ($\rho_q(\vec{r},\vec{r}')$) entries of the density matrix ρ_{HF}. While the ETF method approximates τ_q and $\vec{J}_q$ by expressions $\tilde{\tau}_q$ and $\tilde{\vec{J}}_q$ that only depend on the diagonal parts of the density matrix, the off-diagonal terms are included in the HFB approach, rendering this method more precise, but also computationally much more expensive. Although it is labelled a fully microscopic model, it also makes use of some phenomenological terms that are fitted to existing experimental data in order to decrease the average error. The HFB model is updated and improved regularly. The newest updates are called HFB–28 and HFB–29 (Goriely, 2015b), but in this work we will make use of the openly available version HFB–14 (Goriely et al., 2007). A comparison of

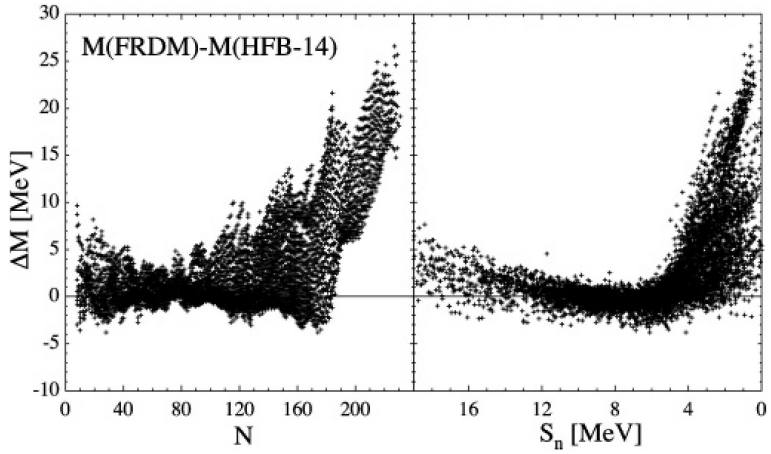

Figure 2.3: Differences in mass predictions between the FRDM and the HFB–14 model in dependence of neutron number (left) and neutron separation energy (right). The discrepancies grow as the neutron-drip line is approached. Figure from Goriely et al. (2007).

mass predictions between the FRDM and HFB−14 models is shown in Figure 2.3, revealing huge differences for nuclei far from stability and underlining the large uncertainties that are still present in r-process calculations.

Chapter 3

Galactic Chemical Evolution (GCE): A Short Overview

Whenever baryonic matter is ejected in an explosive astrophysical event, the (local) interstellar medium (ISM) becomes enriched with chemical elements that have been synthesized either during stellar evolution or in the explosion itself. Newforming stars in that region will then inherit the composition of the ISM at the time of their birth and therefore carry in their atmospheres a signature of the local nucleosynthesis history. By observing and analysing their stellar spectrum, we can obtain evidence of past events in the vicinity of the star and an estimate of its age. Stars of the first generation started with a composition originating from primordial nucleosynthesis, i.e., hydrogen, helium, as well as small amounts of lithium and beryllium. Elements with higher mass numbers are products of stellar evolution or explosive events (Burbidge et al., 1957; Cameron, 1957), and are mixed into the ISM after a star's death. The relative abundance of these heavier elements in a star is therefore an indication of the number of explosive events that happened prior to the star's birth in its vicinity. Historically, the added mass fraction of all elements with $Z > 2$ is called *metallicity*. Since iron is produced abundantly in many events and is easily detectable in most stars, often the star's iron-to-hydrogen ratio is used as a measure for its metallicity. We will introduce here a notation that is commonly used:

$$[\mathrm{A/B}] = \log_{10}\left(\frac{Y_A}{Y_B}\right)_{star} - \log_{10}\left(\frac{Y_A}{Y_B}\right)_{\odot}, \tag{3.0.1}$$

where A and B are any two elements (or isotopes) whose abundances are known both for the observed star and the sun. Stars with [Fe/H] = 0 are considered to have solar metallicity, and older (earlier-born) stars generally have a negative [Fe/H] value. Note, however, that [Fe/H] is not a perfect measure of a star's age, as it is also dependent on the frequency of explosive events in the star's galactic neighbourhood.

3.1 Linking the Different Astrophysical Nucleosynthesis Sites to Observations

Iron is produced in large amounts in supernovae (SNe) type Ia and core-collapse supernovae (CCSNe), which makes it a suitable representative of metallicity. Similarly, europium (Eu) is often used in order to identify the level of r-process material concentration in a star's atmosphere, as it is almost exclusively produced in the r-process. Plotting [Eu/Fe] against [Fe/H] therefore reveals the history of r-process material enrichment in the galaxy, leading to valuable insights concerning the frequency and appearance timescale of r-process sites.

Figure 3.1 shows observed [Mg/Fe] and [Eu/Fe] values in dependence of metallicity for stars from several large-sample surveys. Magnesium is chosen as a representative of α-elements because its abundance is known for many metal-poor stars. It is evident that [Mg/Fe] has only a small star-to-star scatter even at low metallicities, indicating that magnesium and other α-elements are often ejected in the same events as iron, namely CCSNe. The dip close to [Fe/H] = 0 is attributed to the emergence of SNe Ia, which appear late in the galactic history and eject a large amount of iron. While the low scatter in the Mg data advocates for a simultaneous production of Mg and Fe, this is clearly not the case for Eu, as the lower part of Figure 3.1 shows. At low metallicities ([Fe/H] ≈ -3) there is a large scatter with only a few stars rich in r-process material, which argues for a rare r-process site. Only with increasing metallicity the range of [Eu/Fe] values (indicated by the black dashed lines) becomes narrower. Again, the dip towards [Eu/Fe] = 0 as the metallicity increases is related to SNe Ia. Models of GCE attempt to reproduce the observed abundance ratios over the history of the galaxy, testing many parameters such as star formation rates, individual frequencies of different explosive events, etc. Most models, however, use a simplified approach assuming instantaneous mixing of the ISM in the whole galaxy (see, e.g., Chiappini et al. 2001; Spitoni et al. 2009; Matteucci et al. 2014). As a consequence, stars born at the same time, but in different locations in the galaxy are always treated as if they inherit the exact same composition of the ISM and these models can only be used to study trends (such as the red line in Figure 3.1b). Argast et al. (2004) introduced a model using an inhomogeneous mixing treatment of the ISM. Further developed by Wehmeyer et al. (2015), this model is also able to successfully reproduce the star-to-star scatter at low metallicities (see Figure 3.2). By varying the frequency and the Eu yield of r-process events in these models, a lot can be learned about the nature of the r-process site(s). Neutron star mergers, in particular, are expected to appear relatively late in the galactic history, as they require both stars in a binary system to explode as a supernova (polluting the surrounding ISM with their SN ejecta in the process) and the remaining neutron stars to spiral inwards, losing energy by means of gravitational wave emission, until they finally collide. Therefore, it is difficult to explain the high europium yields in some metal-poor stars with nucle-

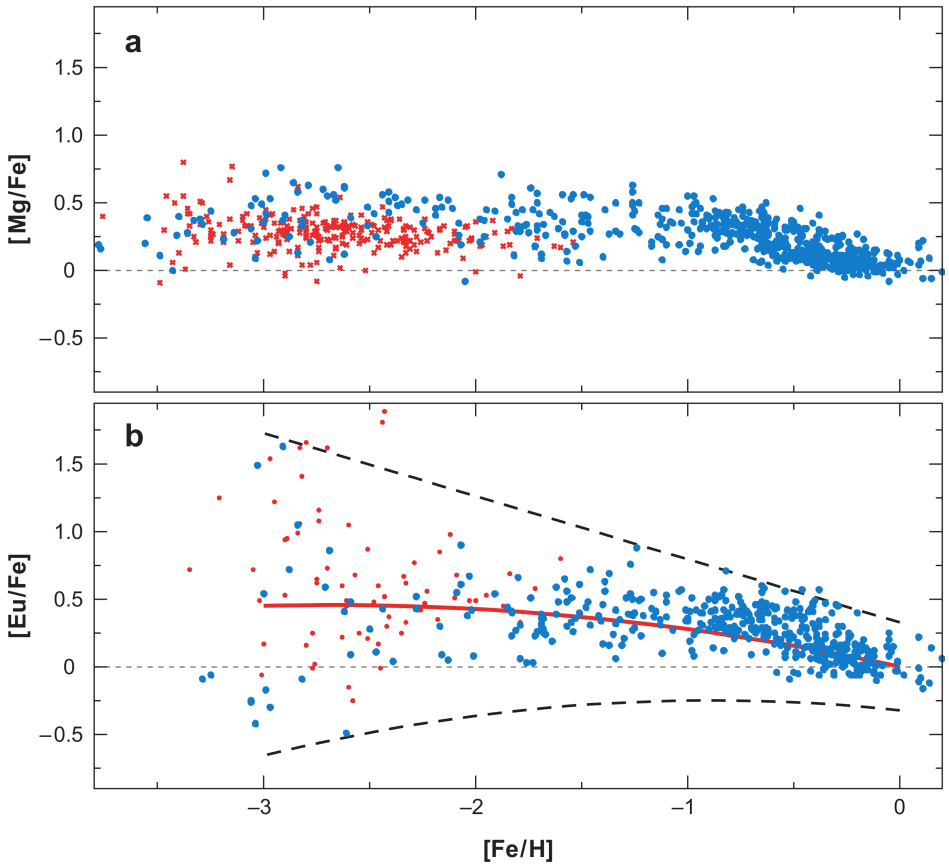

Figure 3.1: Values for (a) [Mg/Fe] and (b) [Eu/Fe] in dependence of [Fe/H] for stars observed in large-sample surveys. The different colours indicate different sources (see caption for Figure 14 in Sneden et al. 2008). The red line in (b) is the least-square fit to the [Eu/Fe] data and the black dashed lines represent the approximate maximum and minimum values for the stars.

osynthesis in NSMs. A possible solution to this problem is an additional r-process site which contributes primarily in the young galaxy. *Magneto-hydrodynamically driven* (MHD) SNe seem to fulfil these requirements: Simulations have shown that the successful ejection of material in the typical polar jets needs a high rotational velocity and large magnetic fields in the progenitor, conditions which are more easily realized in stars with low metallicity (Woosley & Heger, 2006). MHD SNe and their credentials as r-process site candidates are discussed further in section 7.3.

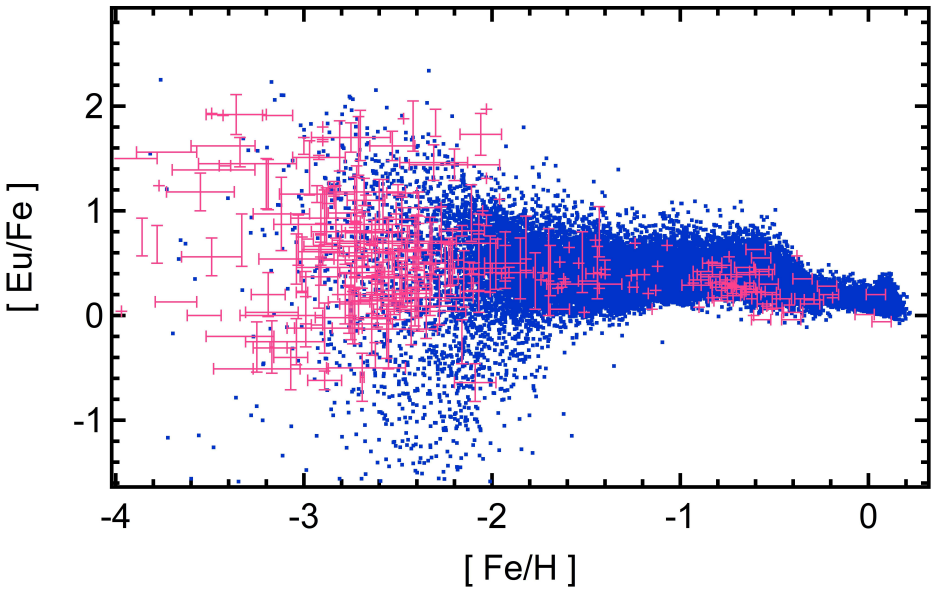

Figure 3.2: GCE model calculations by Wehmeyer et al. (2015) for [Eu/Fe]. The red crosses indicate values for observed stars with their error bars. The model stars are represented by the blue dots. Here, MHD SNe and NSMs are assumed to be the only r-process sites, with probabilities of $P_{NSM} = 3.8 \times 10^{-4}$, and $P_{MHD} = 10^{-3}$, respectively (i.e., the corresponding fractions of massive stars end up in NSMs or MHD SNe). The delay time needed for the two neutron stars in a binary system to spiral inwards is assumed to be 10 Myr.

Chapter 4

The r-Process

About half of the heavy elements beyond iron are produced by the *rapid neutron capture process (r-process*). It is known to operate in an environment with extremely high neutron densities and therefore proceeds along a path in the nuclear chart close to the neutron-drip line. Due to the high neutron density, it is characterized by fast neutron captures in comparison to β-decays. When the supply of free neutrons is depleted, the extremely neutron-rich isotopes undergo a series of β-decays to stability. The basic mechanism was already suggested by Burbidge et al. (1957) and Cameron (1957), who recognized that, in order to produce some of the stable nuclei on the neutron-rich side in the nuclear chart, fast neutron captures with subsequent β^--decays are the only possibility. Figure 4.1 demonstrates this concept on the example of a small excerpt of the nuclear chart. The contributions from the different nucleosynthesis processes towards the abundances of isotopes are indicated by the letters p, s, and r for each isotope. On the left-hand side the chemical elements are given and the mass number is also shown for each isotope. The well-known path of the *slow neutron capture process (s-process)* is indicated by blue arrows. The neutron-rich isotopes ^{134}Xe and ^{136}Xe are not produced by the s-process, because ^{133}Xe is unstable against β^--decay with a half-live of the order of a few days, much shorter than the average neutron-capture timescale in the s-process. In fact, ^{134}Xe and ^{136}Xe can only be produced when extremely neutron-rich nuclei decay towards stability, illustrated by the red dotted arrows. As a consequence, ^{134}Ba and ^{136}Ba are shielded from the decaying neutron-rich isotopes and are therefore s-only isotopes, i.e., they are produced exclusively by the s-process. The isotopes ^{130}Ba, ^{132}Ba, and ^{138}La cannot be produced by either the s- or the r-process. Instead, they are synthesized in a process operating on the neutron-deficient side of the nuclear chart (see e.g., Woosley & Howard 1978; Rauscher et al. 2002; Arnould & Goriely 2003; Fröhlich et al. 2006; Travaglio et al. 2011 for the synthesis of p-nuclei).

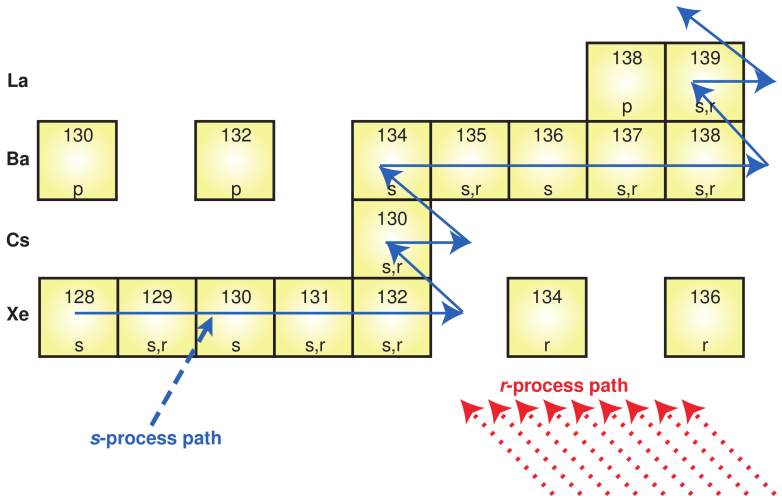

Figure 4.1: Schematic illustration of the working mechanisms of s- and r-process. Isotopes that are produced exclusively from one neutron capture process (p-only, s-only or r-only isotopes) play an important role in disentangling the contributions from each process. See text for further explanations (Figure from Sneden & Cowan 2003).

The r-process path proceeds through the very neutron-rich regions of the nuclear chart. Depending on the neutron density n_n and the temperature, it can even reach the neutron drip-line, i.e., where the neutron separation energy S_n becomes negative and neutron saturation is reached. Whenever a neutron shell is closed, however, both neutron capture cross sections as well as β-decay rates become significantly slower. As a consequence, the reaction flux is held up at the closed neutron shells and matter accumulates in the isotopes closest to stability, which act as waiting points along the reaction path. As the supply of free neutrons decreases, the r-process breaks down and the isotopes decay to stability. Since β-decays do not change the mass number A of a nucleus and r-process yields are often shown in dependence of A, the abundance distribution does not change greatly after this moment, which is referred to as the *freeze-out* of the r-process. In the abundance pattern of nuclei produced in the r-process, distinct peaks are visible which can be attributed to the closed shell waiting points. Figure 4.2 shows the correlation of the abundance peaks with the points where the reaction path (magenta line) meets the closed neutron shells (at $N = 50, 82, 126$).

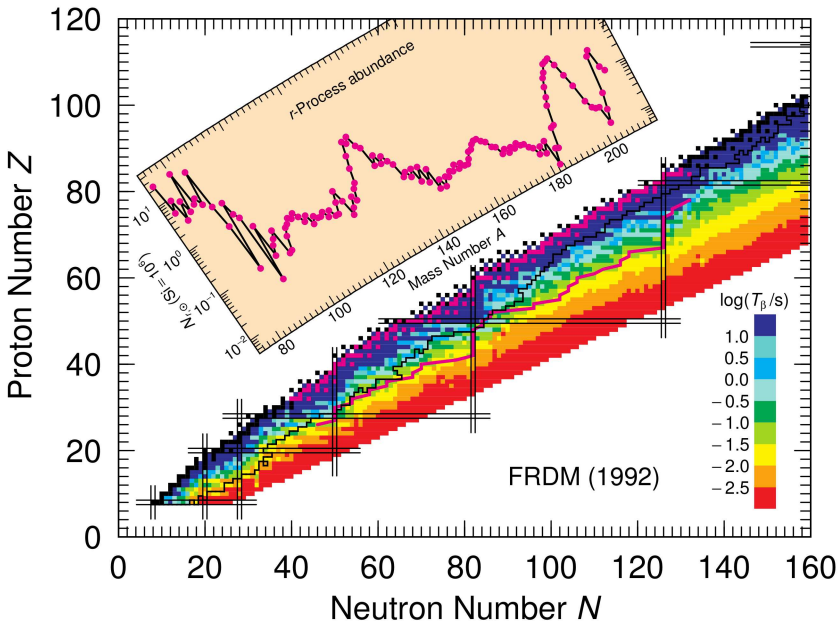

Figure 4.2: Timescales in [s] for β^--decays in the nuclear chart according to the FRDM (1992). Stable nuclei are coloured in black, stable nuclei that are produced by the r-process in magenta, and a typical r-process path is indicated by the magenta line. The observed solar system r-process abundances are plotted in the inset (scaled such that Si = 10^6). Figure from Möller et al. (1997).

4.1 Hot and Cold r-Process

In an isotopic chain, S_n becomes smaller with increasing neutron number N (not accounting for the odd-even staggering). This means that, for large enough temperatures, photons are energetic enough to dissociate neutrons and establish $(n,\gamma) - (\gamma,n)$ equilibria in each isotopic chain. For this *hot r-process* scenario, it is relatively simple to determine the isotopic abundances, since the abundance ratio $Y(Z,A+1)/Y(Z,A)$ depends only on the (velocity-integrated) neutron capture cross section $\langle\sigma v\rangle_{n,\gamma}(A)$ on nucleus (Z,A) and the photodisintegration term $\lambda_{\gamma,n}(Z,A+1)$ as well as the neutron density n_n:

$$\frac{Y(Z,A+1)}{Y(Z,A)} = \frac{\langle\sigma v\rangle_{n,\gamma}(A)}{\lambda_{\gamma,n}(Z,A+1)} n_n \,. \tag{4.1.1}$$

A relation between $\langle\sigma v\rangle_{n,\gamma}(A)$ and $\lambda_{\gamma,n}(Z,A+1)$ can be found using equation (2.1.30):

$$\lambda_{\gamma,n}(A+1) = \frac{2G(Z,A)}{G(Z,A+1)} \left(\frac{A}{A+1}\right)^{3/2} \left(\frac{m_u kT}{2\pi\hbar^2}\right)^{3/2} \langle\sigma v\rangle_{n,\gamma}(A) \exp[-S_n(A+1)/kT] \,, \tag{4.1.2}$$

which together with equation (4.1.1) gives

$$\frac{Y(Z,A+1)}{Y(Z,A)} = \frac{G(Z,A+1)}{2G(Z,A)}\left(\frac{A+1}{A}\right)^{3/2}\left(\frac{2\pi\hbar^2}{m_u kT}\right)^{3/2} n_n \exp[S_n(A+1)/kT]\,. \quad (4.1.3)$$

Using the above relation, isotopic abundances can be calculated if n_n, T, and the neutron separation energies S_n are known. The most abundant nuclei in each isotopic chain are so-called *waiting points*, as their β-decay half-lives determine at which timescale the next isotopic chain is populated. Following the prescriptions above, i.e., assuming $(n,\gamma)-(\gamma,n)$ equilibrium for each isotopic chain with subsequent β-decays of the most abundant nuclei leads to the *waiting point approximation*, which had been applied in early r-process calculations. If the temperature is not high enough to establish an $(n,\gamma)-(\gamma,n)$ equilibrium, the r-process is categorized as *cold*.

4.2 Possible Sites of the r-Process

Although the basic mechanism of the r-process and its requirements are known, we still lack direct observations of an astrophysical event as a confirmed r-process site. One of the key properties in r-process calculations is the initial neutron-to-seed ratio Y_n/Y_{seed}, where all nuclei above a certain mass number (e.g., $A \geq 16$) carry the label "seed". Knowing the average mass number of the initial composition $\langle A\rangle_i$, it is possible to estimate the final average mass number $\langle A\rangle_f$ using only the neutron-to-seed ratio:

$$\langle A\rangle_f = \langle A\rangle_i + Y_n/Y_{seed}\,. \quad (4.2.1)$$

Note that nucleons and nuclei up to $A = 4$ do not count towards $\langle A\rangle$.

Several factors have an impact on Y_n/Y_{seed}. Obviously, in order to obtain a large ratio, a high neutron abundance is beneficial. Since we always assume charge neutrality for our nucleosynthesis calculations, a high Y_n corresponds to a low electron fraction Y_e. On the other hand, Y_{seed} is low in environments with high entropy S (as the photons dissociate some of the existing seed nuclei into nucleons and α-particles) and/or short dynamical timescales τ_{dyn}, resulting in an α-rich freeze-out.

It has long been thought that the neutrino-driven wind in core-collapse supernovae could provide the conditions needed for the operation of the r-process. In addition to the high entropies encountered in such winds, interactions of material with neutrinos have an effect on Y_e via

$$\begin{aligned} \nu_e + n &\rightarrow p + e^- \\ \overline{\nu}_e + p &\rightarrow n + e^+\,. \end{aligned} \quad (4.2.2)$$

Otsuki et al. (2000) calculated the r-process requirements with respect to entropy per baryon and the dynamical timescale of the expansion (see Figure 4.3) for ν-driven winds and the combinations that would result in the production of the second and the third r-process peak material, respectively. They define τ_{dyn} as the time it takes for the expanding material to cool down from a temperature of $T_1 = 5\times10^9$ K to $T_2 = T_1/e \approx 1.84\times10^9$ K, which they correlate to the time span where new seed nuclei can be produced via the triple-α reaction and subsequent α captures:

$$\tau_{dyn} = \int_{T_1}^{T_2} \frac{dr}{u}\,, \tag{4.2.3}$$

where u is the radial component of the four-velocity in the Schwarzschild geometry. However, more recent hydrodynamic simulations suggest that the required conditions cannot be met in this scenario (see e.g., Arcones et al. 2007; Fischer et al. 2010; Hüdepohl et al. 2010; Arcones & Janka 2011).

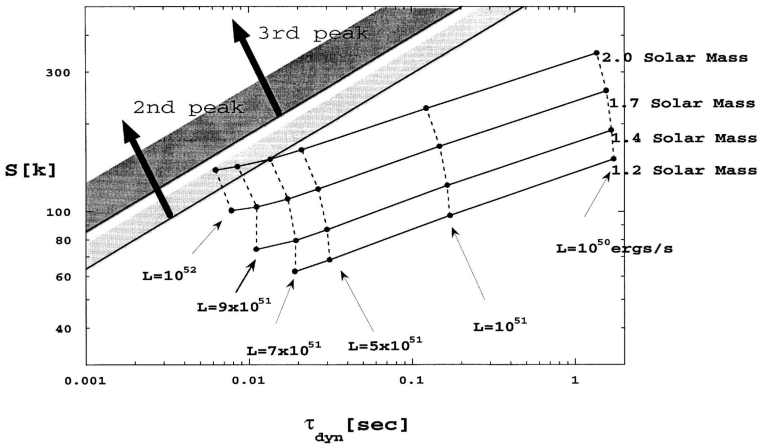

Figure 4.3: Conditions necessary to synthesize the second (lower band) and the third r-process peak (upper band) with respect to entropy per baryon and the dynamical timescale τ_{dyn} according to Otsuki et al. (2000). The lines connecting the grid points refer to cases with equal neutrino luminosity L (vertical lines) and equal neutron star mass (horizontal).

Other sites related to regular core-collapse supernovae have been proposed, among them shocked surface layers in an O-Ne-Mg progenitor (Ning et al., 2007; Eichler et al., 2012) and a neutrino-induced r-process in the He shell at low metallicities (Epstein et al., 1988; Banerjee et al., 2011), both of which could host an r-process in only slightly neutron-rich conditions due to the low amount of seed nuclei. There are however considerable problems associated to these sites, as the conditions are not realized in hydrodynamical simulations (high velocities in the shocked surface layers), or the site is only viable for low metallicities and does not lead to a good

reproduction of the solar r-process abundance pattern (in the case of the ν-induced r-process in the He shell).

Magneto-hydrodynamically driven (MHD) SNe (Winteler et al., 2012; Käppeli, 2013) are a rare class of CCSNe, which eject matter in two relatively neutron-rich polar jets. This scenario looks promising, especially as an early producer of r-process material in a young galaxy. It is discussed further in section 7.3.

A natural r-process site seem to be binary neutron star mergers (NSMs) and mergers between a neutron star and a black hole, since a lot of neutron-rich material becomes gravitationally unbound in these high-energetic collisions. Hydrodynamical simulations of these events confirm that the dynamical ejecta are extremely neutron-rich ($(Y_n/Y_{seed})_i \approx 1000$). In this environment, the reaction path runs along the neutron drip-line and the resulting abundance pattern is very robust with respect to the exact hydrodynamic evolution. Figure 4.4 illustrates this fact on the example of a few trajectories of a NSM with two 1.4 $M_\odot$ neutron stars from the set of Rosswog et al. (2013).

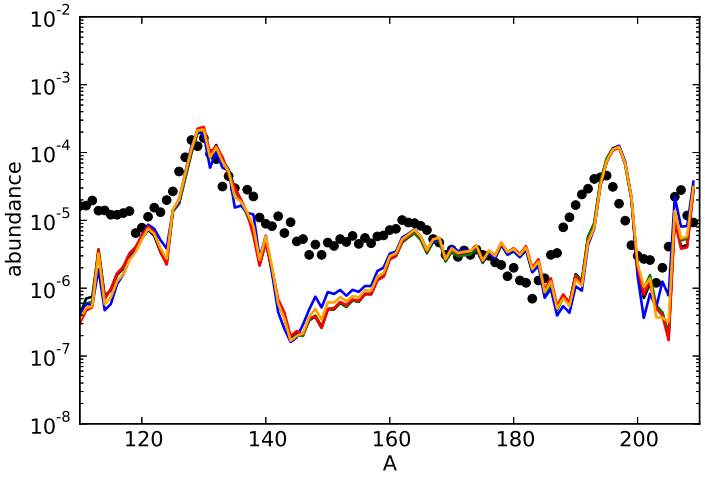

Figure 4.4: Final abundance distributions from different trajectories belonging to a neutron star merger of two 1.4 $M_\odot$ neutron stars from Rosswog et al. (2013). The robustness of the nucleosynthesis results are caused by the extremely high neutron-to-seed ratios, which guarantee that the reaction path runs close to the neutron drip-line. The black dots represent the solar r-process abundances reported in Sneden et al. (2008)

While the high neutron-to-seed ratio guarantees the reliable production of r-process nuclei up to the heaviest stable nuclei, it also poses some challenges to nucleosynthesis network calculations. In particular, there are large uncertainties still concerning the masses of the neutron-rich nuclei involved in the reaction path, and some of

the features in the abundance pattern are sensitive to the choice of theoretical mass model. Furthermore, the nature of nuclear fission for these highly neutron-rich nuclei is not yet fully understood and there exist large differences in predictions of the fission products.

In addition to the dynamical ejecta which become unbound during the collision, neutron-rich material can be ejected from the accretion disk in the aftermath of a NSM by a neutrino-driven mechanism. Although Y_e appears to be larger, simulations show that it is still sufficiently low to account for an r-process producing at least the r-nuclei with small mass numbers.

The robustness of nucleosynthesis results in NSMs agrees very well with observations of metal-poor stars, which show that the heaviest r-elements are produced in a pattern that is remarkably similar from star to star. A breakdown of r-only abundances in six metal-poor stars from the galactic halo is shown in Figure 4.5. Different symbols are used for the different stars and their abundances are vertically offset for display purposes. The solar system r-only abundances are represented by the blue lines. In the lower parts of Figure 4.5 the individual abundance offsets (b) and offsets averaged over all six stars (c) are shown. In all cases the offsets are calculated with respect to the solar system abundances and normalized to zero at Eu. For $Z \geq 56$ the relative abundances are in very good agreement to the solar abundances, arguing for the robust nature of the r-process producing these elements, and consequently supporting neutron star mergers as a viable r-process site.

However, four of the stars discussed here have metallicities [Fe/H] ≈ -3, which means that they must have formed very early in the history of the galaxy. Neutron star mergers appear relatively late in the timeline of nucleosynthesis events, posing a problem to explain r-process abundances in these old stars.

Recently, a high-energetic gamma-ray burst event has been observed, followed by a light curve that can be attributed to the radioactive decay of nuclei produced in an r-process (Tanvir et al., 2013; Piran et al., 2014; Grossman et al., 2014). This discovery of a 'macronova' (or 'kilonova'), together with the very recent first-time measurements of gravitational waves (Abbott et al., 2016), pushes the door wide open for future observations of binary neutron star mergers and a possible confirmation of NSMs as an r-process site.

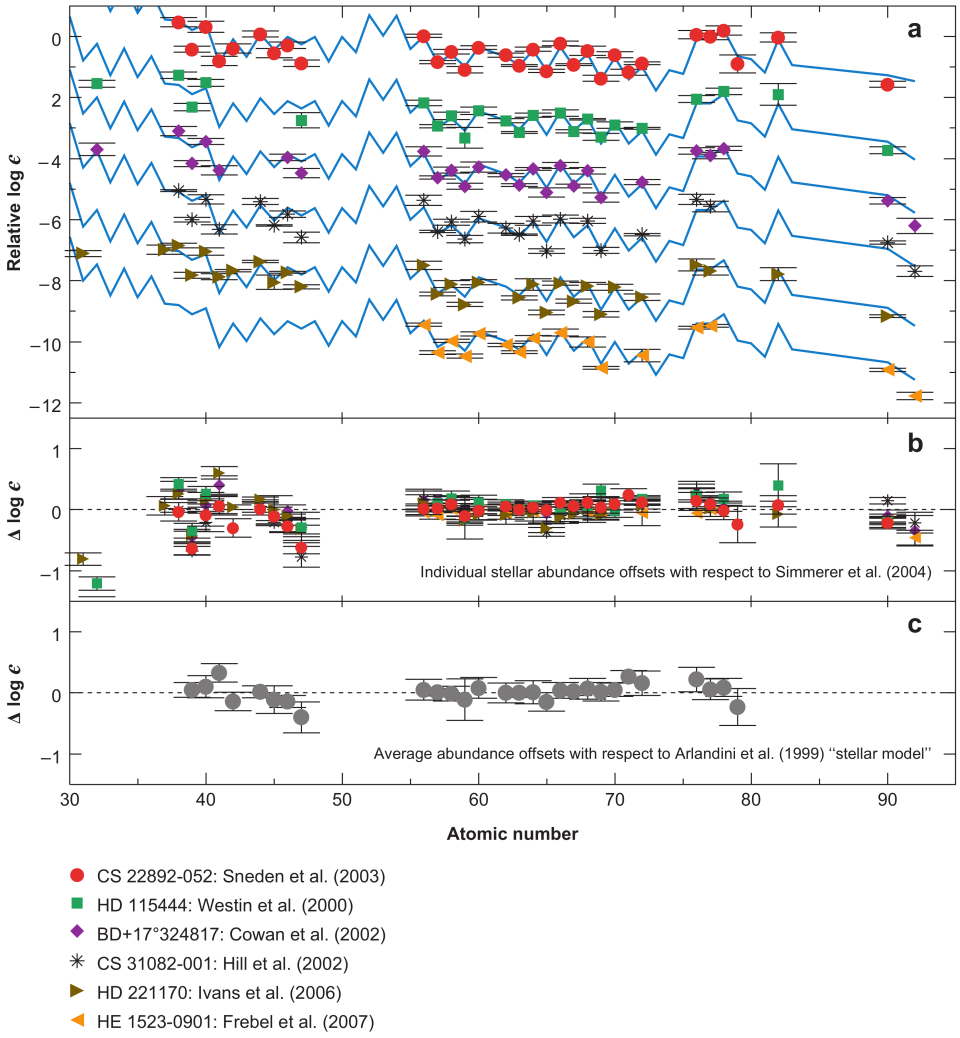

Figure 4.5: (a) Abundances of r-only elements in six galactic halo stars and comparisons to the solar system r-only abundances (blue lines), scaled to the respective Eu value. The vertical offset is for display purposes only. (b) Individual deviations of the stellar abundances from the solar r-only abundances reported in Simmerer et al. (2004). (c) Average deviations with respect to the Arlandini et al. (1999) solar abundance predictions. All the data in (b) & (c) are scaled to $\Delta \log \varepsilon(Eu) = 0$. Figure from Sneden et al. (2008).

Chapter 5

Fission

When moving up the nuclear chart to higher proton and neutron numbers, nuclei not only become more massive, but also increase in volume. As the strong force that holds the nucleons together has a very limited range (one to a few femtometers), it only acts between neighbouring nucleons. The Coulomb repulsion of the protons, however, has a long range and gains in influence with increasing proton number. Therefore, heavier nuclei are generally less bound and can easily deform. Some deformations lead to the formation of a neck (see Figure 5.4), and eventually to the splitting into two lighter fragments. For most nucleosynthesis events in the universe fission can be neglected, because the required mass numbers are not reached. In an r-process scenario with a large neutron-to-seed ratio ($Y_n/Y_{seed} \gtrsim 200$), however, fissioning nuclei are produced, and a realistic treatment of fission is necessary to determine the final abundances of the ejecta in such an event. If Y_n/Y_{seed} exceeds 200, freshly produced fission fragments can proceed to capture neutrons until they themselves become unstable and undergo fission. This is called *fission cycling*. The presence of fission cycling can be verified by tracking the average mass number $\langle A \rangle$ or, similarly the average proton number $\langle Z \rangle$. Each notable decrease in $\langle A \rangle$ or $\langle Z \rangle$ can be attributed to a fission cycle (see Fig. 5.1). If the initial Y_n/Y_{seed}, $\langle A \rangle_i$, and $\langle A \rangle_f$ are known, the number of fission cycles N_{FC} can be estimated by

$$N_{FC} = \log_2 \left(\frac{\langle A \rangle_i + (Y_n/Y_{seed})_i}{\langle A \rangle_f} \right), \tag{5.0.1}$$

where the indices i and f denote the initial and final values.

The fission process is still far from being fully understood, despite many decades of dedicated research. The first discovery of fission was reported in 1939, when barium isotopes were detected as products of the irradiation of natural uranium with neutrons (Hahn & Strassmann, 1939). At the same time this was also the first indication for asymmetric fission (i.e., fission fragments with different proton and/or

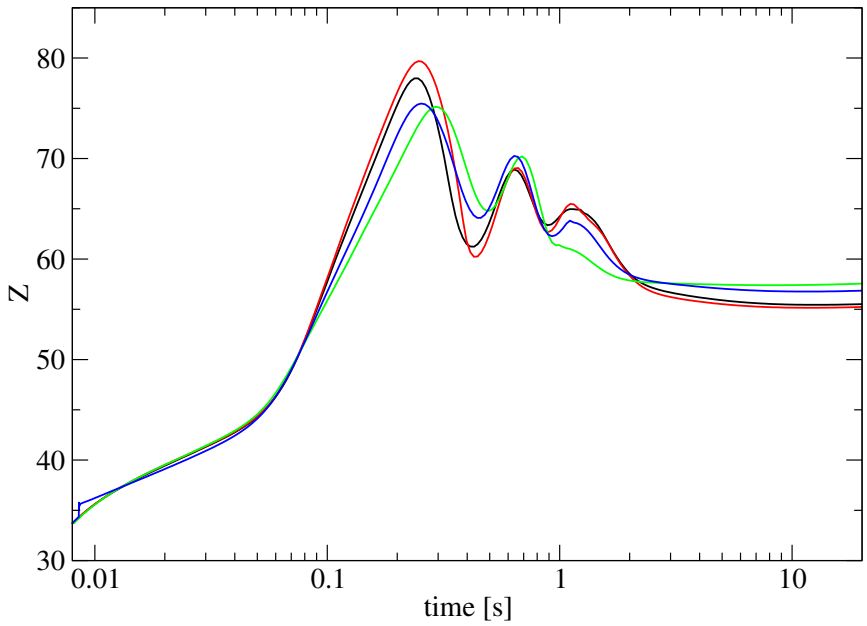

Figure 5.1: Average proton number $\langle Z \rangle$ for four different trajectories in a neutron star merger simulation from Rosswog et al. (2013). The fission cycles are recognisable by the decreases in $\langle Z \rangle$.

neutron numbers), which could not be explained by the liquid-drop model. The introduction of the spherical-shell model 10 years later (Mayer, 1949) helped solve this problem. Soon after, the mass distribution of fission fragments was linked to shell closures in the daughter nuclei (Fong, 1956). It was still a long way, however, to the development of successful theoretical models. The first quantitative predictions of fission products were made by Wilkins et al. (1976), using a statistical scission-point model (see Steinberg & Wilkins 1978 for the impact on r-process nucleosynthesis). Their model was able to explain the dependence of fission on the nuclear structure remarkably well. Some global characteristics of fissioning nuclei can be observed in experiments (Fig. 5.2). The light nuclei ($A < 226$) show a symmetric fission behaviour, while fission of heavier nuclei ($226 < A < 256$) produces an asymmetric fragment distribution. Close to $A = 260$ fission again becomes symmetric, with both fragments around $A = 132$.

A potential energy barrier prevents a stable nucleus from decay, and in the case of fission, the barrier is usually referred to as *fission barrier*. For some nuclei two potential barriers are between the bound state and the scission point. Such a shape in the potential energy landscape is called double-humped barrier. For fissioning nuclei there are three possibilities (modes) to overcome the fission barrier. First, quantum mechanics allows the nucleus to tunnel through. This mode is called spontaneous fission. Another possibility involves the caption of a neutron, which

excites the compound nucleus to an energy level above its fission barrier. In order to determine which nuclei undergo neutron-induced fission, one can compare the neutron separation energy S_n with the fission barrier B_f. If the fission barrier is lower than S_n, the compound nucleus (after neutron capture) is in an excited state higher than the fission barrier and fission occurs. A comprehensive comparison of the fission barrier with S_n has been done in Petermann et al. (2012) for two mass models and their corresponding fission barrier predictions: FRDM (1992) and ETFSI (see Figure 5.3). It shows considerable differences for the two mass models. In particular, for the FRDM the reaction path is ended by n-induced fission (negative values for $B_f - S_n$) around $Z = 95$, while for ETFSI a narrow bridge of positive $B_f - S_n$ values may allow the reaction path to proceed to larger masses and the production of superheavy elements (SHE). Finally, a β-decay can also leave the nucleus in an excited state higher than the fission barrier, which results in β-delayed fission. An extensive discussion on the individual fission modes can be found in Petermann et al. (2012).

5.1 Understanding Fission: The Multi-Dimensional Potential-Energy Surface

A good understanding of the fission process can be obtained by calculating the potential-energy landscape as a function of several deformation parameters describing the shape of the fissioning nucleus (e.g., Möller et al. 2001) within the framework of a theoretical mass model. The features of the landscape (peaks, valleys, saddle-points) are shaped mainly by the microscopic corrections to the energy potential due to shell effects in the nuclear structure. On the transition from parent nucleus to two or more separated fragments, ridges in the landscape correspond to

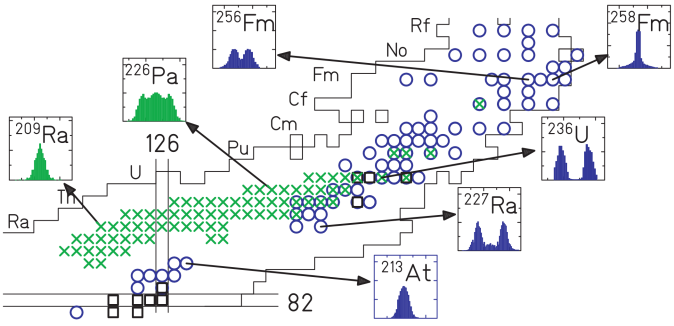

Figure 5.2: Positions of nuclei in the nuclear chart for which fission fragment distributions have been experimentally determined, either as a function of proton number (crosses) or mass number (circles). The insets show the mass distributions of the fission fragments. Figure from Schmidt et al. (2008).

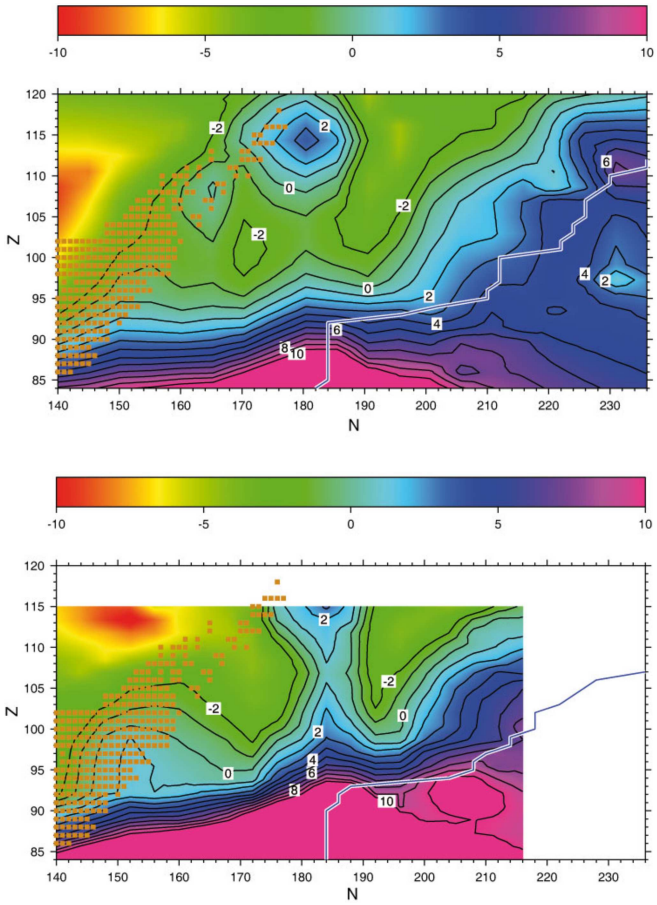

Figure 5.3: Difference between fission barriers B_f and S_n for the FRDM (top) and ETFSI (bottom) mass models, both with corresponding fission barrier predictions. The values are given in MeV. Negative $B_f - S_n$ values mark the regions where neutron-induced fission is expected upon neutron capture. Figure from Petermann et al. (2012).

potential energy barriers that have to be overcome, the highest of which is usually referred to as the fission barrier. Magic neutron or proton numbers in the nascent fragments can be seen as valleys long before the actual scission point, which explains why fragments with magic numbers are often preferred. Möller et al. (2001) calculate the potential-energy landscape as a function of five independent shape parameters: elongation (expressed by the charge quadrupole moment Q_2), neck diameter d, left and right nascent fragment deformation ε_{f1} and ε_{f2}, and mass asymmetry α_g (see Figure 5.4). In their chosen resolution, this leads to a grid with 2 610 885 grid points.

Features of the potential-energy landscape and the most likely path from ground state to scission can be found using the so-called *flooding algorithm* (Möller et al.,

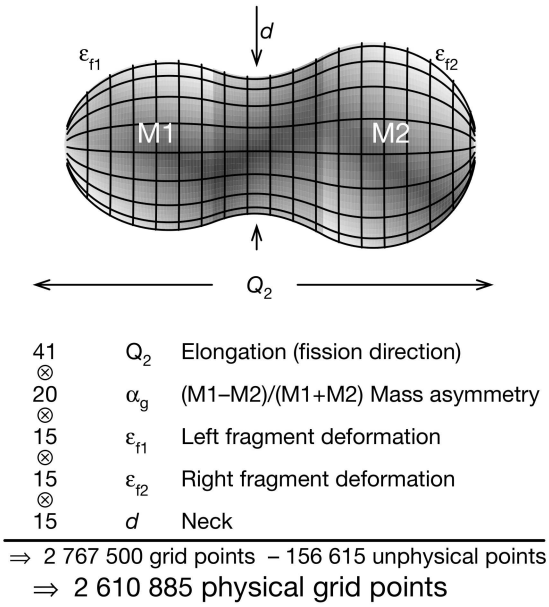

Figure 5.4: Shape parameters of fissioning nuclei used in Möller et al. (2001). See text for explanation.

2001), where imaginary water flows are applied. When a state of separation is beginning to fill with water, the corresponding fission barrier can be identified by comparing with the global water level at this time. Their calculations are based on the FRLDM (Möller et al., 1995), and they successfully reproduce various experimental observations, such as fission fragment distribution yields, multi-modal fission in nuclei around $A = 230$, and kinetic energies of the fragments.

5.1.1 Calculating ETFSI fission barriers

A similar approach has been used in Mamdouh et al. (1998) for the determination of fission barriers compatible with the ETFSI model. The left-right symmetry condition that has been used in the mass formula is relaxed here, allowing for a better description of deformations. However, axial symmetry is preserved. The so-called (c, h, α) parametrization is used (see Brack et al. 1972), allowing for all deformed shapes of a given nucleus, including total break-up, to be described continuously, starting from a spherical configuration.
First, a reference surface S_0 is introduced. It more or less corresponds to the actual surface of the fissioning nucleus or the surfaces of the two fragments resulting from fission. The reference surface always encloses the same volume, regardless of the

deformation. Its radius in the spherical configuration is

$$R = \frac{N}{N+Z}C_n + \frac{Z}{N+Z}C_p, \tag{5.1.1}$$

with N and Z the number of neutrons and protons, respectively. The general shape of S_0 is described by

$$\eta^2 = (c^2R^2 - z^2)\left(A + \frac{\alpha}{cR}z + \frac{B}{c^2R^2}z^2\right), \quad B \geq 0 \tag{5.1.2}$$

and

$$\eta^2 = (c^2R^2 - z^2)\left(A + \frac{\alpha}{cR}z\right)\exp\left(\frac{Bc}{R^2}z^2\right), \quad B < 0, \tag{5.1.3}$$

where η and z are cylindrical coordinates with the symmetry axis along the z-axis and α determining the left-right asymmetry (with $\alpha = 0$ denoting symmetry). A and B are additional deformation parameters. The elongation parameter c is defined in a way that the length of the nuclear system in the direction of z is always $2cR$, so S_0 lies in the interval $-cR \leq z \leq cR$. The exact shape of S_0 now depends on the factor

$$f_+ = A + \frac{\alpha}{cR}z + \frac{B}{c^2R^2}z^2 \tag{5.1.4}$$

for $B \geq 0$ and on

$$f_- = A + \frac{\alpha}{cR}z \tag{5.1.5}$$

for $B < 0$, respectively. If $f_+ > 0$ throughout the interval $-cR \leq z \leq cR$, then S_0 consists of one single piece (= one nucleus), however when f_+ has two zeroes inside the interval, S_0 is split into two separate closed pieces, meaning the nucleus has fissioned. Meanwhile f_- can never have two zeroes, as it is no quadratic factor, so for $B < 0$ there will never be more than one closed piece in the interval.

Under the condition that S_0 always encloses the same volume $4\pi R^3/3$, expressions for c can be found:

$$c = \left(A + \frac{B}{5}\right)^{-1/3} \tag{5.1.6}$$

for one single nucleus, and

$$\begin{aligned} c = \Big(A + \tfrac{B}{5} - \tfrac{3b}{2}\Big\{A\left(1 - a^2 - \tfrac{b^2}{3}\right) + B\left(a^2 + \tfrac{b^2}{3} - a^4 - 2a^2b^2 - \tfrac{b^4}{5}\right) \\ +\alpha a(1 - a^2 - b^2)\Big\}\Big)^{-1/3} \end{aligned} \tag{5.1.7}$$

for two fragments, where a and b are defined as

$$\begin{aligned} a &= -\frac{\alpha}{2B} \\ b &= \frac{\sqrt{\alpha^2 - 4AB}}{2B}\,. \end{aligned} \tag{5.1.8}$$

A further second parameter h can be introduced as

$$h = \frac{B}{2} + \frac{1-c}{4}\,, \tag{5.1.9}$$

allowing the deformation to be described by the parameters (c, h, α).

To determine the fission barriers one first has to calculate the deformation energies of the nucleus depending on the deformation parameters. For instance, for the two parameters (c, h) one can determine the energy values at certain grid points in the (c, h) plane and then interpolate. A contour plot of the energy will reveal the positions and the heights of the fission barriers. If there are more than two deformation parameters, things are more complicated. The procedure applied can be compared to water dripping from an open tap into the ground-state minimum (which has to be located first). By slowly increasing the water level the water will pour into other (local) minima. As soon as the so-called valley of fission is reached by the water, the fission barrier has been overcome and the height of the water level at that time (measured from the ground-state minimum) corresponds to the height of the highest fission barrier. Only for $Z \geq 90$ more than one barrier can be observed. For the lighter elements only one barrier is observed, and it is safe to assume that it is the outermost, as the inner barrier(s) are effectively concealed. According to Mamdouh et al. (1998), however, only the primary (i.e. the highest) fission barrier is relevant for r-process nucleosynthesis. Overall the agreement of the ETFSI barrier calculations with observations is quite good if the barrier does not exceed 10 MeV. For higher barriers the deviations are larger, but since the neutron separation energy of r-process nuclei usually is around 4 MeV, a fission barrier in excess of 10 MeV means that the nucleus in question does not undergo fission but will rather eject a neutron.

5.2 Fission in Nuclear Networks: Fission Fragment Distribution Models

The content of this section is part of the publication Eichler et al. (2015a). In our nuclear network, fission reactions are included in a similar way to other decays (spontaneous and β-delayed fission) and neutron-induced processes (n-induced fission). However, to account for the fact that each fissioning nucleus can split in many different possible fragments, we additionally make use of fission fragment distribution models. These models statistically predict the fragment yields for each fission reaction. Over the years, a multitude of fission fragment distribution models has been developed. We compare four different models and their impact on the final abundance distribution in section 6.2. The fission fragment distribution depends on the nuclear structure of the fissioning nucleus as well as that of the fission products, e.g., the shell structure of nuclei far from stability. The fission

products can be predicted statistically by assigning a pre-determined probability to each possible fission channel. Rates for the various fission channels considered and the associated yield distributions are crucial for r-process studies in NSMs. In each fission reaction there is a possibility of several fission neutrons to be emitted. While the number of fission neutrons has been measured to be $2-4$ for experimentally studied nuclei, it is known to increase with mass number as heavy nuclei become more neutron-rich (Steinberg & Wilkins, 1978). Additional neutrons can be emitted as the fission fragments decay towards the r-process path (Martínez-Pinedo et al., 2006). Recent advances are discussed in Tatsuda et al. (2007), Panov et al. (2008), Kelic et al. (2008), Goriely et al. (2013), and Goriely (2015a), with differences for the predicted mass distributions revealing the remaining uncertainties in present fission calculations.

For our NSM nucleosynthesis calculations we employ four different fission fragment distribution models: (a) Kodama & Takahashi (1975), (b) Panov et al. (2001), (c) Panov et al. (2008), and (d) ABLA07 (Kelic et al., 2008, 2009). The first one is a relatively simple parametrization that does not take into account the release of neutrons during the fission process. The second and third are parametrizations guided by experimental data. The number of released neutrons in Panov et al. (2008) has been estimated as a function of charge and mass number of the fissioning nucleus and can reach 10 per fragment for nuclei near the drip line. The ABLA07 model is based on a statistical model considering shell effects in the fragments from theoretical predictions and has been tested to provide an accurate description of known fission data including the number of released neutrons (Benlliure et al., 1998; Gaimard & Schmidt, 1991; Kelic et al., 2009). It also includes the reproduction of fragment distributions from extended heavy ion collision yields (Kelic et al., 2008), and therefore goes much beyond the areas in the nuclear chart where spontaneous, β-delayed or neutron-induced fission yields are known experimentally. In Fig. 5.5 (and the related caption) we provide the fission fragment distributions as a function of A as well as the number of released neutrons for ^{274}Pu ($Z = 94$). Note that the model by Kodama & Takahashi (1975) does not lead to any neutron release and Panov et al. (2008) predicts the largest number of released neutrons. It can also be seen that the predicted fragments in the Panov et al. distributions do not extend beyond $A = 140$, which will be important in section 6.2.2.

Other applications of recent fragment distribution models (called GEF and SPY) are employed in Goriely (2015a). However, these models have either been restricted so far to not very neutron-rich nuclei ($A/Z < 2.8$ and $N < 170$; GEF), or have not yet been the subject of the same severe tests as ABLA07 (both GEF and SPY). Based on NSM simulations of Rosswog et al. (2013), we present a comparison of the abundance features resulting from utilizing the different fission fragment models in section 6.2 (see also Eichler et al. 2016).

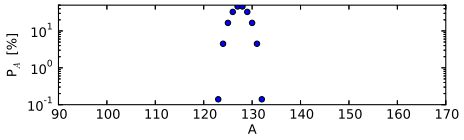

(a) Panov et al. (2008)

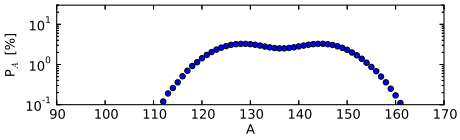

(b) Kodama & Takahashi (1975)

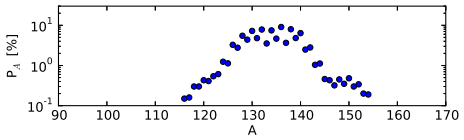

(c) ABLA07

Figure 5.5: Fission fragment distributions for the models introduced in the text, here for the case of neutron-induced fission of ^{274}Pu. For this reaction Panov et al. (2008) predicts 19, ABLA07 7 released fission neutrons. Kodama & Takahashi (1975) do not predict any fission neutrons. For Panov et al. (2001) neutrons can be released if the fragments would lie beyond the neutron dripline. The distribution for Panov et al. (2001) consists only of two products with $A_1 = 130$ and $A_2 = 144$.

Chapter 6

Neutron Star Mergers as R-Process Site: Accomplishments and Issues[1]

As of today, the astrophysical site(s) of the r-process remain(s) uncertain, but metal-poor stars with enriched r-process material offer valuable clues about the nature of the r-process source(s). Observations reveal that the [Eu/Fe] ratios of the oldest stars are scattered over several orders of magnitude, while the scatter decreases for younger and correspondingly less metal-poor stars (see Figure 3.1). Europium is exclusively produced by the r-process and is therefore used as an indicator of r-process material enrichment. On top of that, the overall element abundance pattern of heavy ("strong") r-process nuclei follows the solar one with remarkable accuracy (Figure 4.5). In combination with the large scatter in [Eu/Fe] for low-metallicity stars, this points to a rare event, responsible for the production of heavy r-process material (Sneden et al., 2008; Roederer et al., 2012). On the other hand, various intermediate-mass r-process elements up to Europium are observed in almost all stars, albeit at lower levels (Honda et al., 2007; Roederer, 2013). This argues for an additional frequent event which can account for such a "weak" r-process signature. Regular core-collapse supernovae may be the origin, as the neutrino wind could generate a slightly neutron-rich environment (Roberts et al., 2012; Martínez-Pinedo et al., 2012), but does not provide the entropies required for the operation of a strong r-process in slightly neutron-rich conditions.

Compact object mergers have long been suspected to be a possible site for r-process nucleosynthesis (Lattimer & Schramm, 1974; Meyer, 1989; Freiburghaus et al., 1999; Roberts et al., 2011; Goriely et al., 2011; Korobkin et al., 2012; Bauswein

[1]The content of this chapter has been published in Eichler et al. (2015a).

et al., 2013; Rosswog et al., 2014). For recent results see also Just et al. (2015), Mendoza-Temis et al. (2015), Wanajo et al. (2014), and Martin et al. (2015). As discussed above, the combination of very low-Y_e material and rapid expansion of the ejecta guarantees the occurrence of a strong r-process. Several studies (Goriely et al., 2011; Korobkin et al., 2012; Bauswein et al., 2013) uncovered remarkable astrophysical robustness of the abundance yields produced in the dynamical ejecta of neutron star mergers (NSM) and mergers of a neutron star with a black hole for a given nuclear input (see also Figure 4.4). This insensitivity of the abundance pattern to the parameters of the merging system is explained by an extremely low-Y_e environment, which guarantees the occurrence of several fission cycles before the r-process freezes out. However, recent NSM simulations that also account for the neutrino-driven wind and/or viscous disk ejecta at a later stage of the merger find a much broader range of Y_e-values for the ejecta (Rosswog et al., 2014; Just et al., 2015; Perego et al., 2014; Wanajo et al., 2014).

Here, we revisit the nucleosynthesis in the dynamical ejecta of NSMs of Korobkin et al. (2012), by using the ETFSI–Q (Aboussir et al., 1995; Pearson et al., 1996) and HFB–14 (Goriely et al., 2008, 2009) mass models in addition to the FRDM (Möller et al., 1995). Our main focus is the effect of fission on the r-process path through the very neutron-rich, unstable nuclei, utilizing corresponding fission barriers (Myers & Swiatecki 1999 for FRDM and Mamdouh et al. 1998 for ETFSI–Q and HFB–14, as discussed in Panov et al. 2010) and the four fission fragment distribution predictions introduced in section 5.2. We also follow the decay back to stability during the r-process freeze-out and the competition between late neutron captures and neutron release by fission and β-decays of heavy nuclei (see similar discussions of freeze-out effects without including fission in Mumpower et al. 2012 and references therein). Late neutron captures have a direct effect on the final position of the third r-process peak (also seen in Goriely et al. 2013 and Goriely 2015a). To study the dependence of the final abundance distribution on the freeze-out characteristics, we pick a typical trajectory from the same database of trajectories[2] that was used in Korobkin et al. (2012). We include the following three fission modes: spontaneous, β-delayed and neutron-induced fission, as described in detail in Panov et al. (2008, 2010) and Petermann et al. (2012).

6.1 Nucleosynthesis Calculations

6.1.1 Basic Input and Conditions in Ejecta Trajectories

We utilize the extended nuclear network WINNET (Winteler, 2011; Winteler et al., 2012) with more than 6000 isotopes up to Rg. Our sets of reaction rates utilized

[2]http://compact-merger.astro.su.se/

are based on masses from the FRDM (Möller et al. 1995), the ETFSI–Q model (Aboussir et al. 1995; Pearson et al. 1996), both in combination with the statistical model calculations of Rauscher & Thielemann (2000) for $Z \leq 83$, and on the HFB–14 model (Goriely et al., 2008, 2009), respectively. Theoretical β-decay rates are taken from Möller et al. (2003), experimental data from the nuclear database NuDat2 (2009). The neutron capture rates on heavy nuclei ($Z > 83$) as well as the neutron-induced fission rates are from Panov et al. (2010), while the β-delayed fission rates are taken from Panov et al. (2005). In our calculations, we refer to the combined application of these basic sets of reaction rates as *original*. We also test the effect of very recent advances in β-decay half-life predictions by Marketin et al. (2015) and Panov et al. (2015).

We have performed r-process calculations for a neutron star merger scenario with two 1.4 $M_\odot$ neutron stars (Rosswog et al., 2013; Korobkin et al., 2012). We use 30 representative fluid trajectories, covering all the conditions in the ejected matter and providing the temperature, density and electron fraction within the ejected material up to a time of $t_0 = 13$ ms. We start our nucleosynthesis calculations after the ejecta have begun to expand and the temperature has dropped to 10 GK. For $t > t_0$ we extrapolate, using free uniform expansion for radius, density and temperature:

$$r(t) = r_0 + tv_0 \tag{6.1.1}$$

$$\rho(t) = \rho_0 \left(\frac{t}{t_0}\right)^{-3} \tag{6.1.2}$$

$$T(t) = T[S, \rho(t), Y_e(t)], \tag{6.1.3}$$

with radius r, time t, velocity v, density ρ, temperature T, entropy S and electron fraction Y_e of the fluid element. The index 0 denotes the values at t_0. The temperature is calculated at each timestep, using the equation of state of Timmes & Swesty (2000).

Our network accounts for heating due to nuclear reactions (Freiburghaus et al., 1999), using

$$kT\frac{dS}{dt} = \epsilon_{th}\dot{q} \tag{6.1.4}$$

to calculate the entropy increase caused by thermal heating, where $\dot{q}$ is the energy generated due to nuclear reactions. We choose a heating efficiency parameter of $\epsilon_{th} = 0.5$ (introduced in Metzger et al. 2010a), corresponding to about half of the β-decay energy being lost via neutrino emission. The efficiency for neutron captures and fission processes should be higher, as none of the released energy escapes. However, the energy release in neutron captures is small due to small neutron-capture Q-values along the r-process path (compared to large β-decay Q-values), and the abundances of heavy fissioning nuclei are small in comparison to the majority of nuclei in the r-process path. Thus, while the heating via beta-decays dominates, the exact value of ϵ_{th} is difficult to determine. In the case of

extremely neutron-rich dynamic NSM ejecta, the final abundances are, however, quite insensitive to its value (Korobkin et al., 2012).

6.2 Results

This section focuses on several aspects entering r-process nucleosynthesis in NSM ejecta: a comparison of different fission fragment distribution and mass models and their impact on the second r-process peak (section 6.2.1), a discussion of the late capture of fission neutrons and the impact on the position of the r-process peaks (section 6.2.2), and the overall combined effect of mass models, fission, and β-decay half-lives on the abundance distribution for $A > 120$, i.e., including the second and the third peak (section 6.2.3).

6.2.1 The Effect of Fission Fragment Distributions

The effect of adopting different fission fragment distribution models, all in combination with the FRDM mass model for the r-process calculations, is illustrated in Fig. 6.1. It shows final abundances of the NSM ejecta in the atomic mass range $A = 110 - 210$ for the four models introduced in section 5.2. Two of the fragment distributions (Panov et al., 2001; Kodama & Takahashi, 1975) have already been used for NSM calculations before (Korobkin et al., 2012) (see also Bauswein et al. 2013, utilizing the latter of the two, but with fragment mass and charge asymmetry derived from the HFB–14 predictions; see Goriely et al. 2011), while the other two (Panov et al., 2008; Kelic et al., 2008) have been newly implemented for the present calculations. All our results are compared to the solar r-process abundance pattern (Sneden et al. 2008).

For the fissioning nuclei produced in the present r-process simulations, our fission models mainly result in fission fragments in the mass range $100 \leq A \leq 160$. Therefore, it is no surprise that the largest differences between the models are found around the second peak. The results obtained with the two Panov models (Fig. 6.1a) show a drastic underproduction of the mass region beyond the second peak ($A \approx 140 - 170$) by a factor of 10 and more, due to the dominance of the symmetric fission channel and a large number of released neutrons. The Kodama & Takahashi model, in contrast, shows an overproduction of these nuclei and fails to produce a distinct second peak. The ABLA07 model (dashed line in Fig. 6.1b) shows the best overall agreement with the solar r-process abundance pattern (for the chosen mass model FRDM), leading only to an underproduction of $A = 140 - 170$ nuclei by a factor of about 3. The predicted fragments in the Panov et al. distributions do not extend beyond $A = 140$ (see Figure 5.5) and thus lead to the strongest underproduction in the mass range $A = 140 - 170$.

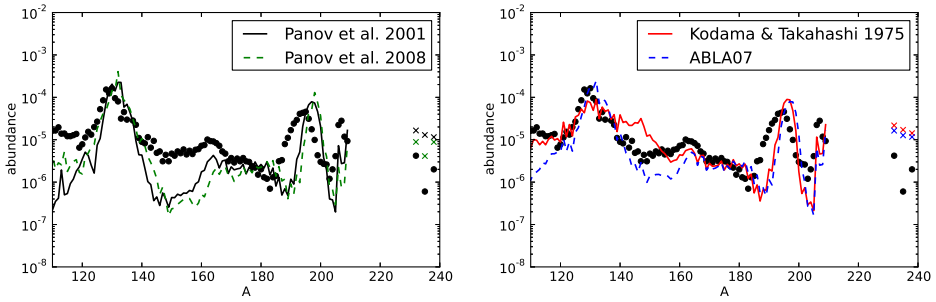

(a) (b)

Figure 6.1: Final abundances of the integrated ejecta around the second and third peak for a NSM (Rosswog et al., 2013; Korobkin et al., 2012) at a simulation time $t = 10^6$ s, employing the FRDM mass model combined with four different fission fragment distribution models (see text). For reasons of clarity the results are presented in two graphs. The abundances for Th and U are indicated by crosses. In the left-hand panel the lower crosses belong to the Panov et al. (2008) model (dashed line), while the lower crosses in the right-hand panel belong to the ABLA07 distribution model (dashed line). The dots represent the solar r-process abundance pattern (Sneden et al., 2008).

Figure 6.2 demonstrates the importance of fission in our calculations, indicating the fission rates from two fission modes (neutron-induced and β-delayed fission) at $t =$ 1s. It is obvious that the mass region with $Z = 93-95$ and $N = 180-186$ dominates. In Fig. 6.2c we show the corresponding (combined) fragment production rates for ABLA07 in the nuclear chart.

Some of the deficiencies beyond the second peak can also be attributed to the FRDM mass model, which is known to predict rather low or even negative neutron separation energies for nuclei beyond the $N = 82$ shell closure around $N = 90$ ($A \sim 138$) (e.g., Meyer et al. 1992; Chen et al. 1995; Arcones & Martínez-Pinedo 2011). As a consequence, material is piled up in and slightly above the second peak, while the mass region beyond $A = 140$ is underproduced. This effect might be reduced when applying the new FRDM version (Möller et al., 2012, 2016), see e.g., Kratz et al. (2014). Thus, in order to explore the full dependence on uncertainties due to the combination of mass models and fission fragment distributions, we also performed reference calculations, employing the ETFSI–Q mass model (Pearson et al., 1996) and the HFB–14 model (Goriely et al., 2008, 2009) for the set of fragment distributions Kodama & Takahashi (1975), Panov et al. (2008), and ABLA07 (Kelic et al., 2008). They show less or no underproduction for $A > 140$, even for the Panov et al. (2008) fragment distribution. The results are displayed in Fig. 6.3.

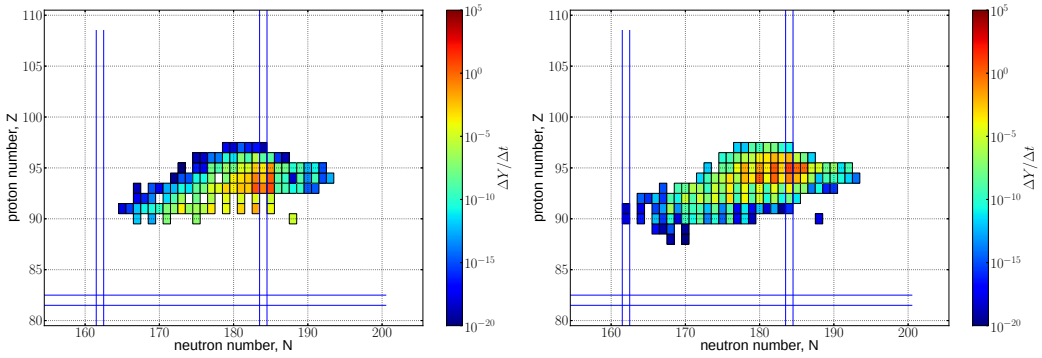

(a) β-delayed fission

(b) neutron-induced fission

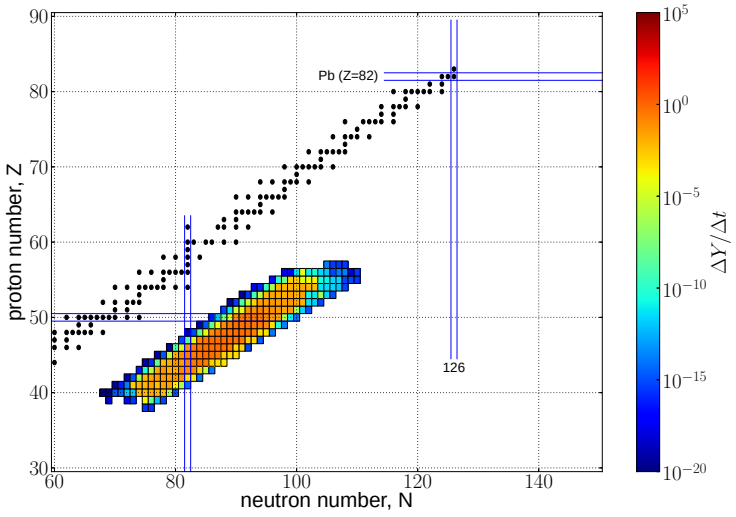

(c) fission fragments

Figure 6.2: Fission rates (at $t = 1$s) in s^{-1} for (a) β-delayed and (b) neutron-induced fission at freeze-out from (n,γ)–(γ,n) equilibrium for one representative trajectory when utilizing the FRDM mass model and Panov et al. (2010) fission rates. (c) Corresponding fission fragment production. The distribution model here is ABLA07.

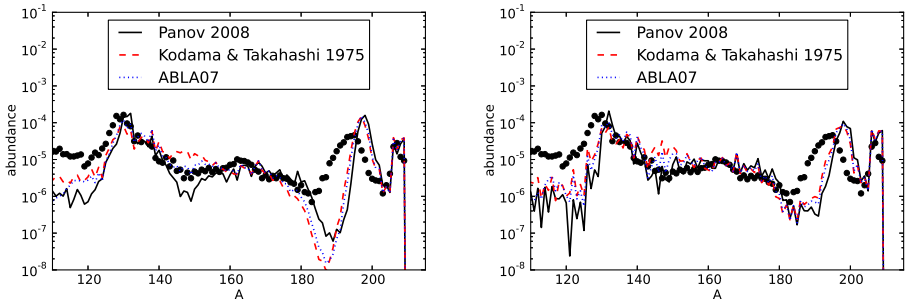

(a) ETFSI–Q (b) HFB–14

Figure 6.3: Similar to Fig. 6.1, several fission fragment distributions are tested for the mass models ETFSI–Q (Fig. 6.3a) and HFB–14 (Fig. 6.3b). It can be realized that in both cases the ABLA07 fragment distribution leads to a good fit to solar r-abundances in the mass region $A = 140 - 170$. In addition, these mass models also avoid the still (to some extent) existing underproduction due to FRDM, apparent in Fig. 6.1 also for the ABLA07 fragment distribution. The second peak in HFB–14 is slightly shifted to higher masses, a feature also seen in Bauswein et al. (2013). Whether this is due to different fission fragments or late neutron captures after fission will be discussed later.

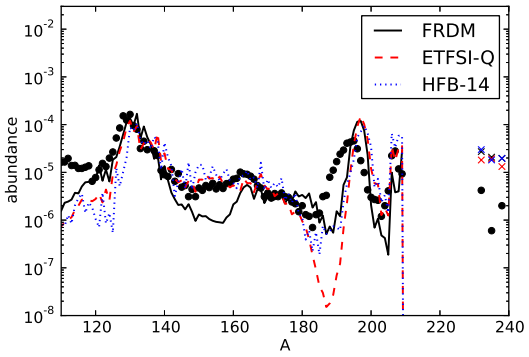

Figure 6.4: Comparison of nuclear mass models FRDM, ETFSI–Q, and HFB–14. The underproduction of $140 < A < 160$ nuclei apparent in the FRDM model does not occur in the ETFSI–Q or HFB–14 model cases. The fission fragment distribution model used here is ABLA07.

A comparison of all different mass models with the fragment distribution ABLA07 is shown in Fig. 6.4. ETFSI–Q suffers from a sudden drop of the neutron separation energy for $A \approx 140$, causing the formation of a small peak around this mass number. The distinctive trough in the ETFSI–Q abundance distribution before the third peak was subject of a detailed discussion in Arcones & Martínez-Pinedo (2011).

While the extent of the underproduction in the mass range 140 – 160 is due to a combination of the fission fragment distribution and the mass model used (see also Fig. 6.3), the results for all mass models utilized here show a shift of the third peak to higher mass numbers by up to 5 units, which will be a topic of the following sections.

While the position of the third peak is similar for all the mass models considered here, the abundance patterns around the second peak and the rare-earth peak show some diversity. For these mass regions, the final abundances are strongly influenced by fission close to the freeze-out and also possible final neutron captures thereafter. Therefore, different final abundance patterns can be an indicator of different fission progenitors. Figure 6.5 shows the predominant fission reactions at the time of freeze-out for the HFB–14 model. A comparison with Figure 6.2 reveals that for the HFB–14 model the fission close to freeze-out tends to happen at higher mass numbers (up to $A = 300$), while for the FRDM model the fission parent with the highest mass is found at $A = 287$. As a consequence, fragments with higher mass can be produced (Fig. 6.5c). However, the bulk of fragments lies between $A = 125$ and $A = 155$, very similar to the FRDM case. Therefore, the aforementioned shift of the second peak in the HFB model calculations cannot be due to the fission fragment distribution lacking fragments with mass numbers at the lower flank of the second peak. The main cause must be reactions occurring after fission, which will be discussed in the following section.

6.2.2 The Impact of Late Neutron Captures

In our NSM calculations, the third peak is shifted towards higher mass numbers compared to the solar values (Figures 6.1 , 6.3, & 6.4), regardless of the nuclear mass model utilized in the present investigation. This phenomenon has appeared in various calculations of NSMs before (Freiburghaus et al., 1999; Metzger et al., 2010b; Roberts et al., 2011; Korobkin et al., 2012; Goriely et al., 2013). We find that the position of the third peak in the final abundances is strongly dependent on the characteristics of the conditions encountered during/after the r-process freeze-out, which are characterized by a steep decline in neutron density and a fast increase in the timescales for neutron captures and photodissociations, leading to different stages (timescales): (1) freeze-out from an (n,γ)–(γ,n) equilibrium, (2) almost complete depletion of free neutrons ($Y_n / Y_{seed} \leq 1$), and (3) the final abundance distribution. In the following, we use the term *freeze-out* in the context of definition (1).

Figure 6.6 shows a comparison of our abundances on the r-process path resulting from detailed nucleosynthesis calculations at $t = 1$ s for the FRDM mass model with those which would result from an (n,γ)–(γ,n) equilibrium in each isotopic chain (as first discussed by Seeger et al. 1965) for the temperature and neutron

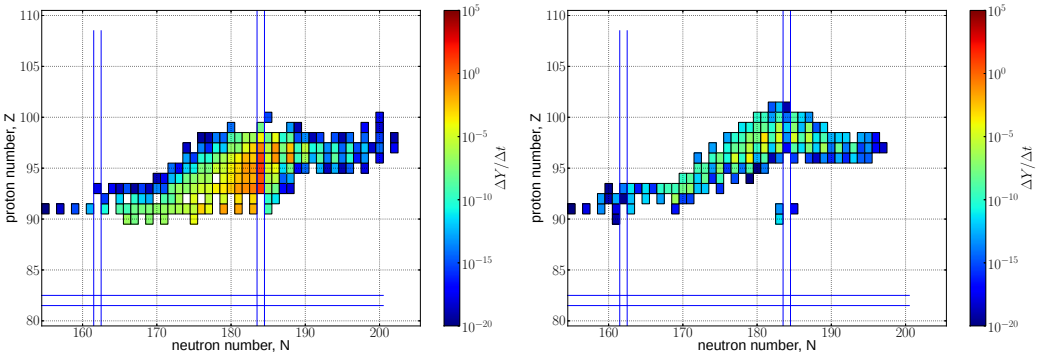

(a) β-delayed fission

(b) neutron-induced fission

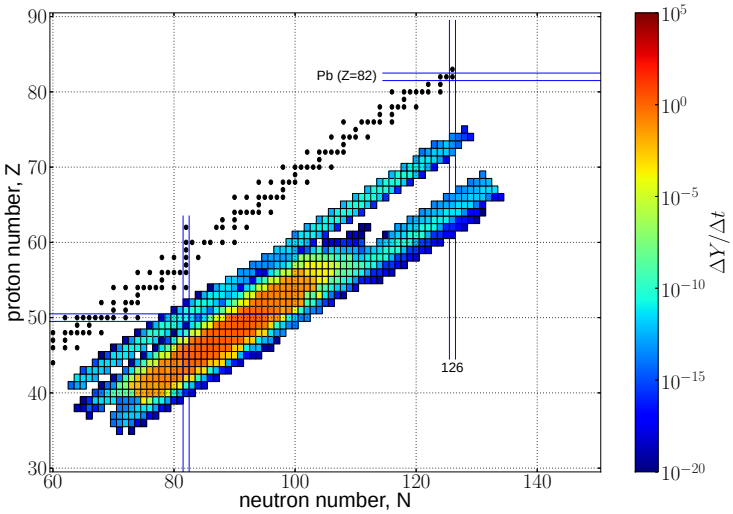

(c) fission fragments

Figure 6.5: Same as Fig. 6.2, but for the HFB–14 mass model.

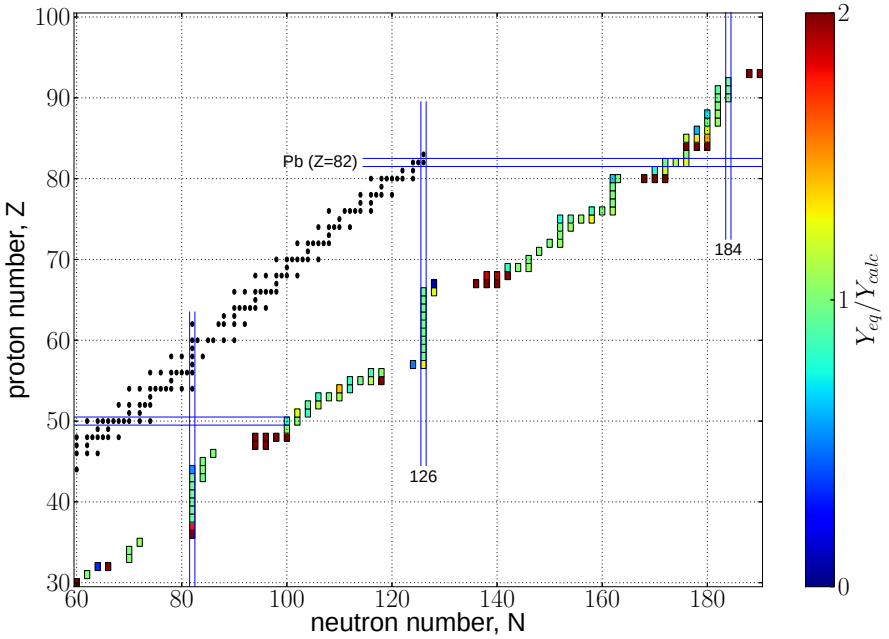

Figure 6.6: Comparison of abundances from our calculations with (n,γ)–(γ,n) equilibrium abundances on the r-process path for the FRDM mass model. The colours show the factor Y_{eq}/Y_{calc}. Only the most abundant nuclei are shown for each isotopic chain. See text for details.

density at that time ($T = 9.5\times10^8$ K, $n_n = 7.44\times10^{26}$ cm^{-3}). The plot displays the most abundant nuclei in each isotopic chain, i.e., those on the r-process path. The colours indicate the factor between the equilibrium abundances and the abundances in our calculation. The highest discrepancies can be observed around $N = 100$ and $N = 140$, but only few nuclei show a factor larger than 2. This leads to the conclusion that at this time the r-process still proceeds in (n,γ)–(γ,n) equilibrium with (n,γ) and (γ,n) timescales much shorter than β-decays, characteristic of a hot r-process.

This changes at $t = 1.34$ s (see Fig. 6.7), when the timescales for neutron capture and photodissociation become larger than the β-decay timescale. Here both reaction timescales become larger than β-decays, and also neutron capture wins against photodissociations. Note that the timescales of β-decay also become larger as the material moves closer to stability. As can be seen in Fig. 6.7, there is a short period after the freeze-out where (n,γ) dominates over both (γ,n) and β-decay. Figure 6.8 shows the second and third peak abundances at r-process freeze-out and the final abundances for a representative trajectory for the FRDM, ETFSI–Q, and HFB–14 mass models. It is evident that the position of the third peak is still in line with the

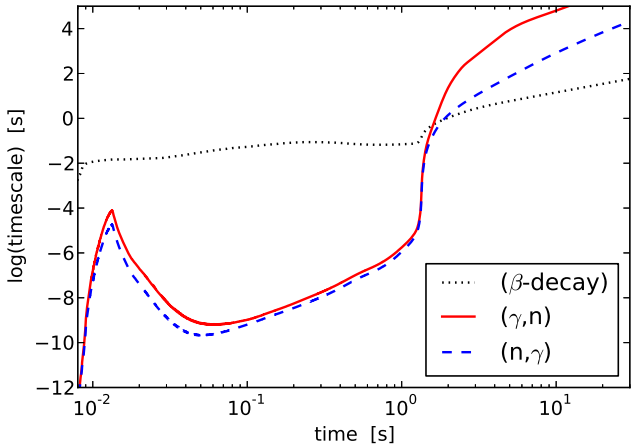

Figure 6.7: Averaged reaction timescales vs. time for β-decays, (γ,n) reactions, and (n,γ) reactions for one trajectory with the FRDM mass model.

solar peak at freeze-out, but is shifted thereafter for all mass models. The position of the second peak behaves differently. For all mass models, the final abundances for $A < 120$ nuclei are larger than the abundances at freeze-out, because fission fragments with these mass numbers are still produced after freeze-out. Nevertheless for the HFB–14 model the (final) second peak seems shifted to higher mass numbers, similar to its position at freeze-out. This might indicate that, for the astrophysical conditions encountered here, this mass model leads to a path running too close to stability. The shift in the third peak as described above is a generic feature in our NSM calculations. It is caused by the continuous supply of neutrons from the fissioning of material above $A \simeq 240$. Fig. 6.9 shows that after the freeze-out the release of neutrons from fission dominates over β-delayed neutrons.

To further illustrate the importance of fission neutrons after the freeze-out, we have run several calculations with both FRDM and HFB–14 where we have switched off certain types of reactions after the freeze-out. (1) The dashed lines in Figure 6.10 (labelled "only decays") represent the cases where only decay reactions are allowed after the (n,γ)–(γ,n) freeze-out (without fission). In this artificially created scenario the only possibility for nuclei after the freeze-out is to decay to stability, without the option to fission or capture neutrons. In fact, a small shift of the third peak to lower mass numbers can be observed during this phase (compare Fig. 6.10 & 6.8), as β-delayed neutrons cause the average mass number to decrease. In addition, since fission is not allowed either, the second peak consists of just the material that was present there at freeze-out, but the composition is (slightly) modified due to the combined effects of β-decays and β-delayed neutrons. (2) If we also allow for fission in addition to the decay reactions (dot-and-dashed lines in Fig. 6.10), the second peak is nicely reproduced by fission fragments for both mass models

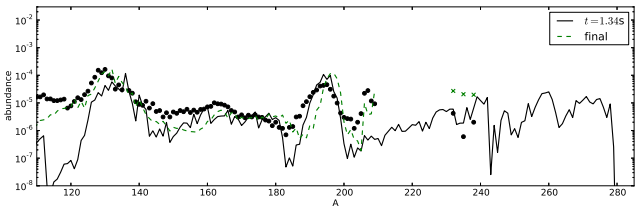

(a) FRDM

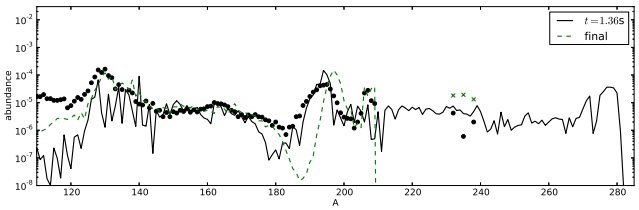

(b) ETFSI–Q

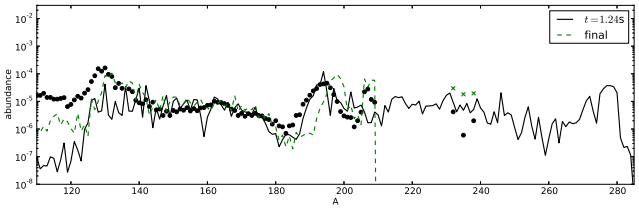

(c) HFB–14

Figure 6.8: (a) Second and third peak abundances at the time of r-process freeze-out (where $\tau_{(\gamma,n)} > \tau_{(n,\gamma)}$ or $t = 1.34$ s; solid line) compared to the final abundances (dashed line) for one trajectory employing the FRDM mass model. (b) Same for the ETFSI–Q mass model, where the freeze-out occurs at $t = 1.36$ s. (c) Same for the HFB–14 mass model. Here the freeze-out occurs at $t = 1.24$ s. Notice that the third peak position is still consistent with the solar r-abundances at freeze-out, but that for all mass models a shift takes place afterwards. For none of the mass models the features of the second peak at freeze-out are perfect. However, the FRDM and ETFSI–Q models show a decent agreement for the final abundances, while for the HFB–14 mass model the second peak is shifted for the time at freeze-out as well as for the final abundances.

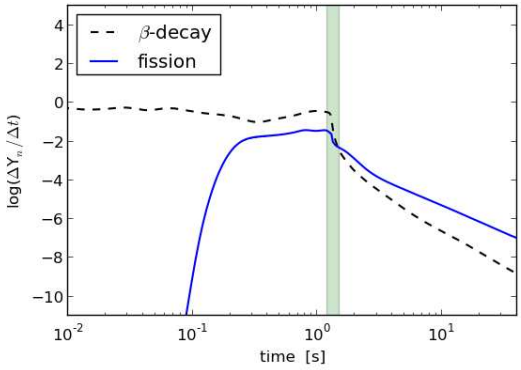

Figure 6.9: Released neutrons due to fission and β-delayed neutrons vs. time. The plotted quantity is the neutron production rate (per second). After the time of freeze-out (shaded area) fission neutrons dominate over β-delayed neutrons.

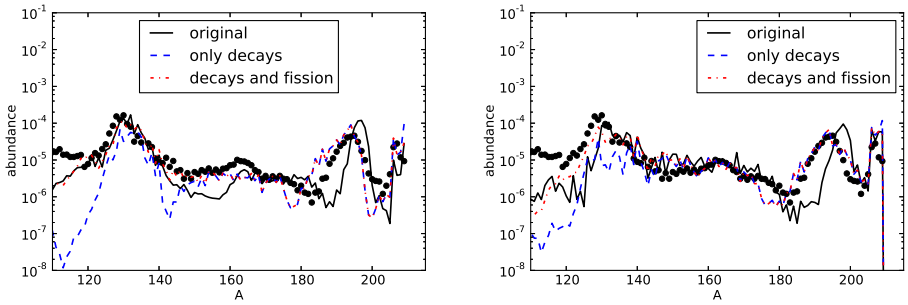

(a) FRDM (b) HFB–14

Figure 6.10: Final abundance distribution for cases where only certain types of reactions are allowed to proceed after freeze-out (dashed line: only decays except for fission; dot-and-dashed line: decays including fission) for (a) FRDM and (b) HFB–14. The solid line represents the original calculation where neutron captures are also allowed after freeze-out. All cases use ABLA07.

and the third peak is still not affected. (3) However, a notable difference between the two mass models can be seen for the final abundance distribution including also final neutron captures (denoted as "original" in Fig. 6.10), indicating that for HFB not only the position of the third peak is influenced by late neutron captures, but also the position of the second peak. On the other hand, the behaviour is reversed for the mass region $140 < A < 160$, where large deviations can be observed compared to the original calculation for FRDM, since in the original case neutron captures move material up to higher masses, creating the underproduction we have discussed in chapter 6.2.1. This indicates that when also neutron captures and all other reactions are permitted after freeze-out (i.e., the original calculation), major

changes in the abundance pattern can still occur. The third peak moves to higher masses for all mass models discussed here. In the HFB case, the second peak moves to the position it had at freeze-out, resembling abundance features resulting from an r-process path too close to stability for the astrophysical conditions encountered here.

It can be seen in Figures 6.1 , 6.3 & 6.8 that the shift of the third peak is indeed related to the amount of released neutrons. The shift is smallest for the Kodama & Takahashi (1975) model, which does not assume any neutron emission during fission, and largest for the Panov et al. (2008) model, which assumes the largest amount of neutrons produced. It should be noted, however, that the differences are smaller than expected from the numbers of released neutrons as in addition to the neutrons directly released during fission also those released from the neutron-rich fission fragments can be important as they move back to the r-process path. These in turn depend on the fission yields used. Since the position of the third peak does not coincide with the third peak of the solar abundance pattern, we explore in the following under which conditions such a shift to larger mass numbers can be avoided. In a first test we artificially increase the temperature throughout the expansion by setting the heating efficiency parameter $\epsilon_{th} = 0.9$ instead of our default value of 0.5 (see section 6.1). This change does not affect the final abundance distribution significantly, in particular the position of the third peak, because more vigorous heating simply prolongs the (n,γ)–(γ,n) equilibrium until the temperature drops to a similar value due to expansion. Therefore, the r-process freeze-out happens later, at a temperature that is comparable to the reference case ($\epsilon_{th} = 0.5$). Our finding that the exact value of the heating efficiency parameter ϵ_{th} does not greatly affect the final abundances, provided that it is above some threshold value, is in agreement with Korobkin et al. (2012).

We have further explored the effect of modified neutron capture rates. Slower rates could arise as the statistical model might not be applicable for small neutron separation energies S_n and not sufficiently high level densities in the compound nucleus. Faster rates could be attributed to the rising importance of direct capture contribution far from stability (Mathews et al., 1983; Rauscher, 2011). We realized that artificially varying the neutron capture rates across the nuclear chart does not have an effect on the position of the third peak. However, some minor local effects on the final abundance distribution can be observed. Reduced rates slow down the reaction flux and, as a consequence, lead to a reduced underproduction of $140 < A < 165$ and a slight overproduction of $180 < A < 190$ nuclei, the former due to fission fragments, the latter caused by S_n predictions of the FRDM mass model. Accelerating the rates has an opposite, but still minor effect.

As the shift is related to the continuous supply of neutrons from fission of heavy nuclei, any mechanism that affects the timescale for this supply can potentially influence the position of the third r-process peak. As an example, we have artifi-

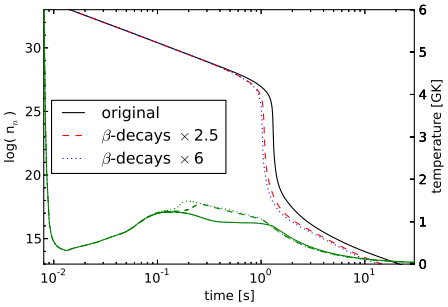

(a) FRDM neutron density and temperature

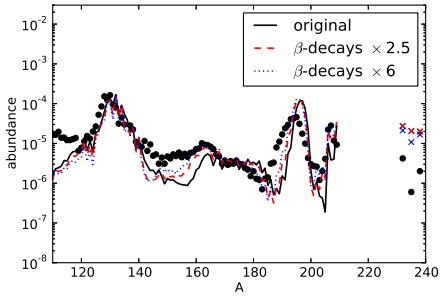

(b) FRDM final abundances

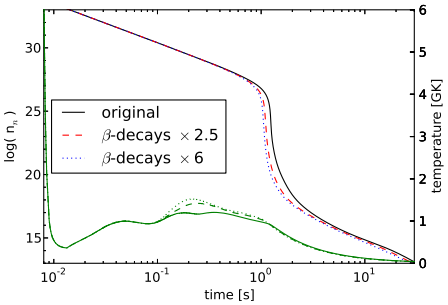

(c) HFB–14 neutron density and temperature

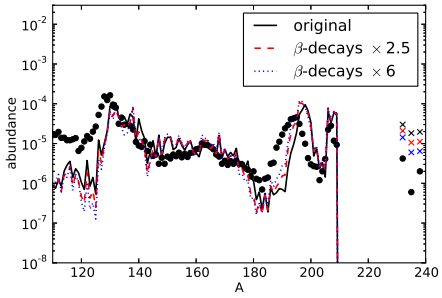

(d) HFB–14 final abundances

Figure 6.11: (a) Neutron density (n_n) and temperature (green lines in the bottom part of the graphs; the linestyles correspond to the individual calculations), and (b) final abundances for a NSM calculation with artificially acccelerated β-decays (dashed and dotted line) compared to the original calculation (solid line) with the FRDM nuclear mass model. The calculations were repeated using the HFB–14 model ((c) & (d)). The dots in (b) and (d) represent the solar r-process abundance pattern (Sneden et al., 2008). Here we use the ABLA07 fission fragment distribution model (Kelic et al., 2008). See text for further explanations.

cially increased all the β-decay rates for nuclei with $Z > 80$ (which corresponds roughly to $A > 220$) by exploratory factors of 2.5 and 6, respectively. This change of rates has been motivated by recent calculations (Panov et al., 2015; Marketin et al., 2015). These latest predictions underline that especially the heavy nuclei with $Z > 80$ may have shorter half-lives by a factor of up to 10 and more. This is exactly the mass range tested in the present calculations. The results are shown in Figure 6.11 for the example of one trajectory with two nuclear mass models (FRDM and HFB). As a consequence of the increased β-decay rates, the reaction flux for the heavy nuclei is accelerated, which increases both the heating rate and the temperature at around 0.1 s in the calculation (Figures 6.11a & 6.11c). Additionally, the release of neutrons by fission of heavy nuclei is accelerated, providing neutrons before freeze-out (when the third r-process peak is still located close to solar values). The evolution after freeze-out proceeds faster and consequently the period of time where a combination of neutron captures and β-decays can move nuclei to higher mass numbers becomes shorter. As a consequence, the shift in the third r-process peak is reduced.

We have also tested the effect of an overall increase of (experimentally unknown) β-decay rates by constant factors across the nuclear chart. In this case the effect discussed above vanishes again, as the matter flux feeding the abundance of fissioning nuclei continues on a faster pace and thus leads to an extended release of fission neutrons.

In summary, neutron capture after (n,γ)–(γ,n) freeze-out changes composition features which originate from classical r-process patterns related to an r-process path at a given neutron separation energy. This can be realized by combining the findings in Figures 6.8, 6.10, & 6.11, but is complicated by a complex interaction of freeze-out, final neutron captures, and the feeding due to fission (combined with neutron release). Fig. 6.8 demonstrates (for all mass models) that the third peak is shifted to higher masses during/after freeze-out, caused by the final neutron captures from neutrons which are released during fission of the heaviest nuclei in the final phases of nucleosynthesis (whereas the third peak is still located at the correct position in the last moments when (n,γ)–(γ,n) equilibrium holds). This feature is underlined by the results of Fig. 6.11, which show the effect of accelerating the beta-decays of the heaviest nuclei ($Z > 80$), i.e., accelerating the feeding of fission parents, which causes fission (and the related neutron release) to occur at different phases (before/during/after) of the freeze-out. An early neutron release (coming with the fastest β-decays of heavy nuclei) still tends to permit (n,γ)–(γ,n) equilibrium and reduces the effect of late neutron capture, although the effect is not sufficient to prevent the move of the third peak completely. We see a similar effect in the $A = 140 - 160$ mass region for the FRDM mass model, slowing down the movement of matter to heavier nuclei and partially avoiding the trough which appears in the final abundance pattern for the original calculation with unchanged nuclear input. A more complex behaviour causes the final abundance pattern of

the second r-process peak with a complex interaction of fission feeding and final neutron processing. In Fig. 6.10 we see that for the FRDM as well as the HFB mass model (when utilizing ABLA07) we have an almost perfect fragment distribution in order to reproduce the second r-process peak (see the entry "decays and fission" in Fig. 6.10 and Fig. 6.2c & 6.5c). However, the final ("original") distribution in the case of FRDM fits the second peak nicely, while for the HFB mass model the peak is shifted by several mass units. From Fig. 6.8 it becomes clear that (not the overall abundance shape, but) the peak positions are in both cases close to the average peak position at (n,γ)–(γ,n) freeze-out. This seems to indicate that even in these final phases an r-process path is again established which is closer to stability for the HFB than for the FRDM mass model, leading to a peak shifted to higher masses (for the conditions obtained in the dynamical ejecta of neutron star mergers). This effect can only be avoided either by a change of the nuclear mass model or by different environment conditions.

6.2.3 Testing the Global Fit via Variations in Mass Models and Beta-Decay Rates

Having shown the impact of a simple (and artificial) change in β-decay half-lives in the previous chapter, we now employ the newly calculated sets of half-lives of Panov et al. (2015) and Marketin et al. (2015). Both new sets predict shorter half-lives for the majority of neutron-rich nuclei in the nuclear chart compared to the previously used Möller et al. (2003) half-lives. However, there are some decisive differences. In Figure 6.12 we present a comparison of the new β-decay rates with the Möller et al. (2003) rates that we have used before. The Panov et al. (2015) set does not predict significantly faster rates far from stability, but in fact even noticeably slower rates (marked in blue) around $N = 162$ close to the neutron drip line. The faster rates (red) closer to stability only come into effect after freeze-out. The Marketin et al. (2015) calculations, on the other hand, predict faster rates for all nuclei on the r-process path beyond $N = 126$. The impact on the final abundances can be seen in Figure 6.13, where we present calculations performed using the Marketin et al. (2015) rates combined with both the FRDM and HFB–14 reaction sets as well as the Panov et al. (2015) rates together with the FRDM model. Note that the Marketin et al. (2015) rates have been calculated using a different mass model, so they are not fully consistent with neither FRDM nor HFB–14. The Panov et al. (2015) rates are based on FRDM, therefore we do not show a calculation with HFB–14.

The Marketin et al. (2015) rates show a similar effect on the final abundances as our artificial study in Fig. 6.11, broadening the low-mass flank of the third peak and increasing the abundances around the rare-earth peak. In fact, the broadening of the peak to lower mass numbers strongly improves the shape of the peak and (at least

for the HFB–14 mass model) even a shift of the position to lower masses can be observed. The Panov et al. (2015) rates have a different effect. Here the β-decays are faster for nuclei with $N = 126$ along the r-process path (before the freeze-out). Therefore the reaction flux proceeds faster in this region before it is held up afterwards at higher mass numbers, which means that less matter is accumulated in the peak. As a result, the height and shape of the third peak matches the solar peak very well (Fig. 6.13c). However, as the abundances of the nuclei in the peak are lower by roughly a factor of 2, each nucleus in the third peak can capture double the amount of neutrons and the effect of the third peak shift is increased. Furthermore, the Panov et al. (2015) rates show strong odd-even dependencies in the mass region $140 < A < 170$ (Fig. 6.12b), a quality which is reflected in the final abundances in this mass region.

6.3 Summary and Outlook

In this Chapter we have tested (for a given set of astrophysical conditions related to the dynamic ejecta of neutron star mergers) the effects of the complex interplay of the nuclear input, including mass models, fission and fission fragment distributions as well as beta-decay half-lives.

We have shown that the r-process yields are strongly affected by fission and the adopted model for fission fragment distributions. In general, we find that more sophisticated fission fragment distribution models (ABLA07) improve the overall agreement with the solar r-process abundances. Similar studies with different fission fragment distribution models have been performed recently (Goriely et al., 2013; Goriely, 2015a). Not surprisingly, the most significant variation is in the mass region $A = 100-160$, where the majority of the fission fragments is produced. This includes the second r-process peak and the rare-earth subpeak. Variations in nuclear mass models applied are decisive as well and we find that the combination of the applied mass model and the fission fragment distribution is essential for reproducing this mass region. In extreme cases of mass models which lead to fission only for $A > 300$ nuclei, the second r-process peak might not be produced at all (Shibagaki et al., 2015).

In neutron-rich NSM nucleosynthesis, the third peak in the final abundance distribution shifts towards higher masses, if after the (n,γ)–(γ,n) freeze-out the conditions for further neutron captures of neutrons released during fission prevail. If the neutron density is still sufficiently high, several neutron captures after freeze-out can shift the peak. It is possible that for mass models not utilized in this study, which have the third peak shifted to lower masses in (n,γ)–(γ,n) equilibrium (see e.g. Mendoza-Temis et al. 2015), the final neutron captures shift the peak to its correct position.

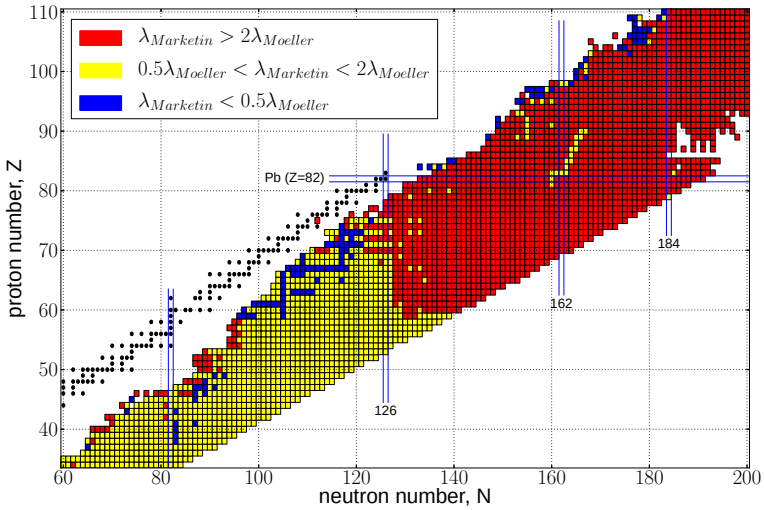

(a) Marketin (2015)

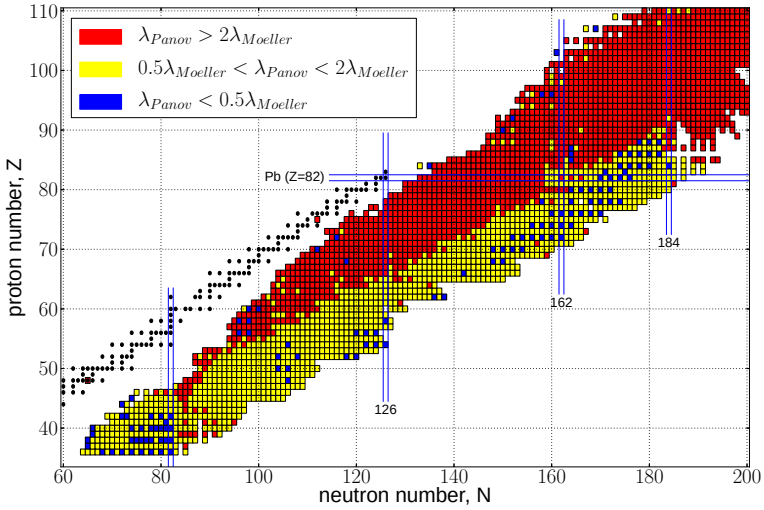

(b) Panov (2015)

Figure 6.12: (a) Comparison of the new Marketin et al. (2015) β-decay rates with the old Möller et al. (2003) rates. A red square means that the Marketin et al. (2015) β-decay rate ($\lambda_{Marketin}$) of the corresponding nucleus is more than two times faster than the Möller et al. (2003) rate, while a blue square signifies that the Marketin et al. (2015) rate is slower than the Möller et al. (2003) rate by more than a factor of 2. If the two rates are within a factor of 2 to each other, the square is coloured yellow. (b) Same for the new Panov et al. (2015) rates.

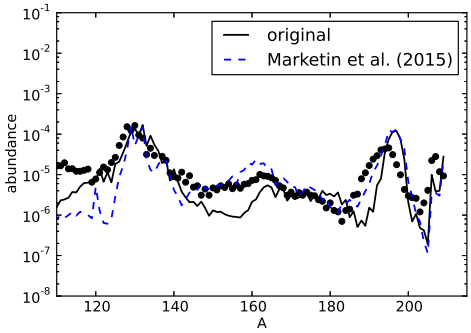

(a) FRDM, Marketin (2015)

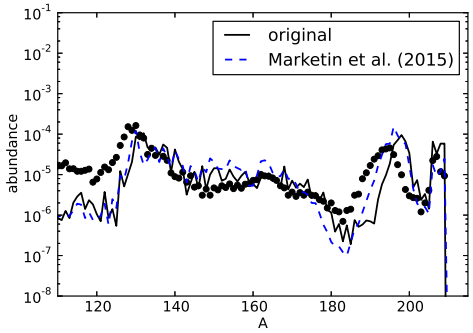

(b) HFB–14, Marketin (2015)

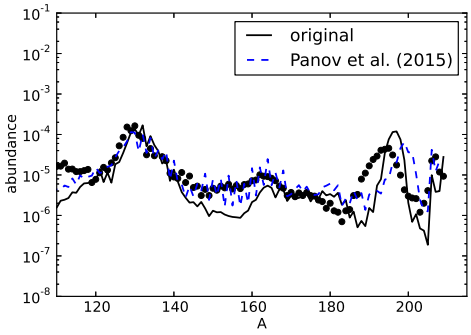

(c) FRDM, Panov (2015)

Figure 6.13: (a) Final abundance distribution for a calculation using the Marketin et al. (2015) rates together with the FRDM mass model and ABLA07. As a reference the FRDM, ABLA07 calculation from Fig. 6.1b is included. (b) Same, but using the HFB–14 mass model. (c) Same as (a), but with the Panov et al. (2015) rates.

We have also tested the effect of increased β-decay rates for the heaviest nuclei in our network ($Z \geq 80$), in which case the reaction flux is accelerated, leading to an earlier release of the fission (and β-delayed) neutrons which are recycled in the (n,γ)–(γ,n) equilibrium that is present before the freeze-out, and leaving less matter in the fissioning region during freeze-out. This effect was further tested for new sets of theoretical β-decay half-lives (Panov et al., 2015; Marketin et al., 2015), which can lead to very different results concerning the shape and position of the third peak. It should be noted that apparently the faster β-decay rates tested here can reduce the amount of late neutron captures and the shift of the third peak, but (at least in the present calculations) the shift of the third peak would not be prevented completely.

In summary, we explored the complex interplay of mass models, fission, and beta-decay half-lives for a variety of nuclear inputs and their impact on the resulting overall r-process abundances. Further changes can be expected with new versions of the FRDM model (Kratz et al., 2014; Möller et al., 2016) and many improved future nuclear structure predictions will be needed to settle these aspects completely.

Independent of the nuclear aspects/uncertainties studied here, it should also be realized that the astrophysical conditions matter as well. Here we utilized only the conditions for the dynamical ejecta of neutron star mergers within the treatment of Korobkin et al. (2012) or Bauswein et al. (2013). However, these dynamical ejecta can also be affected by neutrino interactions and NSM ejecta include, apart from the dynamical channel, also matter ejected via neutrino-driven winds (e.g., Dessart et al. 2009; Rosswog et al. 2014; Perego et al. 2014; Just et al. 2015) and matter from unbinding a substantial fraction of the late-time accretion disk (e.g., Metzger et al. 2008; Beloborodov 2008; Lee et al. 2009; Fernández & Metzger 2013a,b; Just et al. 2015). These additional channels yield larger electron fractions, since matter stays substantially longer near the hot central remnant and therefore positron captures and neutrino absorptions are likely. A number of recent studies (Just et al., 2015; Perego et al., 2014; Wanajo et al., 2014) find a broader range of Y_e-values that may be beneficial for the production of r-process elements and may also contain substantial "weak" r-process contributions (for a parametric study of possible neutrino and antineutrino luminosities and average energies see Goriely et al. 2015). These would be closer to conditions from investigations for matter ejected in the jets of magneto-rotationally powered core-collapse supernovae (see Winteler et al. 2012 and section 7.3), leading to less fission cycling and less final neutron captures from fission neutrons. Both aspects, improvements in the nuclear structure input as well as the complete description of the astrophysical conditions encountered in NS-NS and also NS-BH mergers should be followed in the future.

Chapter 7

Nucleosynthesis in Core-Collapse Supernovae

Core-collapse supernovae (CCSNe) mark the end of massive stars' ($M > 8\ M_{\odot}$) lives. A pre-supernova star is constantly held up against its own gravitational force by radiation pressure resulting from burning nuclear fuel into products with larger total binding energy. At the end of Si burning (the last burning stage), the core consists mainly of iron group nuclei. Since these nuclei have the largest binding energy per nucleon, no further energy can be generated via nuclear fusion. By the time most Si is consumed, the radiation pressure decreases and the core begins to contract, as there is nothing to oppose the gravitational force. Initially, the electron pressure slows down the contraction, but as the central density increases, so does the electron Fermi energy and electron captures on nuclei are accelerated, reducing the electron pressure and turning the core contraction into a collapse. Electron captures continue to occur until the density reaches $\rho \simeq 10^{12}$ gcm^{-3} (Bethe, 1990). At this point, neutrinos cannot escape freely anymore and scatter off nuclei and electrons via neutral-current interactions, which eventually leads to an equilibrium between neutrinos and matter. As the neutrinos scatter, they lose energy, facilitating their escape from the trapping region (because the mean-free path is inversely proportional to the square of their energy). However, between the trapping radius and the *neutrinosphere* radius (i.e., the radius from where the neutrinos will escape freely from the star), they have to cover a large distance where they can still scatter off matter. At the same time, the neutrino scattering leads to an increase in entropy. Eventually, the density in the core exceeds nuclear density, and the low-range repulsive component of the strong interaction becomes dominant, resulting in *core bounce* and an initial outward shock. As this prompt shock moves outwards, however, it quickly loses energy, since it dissolves the nuclei into nucleons and α-particles at a cost of 8.8 MeV per nucleon, and eventually stalls at a radius of a few hundred kilometres. The origin and nature of the mechanism that leads to a

successful explosion and ejection of material into the interstellar medium has still not been conclusively found, but the most promising approach involves a shock-revival by means of absorption of neutrinos (Colgate & White, 1966). During the collapse, an enormous amount of gravitational energy is released, leading to a very high temperature in the center. After core bounce, high-energy neutrinos are emitted, deleptonizing and cooling the core. Wilson (1985) found that at a distance $r = 100 - 200$ km to the center, these neutrinos can efficiently be absorbed, if the (predominant) ^{16}O nuclei are dissociated into nucleons beforehand. This would lead to additional heating in this region and a revival of the stalled shock, resulting in a successful supernova explosion. For a more detailed description of the supernova mechanics, see e.g., Bethe (1990).

In hydrodynamic simulations of CCSNe, special emphasis is laid on the treatment of neutrinos. Up to this day, however, only the lowest-mass progenitor models lead to an explosion. In addition, the consideration of general relativity and multi-D effects such as convection or turbulences can have a great impact on the evolution of the shock and the chemical composition of the ejecta.

Until recently, large studies of CCSNe comprising many different progenitor masses could only be performed in spherical symmetry due to computational power constraints. These studies do not only serve the purpose of investigating the explosion characteristics of the different progenitors, but also help understand the explosive nucleosynthesis of α-elements beyond Si and their distribution in the galaxy through space and time.

CCSNe appear much earlier in the galactic history than the other main contributors to explosive nucleosynthesis (i.e., Type I SNe and neutron star mergers). This means that metal-poor stars can give us valuable clues about the typical compositions of the ejecta in CCSNe. In addition, direct observations of type II supernova light curves are a very good indication of the amount of certain radioactive isotopes produced in such an event. In particular, from SN 1987A reliable numbers are available for the ejected masses of $^{56-58}$Ni and ^{44}Ti. The progenitor of SN 1987A was identified to be around 20 $M_\odot$ (Podsiadlowski et al., 2007).

In the past, many studies have been conducted to gain a better understanding of the nucleosynthesis associated with CCSNe and their role in enriching the interstellar medium with α-element and Fe group nuclei (e.g., Woosley & Weaver 1995; Thielemann et al. 1996). As CCSNe have been the first explosive events to occur in the young galaxy, the compositions of very metal-poor stars can be interpreted as the results of several nearby CCSNe, without any contributions from type I SNe or neutron star mergers.

A correlation between some supernova characteristics (such as the explosion energy or the amount of ejected nickel) and a progenitor-dependent property called

compactness parameter has been found in several recent studies (O'Connor & Ott, 2011; Ugliano et al., 2012; Nakamura et al., 2015; Perego et al., 2015). The compactness parameter is usually defined as the ratio of an arbitrarily chosen enclosed mass M and its corresponding radius inside the progenitor,

$$\xi_M = \frac{M/M_\odot}{R(M)/1000\ km}\,, \tag{7.0.1}$$

in line with the definition of O'Connor & Ott (2011), who introduced it first.

7.1 Reproducing SN 1987A Yields in Spherical Symmetry Using the PUSH Method

The PUSH method (Perego et al., 2015) is a new mechanism to explode supernovae in spherical symmetry that relies on an additional energy-deposition term. The basic idea is that a certain fraction of the heavy-flavour neutrinos (ν_μ, $\nu_{\bar{\mu}}$, ν_τ- and $\nu_{\bar{\tau}}$) is absorbed in the regions where neutrino-driven convection is possible and where the net energy gain from electron-neutrino interactions is positive. The local heating term $Q^+_{\rm push}(t,R)$ is given by

$$Q^+_{\rm push}(t,r) = 4\,\mathcal{G}(t)\int_0^\infty q^+_{\rm push}(r,E)\,dE\,, \tag{7.1.1}$$

where

$$q^+_{\rm push}(r,E) \equiv \sigma_0\,\frac{1}{4\,m_b}\left(\frac{E}{m_e c^2}\right)^2\frac{1}{4\pi r^2}\left(\frac{dL_{\nu_x}}{dE}\right)\mathcal{F}(r,E)\,. \tag{7.1.2}$$

Here, m_b is the average baryon mass and $(dL_{\nu_x}/dE)/(4\pi r^2)$ is the spectral energy flux for any single ν_x neutrino species with energy E. Since all four heavy neutrino species are treated equally, equation (7.1.1) contains a factor 4. The typical neutrino cross section σ_0 is given by

$$\sigma_0 = \frac{4G_F^2\left(m_e c^2\right)^2}{\pi\,(\hbar c)^4} \approx 1.759\times10^{-44}\mathrm{cm}^2\,, \tag{7.1.3}$$

with G_F being the Fermi coupling constant. The already mentioned criterion that determines where $Q^+_{\rm push}$ is active is represented by the term

$$\mathcal{F}(r,E) = \begin{cases} 0 & \text{if} \quad ds/dr > 0 \quad \text{or} \quad \dot{e}_{\nu_e,\bar{\nu}_e} < 0 \\ \exp(-\tau_{\nu_e}(r,E)) & \text{otherwise} \end{cases}\,. \tag{7.1.4}$$

This term is zero for all zones where neutrino-driven convection is ruled out ($ds/dr > 0$ with s being the matter entropy) or where the net specific energy gain rate due

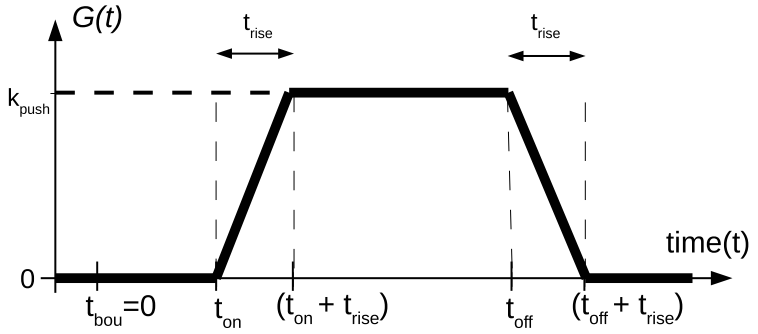

Figure 7.1: The function $\mathcal{G}(t)$ determines the temporal behaviour of the heating due to PUSH. The quantity $t_{\rm on}$ is robustly set by multi-dimensional models. We consider a value of 80 ms in our calculations and a value of 120 ms for testing. $t_{\rm rise}$ and $k_{\rm push}$ are set by our calibration procedure, spanning a range from 50 ms to 250 ms, and from 0 (PUSH off) to ~4, respectively. Since we assume that the explosion takes place within the first second after core bounce, we use $t_{\rm off} = 1$s.

to electron neutrinos and anti-electron neutrinos $\dot{e}_{\nu_e,\bar{\nu}_e}$ is negative, i.e., where the neutrinos do not heat the matter. For all other zones the factor takes the value $\exp(-\tau_{\nu_e}(r,E))$, where τ_{ν_e} is the radial optical depth of the electron neutrinos.

In addition, $Q^{+}_{\rm push}(t,R)$ is active only for a certain amount of time which can be controlled by means of a few parameters. The time-dependence is regulated by the factor $\mathcal{G}(t)$ in equation (7.1.1) which is defined as

$$\mathcal{G}(t) = k_{\rm push} \times \begin{cases} 0 & t \le t_{\rm on} \\ (t - t_{\rm on})\,/t_{\rm rise} & t_{\rm on} < t \le t_{\rm on} + t_{\rm rise} \\ 1 & t_{\rm on} + t_{\rm rise} < t \le t_{\rm off} \\ (t_{\rm off} + t_{\rm rise} - t)\,/t_{\rm rise} & t_{\rm off} < t \le t_{\rm off} + t_{\rm rise} \\ 0 & t > t_{\rm off} + t_{\rm rise} \end{cases} , \qquad (7.1.5)$$

where k_{push} is a measure of the maximum strength and $t_{\rm on}$, $t_{\rm rise}$, and $t_{\rm off}$ determine the time evolution of the heating term $Q^{+}_{\rm push}(t,R)$. The time-dependence of $\mathcal{G}(t)$ is illustrated in figure 7.1.

PUSH provides a new, physically motivated framework for CCSN studies in spherical symmetry, and enables more reliable predictions with respect to the explosion energy, the mass cut and, consequently, the composition of the ejecta than the previously used piston (e.g., Woosley & Weaver 1995; Limongi & Chieffi 2006; Chieffi & Limongi 2013) or thermal bomb methods (e.g., Thielemann et al. 1996; Umeda & Nomoto 2008). In a first step, the free parameters are calibrated on the observed properties of SN 1987A (such as explosion energy, $^{56-58}$Ni and ^{44}Ti yields) for a progenitor mass between the 18.0 and 21.0 $M_\odot$ range, in which the expected mass of the progenitor of SN 1987A lies. Figures and text from the sections 7.1.1 to

7.1.6 are from Perego et al. (2015), with the exception of Figure 7.5, which has been used in Eichler et al. (2015b).

7.1.1 Nucleosynthesis network

To predict the composition of the ejecta, we perform nucleosynthesis calculations using WINNET (Winteler et al., 2012). We include isotopes up to ^{211}Eu covering the neutron-deficient as well as the neutron-rich side of the valley of β-stability. The reaction rates are the same as in Winteler et al. (2012). They are based on experimentally known rates where available and theoretical predictions otherwise. The n-, p-, and alpha-captures are taken from Rauscher & Thielemann (2000), who used known nuclear masses where available and the *Finite Range Droplet Model* (Möller et al., 1995) for unstable nuclei far from stability. The β-decay rates are from the nuclear database *NuDat2*[1].

We divide the ejecta into different mass elements of 10^{-3} $M_\odot$ each and follow the trajectory of each individual mass element. As we are mainly interested in the amounts of ^{56}Ni, ^{57}Ni, ^{58}Ni, and ^{44}Ti, we only consider the 340 innermost mass elements above the mass cut, corresponding to a total mass of 0.34 $M_\odot$. The contribution of the outer mass elements to the production of those nuclei is negligible.

For $t < t_{\rm final}$ ($t_{\rm final}$ being the simulation time of PUSH), we use the temperature and density evolution from the hydrodynamical simulations as inputs for our network. For each mass element we start the nucleosynthesis post-processing when the temperature drops below 10 GK, using the NSE abundances (determined by the current electron fraction Y_e) as the initial composition. For mass elements that never reach 10 GK we start at the moment of bounce and use the abundances from the approximate α-network at this point as the initial composition. Note that for all tracers the further evolution of Y_e in the nucleosynthesis post-processing is determined inside the WINNET network.

At the end of the simulations, i.e., $t = t_{\rm final}$, the temperature and density of the inner zones are still sufficiently high for nuclear reactions to occur ($T \approx 1$ GK and $\rho \approx 2.5 \times 10^3$ g cm^{-3}). Therefore, we extrapolate the radius, density and temperature up to $t_{\rm end} = 100$ s assuming an expansion with constant velocity:

$$r(t) = r_{\rm final} + t v_{\rm final} \tag{7.1.6}$$

$$\rho(t) = \rho(t_{\rm final}) \left(\frac{r(t_{\rm final})}{r(t)} \right)^2 \tag{7.1.7}$$

$$T(t) = T[s_{\rm final}, \rho(t), Y_e(t)], \tag{7.1.8}$$

[1] http://www.nndc.bnl.gov/nudat2/

where r is the radial position, v the radial velocity, ρ the density, T the temperature, s the entropy per baryon, and Y_e the electron fraction of the mass zone. The temperature is calculated at each timestep using the equation of state of Timmes & Swesty (2000).

7.1.2 Observational constraints from SN 1987A

The analysis and the modelling of the observational properties of SN 1987A just after the luminosity peak have been the topics of a long series of works (e.g., Woosley, 1988; Arnett et al., 1989; Shigeyama & Nomoto, 1990; Kozma & Fransson, 1998a,b; Blinnikov et al., 2000; Fransson & Kozma, 2002; Utrobin & Chugai, 2005; Seitenzahl et al., 2014, and references therein). They provide observational estimates for the explosion energy, the progenitor mass, and the ejected masses of ^{56}Ni, ^{57}Ni, ^{58}Ni, and ^{44}Ti, all of which carry rather large uncertainties. In Table 7.1, the reference values used for the calibration of the PUSH method are summarized.

The zero-age main-sequence (ZAMS) progenitor mass is assumed to be between 18 $M_\odot$ and 21 $M_\odot$, corresponding to typical values reported in the literature for the SN 1987A progenitor, see, e.g., Woosley (1988); Shigeyama & Nomoto (1990). For the explosion energy we consider the estimate reported by Blinnikov et al. (2000), $E_{\rm expl} = (1.1 \pm 0.3) \times 10^{51}$ erg (for a detailed list of explosion energy estimates for SN 1987A, see for example Table 1 in Handy et al. 2014). This value was obtained assuming ~14.7 $M_\odot$ of ejecta and a hydrogen-rich envelope of ~10.3 $M_\odot$. The uncertainties in the progenitor properties and in the SN distance were taken into account in the error bar. The employed values of the total ejecta and of the hydrogen-rich envelope are compatible (within a 15% tolerance) with a significant fraction of our progenitor candidates, especially for $M_{\rm ZAMS} < 19.6\ M_\odot$. Explosion models with larger ejected mass (i.e., less compatible with our candidate sample) tend to have larger explosion energies (see, for example, Utrobin & Chugai 2005). Finally, we consider the element abundances for ^{56,57}Ni and ^{44}Ti provided by Seitenzahl et al. (2014), which were obtained from a least squares fit of the decay chains to the bolometric light curve. For ^{58}Ni we use the value provided by Fransson & Kozma (2002).

7.1.3 Fitting procedure

We calibrate the PUSH method by finding a combination of progenitor mass, k_{push}, and t_{rise} which provides the best fit to all the observational quantities of SN 1987A mentioned above. The weight given to each quantity is related to the uncertainty. For example, due to the large uncertainty in the ^{44}Ti mass, this does not provide a strong constraint on selecting the best fit.

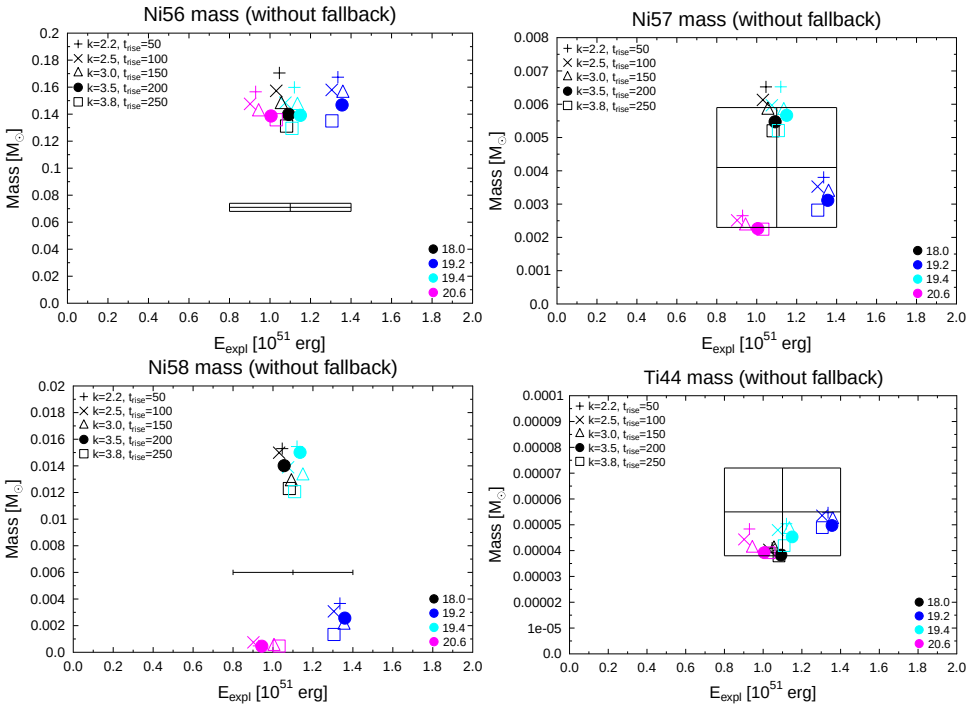

Figure 7.2: Ejected mass of ^{56}Ni (top left), ^{57}Ni (top right), ^{58}Ni (bottom left), and ^{44}Ti (bottom right) and explosion energy for four representative HC progenitor models. Five combinations of k_{push} and t_{rise} are shown, each with a different symbol. The error bar box represents the reported error range for ^{56,57}Ni and ^{44}Ti (Seitenzahl et al., 2014) and for the explosion energy (Blinnikov et al., 2000). No error bars are reported for ^{58}Ni.

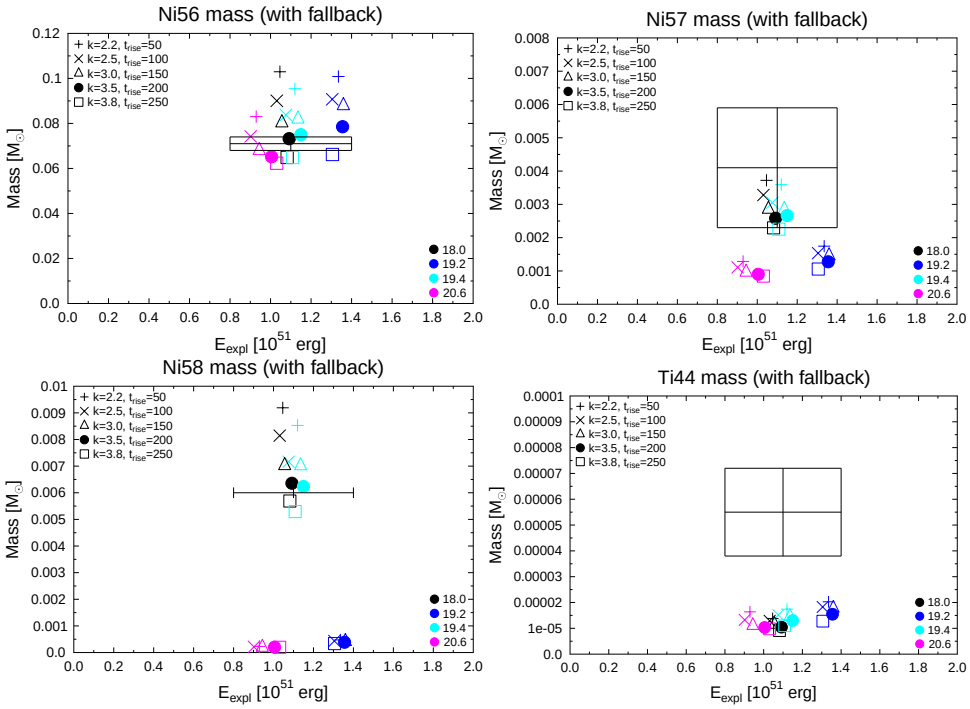

Figure 7.3: Same as Figure 7.2, but assuming 0.1 $M_\odot$ fallback. Note the different scale for ^{56}Ni and ^{58}Ni compared to Figure 7.2.

$E_{\rm expl}$	$(1.1 \pm 0.3) \times 10^{51}$ erg
$m_{\rm prog}$	18-21 $M_\odot$
$m(^{56}\mathrm{Ni})$	(0.071 ± 0.003) $M_\odot$
$m(^{57}\mathrm{Ni})$	(0.0041 ± 0.0018) $M_\odot$
$m(^{58}\mathrm{Ni})$	0.006 $M_\odot$
$m(^{44}\mathrm{Ti})$	$(0.55 \pm 0.17) \times 10^{-4}$ $M_\odot$

Table 7.1: The nucleosynthesis yields are taken from Seitenzahl et al. (2014) except for ^{58}Ni which is taken from Fransson & Kozma (2002). No error estimates were given for ^{58}Ni. The explosion energy is adapted from Blinnikov et al. (2000). For the progenitor range we chose typical values found in the literature, see e.g., Shigeyama & Nomoto (1990); Woosley (1988).

Figure 7.2 shows the explosion energy and ejected mass of ^{56}Ni, ^{57}Ni, ^{58}Ni, and ^{44}Ti for different cases of k_{push} and t_{rise}, and four selected high-compactness (HC) progenitors with relatively high explosion energies used to calibrate the PUSH method. The different cases of k_{push} and t_{rise} span a wide range of explosion energies around 1 Bethe. There is a roughly linear correlation between the explosion energy and the synthesized ^{56}Ni mass, which becomes more distinguished if more progenitor models are considered. However, this correlation is not directly compatible with the observations, as the ejected ^{56}Ni is systematically larger than expected (up to a factor of ~ 2 for models with an explosion energy around 1 Bethe). There is a weak trend that models with higher $t_{\rm rise}$ tend to give lower nickel masses for a given explosion energy.

Our simulations can be reconciled with the observations by taking into account fallback from the initially unbound matter. Since we do not model the explosion long enough to see the development of the reverse shock and the appearance of the related fallback when the shock reaches the hydrogen-rich envelope, we have to impose it, removing some matter from the innermost ejecta[2]. With a value of ~ 0.1 $M_\odot$ we can match both the expected explosion energy and the mass of ejected ^{56}Ni, see Figure 7.3. In this way we have fixed the final mass cut by observations. However, we point out that we are able to identify the amount of late-time fallback only because we also have the dynamical mass cut from our hydrodynamical simulations. This is not possible in other methods such as pistons or thermal bombs. Our value of 0.1 $M_\odot$ of fallback in SN 1987A will be further discussed and compared with other works in section 7.1.6.

[2]Note that we did not modify the explosion energy due to the fallback. This is based on the expectation that at the late time when fallback forms, the explosion energy is approximately equally distributed among the total ejected mass, which is about two orders of magnitude higher than our fallback mass.

k_{push} (-)	t_{rise} (ms)	$t_{\rm on}$ (ms)	$t_{\rm off}$ (s)
3.5	200	80	1

Table 7.2: The 18.0 $M_\odot$ progenitor, together with these parameters, gives the best fit to the observational data. In addition, we had to impose a late-time fallback of 0.1 $M_\odot$.

The observed yield of ^{56}Ni provides a strong constraint on which parameter combination would fit the data. From the observed yields of ^{57}Ni and ^{58}Ni, only the 18.0 and 19.4 progenitors remain viable candidates. Without fallback, our predicted ^{44}Ti yields are compatible with the observed yields (see Figure 7.2). However, if we include fallback (which is needed to explain the observed Ni yields), ^{44}Ti becomes underproduced compared to the observed value. Since this behaviour is true for all our models, we exclude the constraint given by ^{44}Ti from our calibration procedure. From the considered parameter combinations, we obtained the best fit to SN 1987A for the 18.0 $M_\odot$ progenitor model with $k_{\rm push} = 3.5$, $t_{\rm rise} = 200$ ms, and a fallback of 0.1 $M_\odot$. These parameters are summarized in Table 7.2.

A summary of the most important results of the simulations using this parameter set for the different progenitors in the 18-21 $M_\odot$ window is given in Table 7.3. For the remnant mass and for the ^{56}Ni yields of our best-fit model, we provide both the values obtained with and without assuming a fallback of 0.1 $M_\odot$.

7.1.4 Ni and Ti yields, progenitor dependence

Figures 7.2 and 7.3 show that the composition of the ejecta is highly dependent on the progenitor model, especially for the amount of ^{57}Ni and ^{58}Ni ejected. From the four HC progenitors shown, two (18.0 $M_\odot$ and 19.4 $M_\odot$) produce a fairly high amount of those isotopes, while the other two (19.2 $M_\odot$ and 20.6 $M_\odot$) do not reach the amount observed in SN 1987A. A thorough investigation of the composition profile of the ejecta reveals that ^{57}Ni and ^{58}Ni are mainly produced in the slightly neutron-rich layers ($Y_e < 0.5$), where the alpha-rich freeze-out leads to nuclei only one or two neutron units away from the $N = Z$ line. A comparison of the Y_e and composition profiles for the 18.0 $M_\odot$ and the 20.6 $M_\odot$ progenitors is shown in Figure 7.4. For the 18.0 $M_\odot$ model, the cutoff mass is 1.56 $M_\odot$ and a large part of the silicon shell is ejected. In this shell, the initial matter composition is slightly neutron-rich (due to small contributions from ^{54}Fe and ^{56}Fe), with $Y_e \simeq 0.498$ (dotted line in top left graph), and the conditions for the production of ^{57}Ni and ^{58}Ni are favourable. The increase in Y_e around 1.9 $M_\odot$ marks the transition to the

ZAMS ($M_\odot$)	$E_{\rm expl}$ (Bethe)	$t_{\rm expl}$ (s)	$M^B_{\rm remnant}$ ($M_\odot$)	$M^G_{\rm remnant}$ ($M_\odot$)	M(^{56}Ni) ($M_\odot$)
18.0	1.092	0.304	1.563	1.416	0.158
18.2	0.808	0.249	1.509	1.371	0.110
18.4	1.358	0.318	1.728	1.549	0.144
18.6	0.702	0.239	1.529	1.388	0.090
18.8	0.721	0.236	1.522	1.382	0.093
19.0	1.366	0.317	1.716	1.54	0.161
19.2	1.356	0.318	1.724	1.546	0.152
19.4	1.15	0.326	1.608	1.452	0.158
19.6	0.371	0.230	1.584	1.433	0.04
19.8	0.661	0.225	1.523	1.383	0.088
20.0	0.613	0.222	1.474	1.342	0.085
20.2	0.379	0.224	1.554	1.408	0.039
20.4	0.743	0.263	1.674	1.506	0.094
20.6	1.005	0.277	1.781	1.592	0.141
20.8	0.959	0.277	1.764	1.578	0.135
21.0	1.457	0.316	1.733	1.554	0.198
18.0 (fb)	1.092	0.304	1.663	1.497	0.082

Table 7.3: For the model 18.0 (fb), which is our best fit to SN 1987A, we have included 0.1 $M_\odot$ of fallback, determined from observational constraints. See the text for more details. The two different remnant masses given refer to the baryonic mass (M^B) and the gravitational mass (M^G), respectively.

oxygen shell. The same transition for the 20.6 $M_\odot$ model happens around 1.74 $M_\odot$, i.e., inside the mass cut. Therefore, this model ejects less ^{57}Ni and ^{58}Ni (see also Thielemann et al. 1990). In all our models, ^{44}Ti is produced within the innermost 0.15 $M_\odot$ of the ejecta (see Figure 7.4). Since we assume 0.1 $M_\odot$ fallback onto the proto-neutron star (PNS), most of the synthesized ^{44}Ti is not ejected in our simulations.

7.1.5 Sensitivities of nucleosynthesis yields

While post-processing the ejecta trajectories for nucleosynthesis, Y_e is evolved by the nuclear network independently of the hydrodynamical evolution. This leads to a discrepancy at later times between the electron fraction in the initial trajectory ($Y_e^{\rm hydro}$) and in the network ($Y_e^{\rm nuc}$). In order to estimate the possible error in our nucleosynthesis calculations arising from this discrepancy, we have performed reference calculations using $Y_e^{\rm hydro}(t = t_{\rm final})$ instead of $Y_e^{\rm hydro}(T = 10$ GK) as a

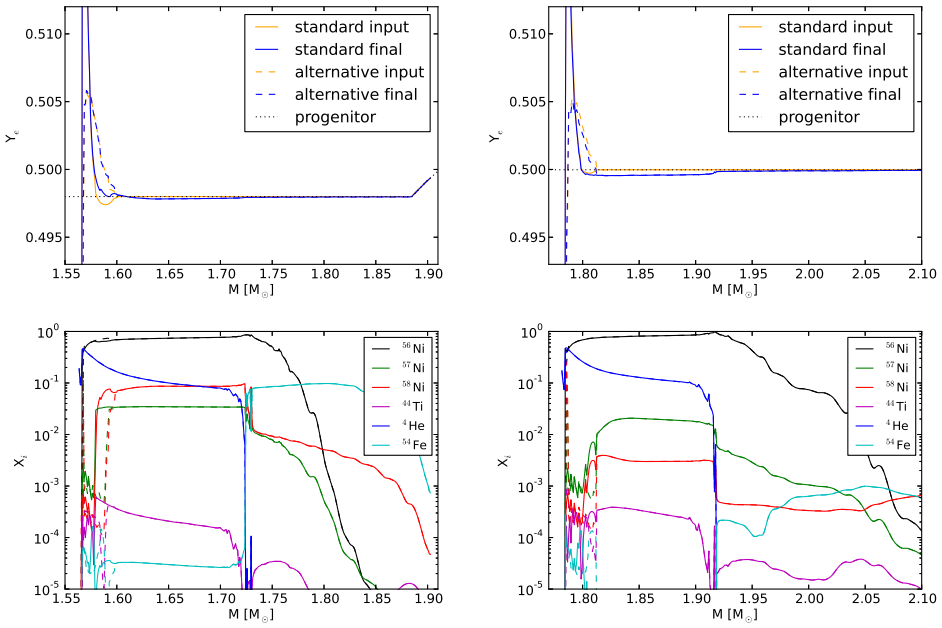

Figure 7.4: Electron fraction profiles (top) and nuclear compositions (bottom) above the mass cut for the 18.0 $M_\odot$ (left) and the 20.6 $M_\odot$ (right) progenitors with the parameters $k_{\rm push} = 3.5$ and $t_{\rm rise} = 200$ ms. The electron fraction is plotted for two different times in the network: the input values for the first timestep ("input") and the value after post-processing ("final"). The dashed lines correspond to the alternative case, where $Y_e^{\rm hydro}(t = 4.6\ {\rm s})$ is taken as the initial electron fraction in the network.

starting value for the network (see section 7.1.1). The results are shown in Figure 7.4 for two progenitors: 18.0 $M_\odot$ and 20.6 $M_\odot$. The label "standard" refers to the regular case which uses $Y_e^{\rm hydro}(T = 10\ {\rm GK})$ as input. The calculation using $Y_e^{\rm hydro}(t = t_{\rm final})$ as input is labelled "alternative" and is represented by the dashed lines. The point in time at which the Y_e profile is shown is indicated by the supplements "input" (before the first timestep) and "final" (at $t = 100$ s). For the Y_e profile of the 18.0 $M_\odot$ progenitor (top left) the minimum around 1.59 $M_\odot$ disappears, leading to an increase in ^{56}Ni in this region at the cost of ^{57}Ni and ^{58}Ni (bottom left). For the 20.6 $M_\odot$ progenitor the situation is similar, with only a very small region just above 1.8 $M_\odot$ showing significant differences. In general, we observe that the uncertainties in Y_e in our calculations are only present up to 0.05 $M_\odot$ above the mass cut. The resulting uncertainties in the composition of the ejecta are very small or even inexistent in the scenarios where we consider fallback.

The radioactive isotope ^{44}Ti can be detected in supernovae and supernova remnants. Several groups have used different techniques to estimate the ^{44}Ti yield (Chugai et al., 1997; Fransson & Kozma, 2002; Jerkstrand et al., 2011; Larsson

et al., 2011; Grebenev et al., 2012; Grefenstette et al., 2014; Seitenzahl et al., 2014), and the inferred values span a broad range, $(0.5 - 4) \times 10^{-4}$ $M_\odot$. Traditional supernova nucleosynthesis calculations (e.g., Thielemann et al., 1996; Woosley & Weaver, 1995) typically predict too low ^{44}Ti yields and there are only very few models that predict high yields: Thielemann et al. (1990) report ^{44}Ti yields around 10^{-4} and above in the best fits of their artificial SN explosions to SN 1987A. Rauscher et al. (2002) argue that the yields of ^{56}Ni and ^{44}Ti are very sensitive to the "final mass cut" (as we have shown, too), which is often determined by fallback.

Ejecta in a supernova may be subject to convective overturn. To account for this, we can assume homogeneous mixing in the inner layers up to the outer boundary of the silicon shell before cutting off the fallback material (see, for example, Umeda & Nomoto 2002 and references therein). For our best-fit model, the ejected ^{44}Ti mass increases to 2.70×10^{-5} $M_\odot$, if this prescription is applied. Comparing to the previous yield of 1.04×10^{-5} $M_\odot$, we observe that the effect of homogeneous mixing is considerable, but not sufficient to match the observational values. The ejected $^{56-58}$Ni masses also show a slight increase. However, there are also uncertainties in the nuclear physics connected to the production and destruction of ^{44}Ti. The final amount of produced ^{44}Ti depends mainly on two reactions: $^{40}\mathrm{Ca}(\alpha,\gamma)^{44}\mathrm{Ti}$ and $^{44}\mathrm{Ti}(\alpha,p)^{47}\mathrm{V}$. Margerin et al. (2014) measured the $^{44}\mathrm{Ti}(\alpha,p)^{47}\mathrm{V}$ reaction rate within the Gamow window and concluded that it may be considerably smaller than previous theoretical predictions. In their study, an upper limit cross section is reported that is by a factor of 2.2 smaller than the cross section we have used in our calculations (at a confidence level of 68%). Using this smaller cross section for the $^{44}\mathrm{Ti}(\alpha,p)^{47}\mathrm{V}$ reaction, our yield of ejected ^{44}Ti for our best-fit model (18.0 $M_\odot$ progenitor, $k_{\mathrm{push}} = 3.5$, $t_{\mathrm{rise}} = 200$ ms) rises to 1.49×10^{-5} $M_\odot$ with fallback, and 5.65×10^{-5} $M_\odot$ without fallback. This corresponds to a relative increase of 43% with fallback and 48% without fallback. If we include both the new cross section and homogeneous mixing, the amount of ^{44}Ti in the ejecta is 3.99×10^{-5} $M_\odot$, including fallback. This value, however, is still below the expected value derived from observations, but within the error box. The effects of the smaller destruction rate and homogeneous mixing are illustrated in Figure 7.5, where the black solid line is the standard calculation (corresponding to the ^{44}Ti line in Figure 7.4) and the ^{44}Ti yields with the modified $^{44}\mathrm{Ti}(\alpha,p)^{47}\mathrm{V}$ rate are represented by the black dashed line. The red horizontal line shows the average ^{44}Ti yield at each mass coordinate if, in addition to the modified rate, homogeneous mixing is assumed. The vertical dashed line indicates the mass cut with 0.1 $M_\odot$ fallback, i.e., the border between fallback and ejected material.

7.1.6 Amount of fallback

To reconcile our models with the nucleosynthesis observables of SN 1987A we need to invoke 0.1 $M_\odot$ of fallback (see section 7.1.3). The variation in the amount of synthesized Ni isotopes between runs obtained with different PUSH parameters (Figure 7.2) suggests that a smaller $t_{\rm rise}$ (and, consequently, smaller $k_{\rm push}$) could also be compatible with SN 1987A observables, if a larger fallback is assumed. On the one hand, assuming that $t_{\rm rise}$ ranges between 50 ms and 250 ms, fallback for the 18.0 $M_\odot$ model compatible with observations is between 0.14 $M_\odot$ (for $t_{\rm rise}$ = 50 ms) and 0.09 $M_\odot$ (for $t_{\rm rise}$ = 250 ms). On the other hand, if the amount of fallback has been fixed, the observed yields (especially of ^{56}Ni) reduce the uncertainty in $t_{\rm rise}$ to $\lesssim$ 50 ms.

Our choice of 0.1 $M_\odot$ is compatible with the fallback obtained by Ugliano et al. (2012) in exploding spherically symmetric models for progenitor stars in the same ZAMS mass window. Moreover, Chevalier (1989) estimated a total fallback around 0.1 $M_\odot$ for SN 1987A, which is supposed to be an unusually high value compared to "normal" type II supernovae. Recent multidimensional numerical simulations by Bernal et al. (2013); Fraija et al. (2014) confirmed this scenario and furthermore showed that such a hypercritical accretion can lead to a submergence of the magnetic field, giving a natural explanation why the neutron star (possibly) born in SN 1987A has not been found yet.

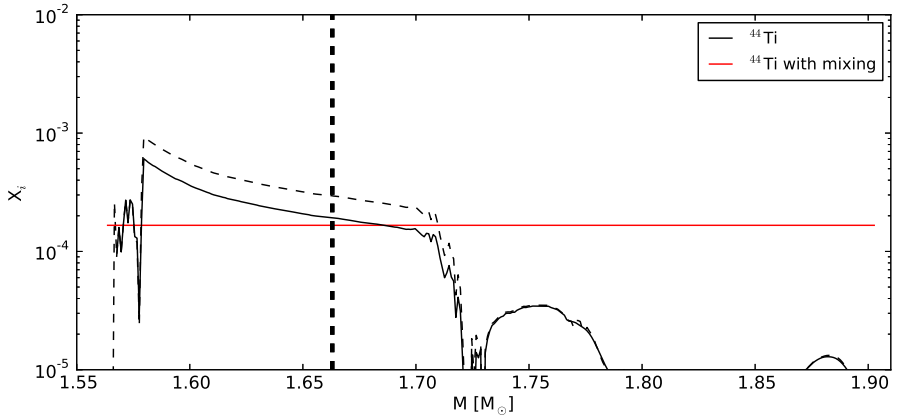

Figure 7.5: Standard (solid black line) and alternate ^{44}Ti yields for the 18.0 $M_\odot$ best-fit model: modified ^{44}Ti$(\alpha, p)^{47}$V rate without (black dashed line) and with homogeneous mixing assumed (red horizontal line). The vertical dashed line marks the final mass cut, if a fallback of 0.1 $M_\odot$ is applied. Figure adapted from Eichler et al. (2015b).

7.2 Multi-D Simulations and Their Nucleosynthesis Yields

In this section, we present detailed full-network nucleosynthesis calculations for an axisymmetric long-term CCSN simulation presented in Nakamura et al. (2015), using a 17 $M_\odot$ progenitor with solar metallicity from the Woosley et al. (2002) series. This progenitor has a compactness of $\xi_{2.5} = 0.161$, and is therefore an intermediate-compactness progenitor. The detailed explosion properties obtained in a long-term simulation are discussed in Nakamura et al. (2017), where a gravitational NS mass of 1.85 $M_\odot$ and a diagnostic explosion energy of 1.23×10^{51} erg are reported. The computational domain encompasses a mass of 4.07 $M_\odot$ and the simulation stops 7s after core bounce. For the nucleosynthesis calculations, we have used 129024 tracer particles that are initially evenly distributed in the computational domain.

7.2.1 Criteria for ejected particles

In a first step, it is important to know which particles are successfully ejected, i.e., become gravitationally unbound in the course of a SN. Usually, a particle is considered ejected when its specific total energy at the end of the simulation is positive ($E(7\text{s}) > 0$). The specific total energy is the sum of internal energy, (radial) kinetic energy, and gravitational potential ϕ:

$$E_{\text{tot}} = E_{\text{int}} + \frac{v_{\text{rad}}^2}{2} + \phi\,. \tag{7.2.1}$$

The initial and final positions (at $t = 0$s and $t = 7$s, respectively) of all tracer particles that are ejected according to this criterion are shown in Figure 7.6, along with the peak temperature each tracer reaches at any point in the simulation. Note that for this model the core bounce occurs at $t = 0.206$s. The progression and position of the shock front at the end of the simulation can be seen in the left panel, since all particles that encounter the shock at one point in the simulation have a higher peak temperature than the others. Indeed, the final velocities of the particles confirm that the shock proceeds in the polar directions, while material around the equator is infalling. The fate of the infalling material is uncertain at this point, as it could be both accreted onto the PNS or accelerated along the z-axis and ejected. Therefore, the pure energy criterion should be seen as an upper limit for the total ejecta mass.

We can find a lower limit by imposing an additional condition, when only particles with a positive radial velocity component are considered ejected, i.e., $E(7\text{s}) > 0$ & $v_{\text{rad}}(7\text{s}) > 0$. Figure 7.7 shows the initial and final positions of these tracers. The tracers in the blank areas around the equator are initially hit by a weak outward shock, obtaining a slightly positive radial velocity, which is however below the

escape velocity. Therefore, their flight from the PNS is stopped after a short amount of time and they fall back towards the center.

The role as lower limit of this criterion can be understood when considering the tracer particles close to the z-axis and still outside of the shock on the left-hand panel in Figure 7.6. Since these particles have not yet encountered the shock, they are infalling (and therefore do not count towards the final ejecta). As soon as the shock front reaches them, however, they will be turned around and their velocity

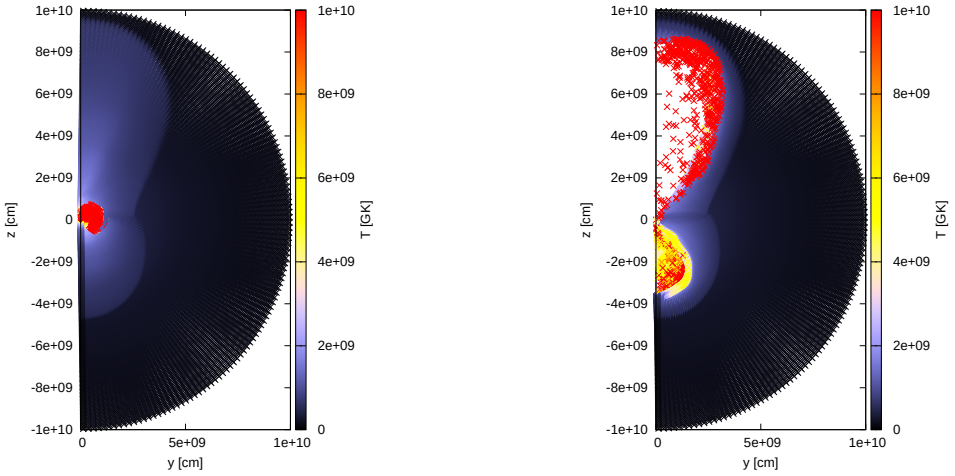

Figure 7.6: Initial distribution of tracer particles (left) with $E(7\text{s}) > 0$ and the final positions of the same tracers at a simulation time of 7s (right). The colour indicates the peak temperature that is reached during any time of the simulation.

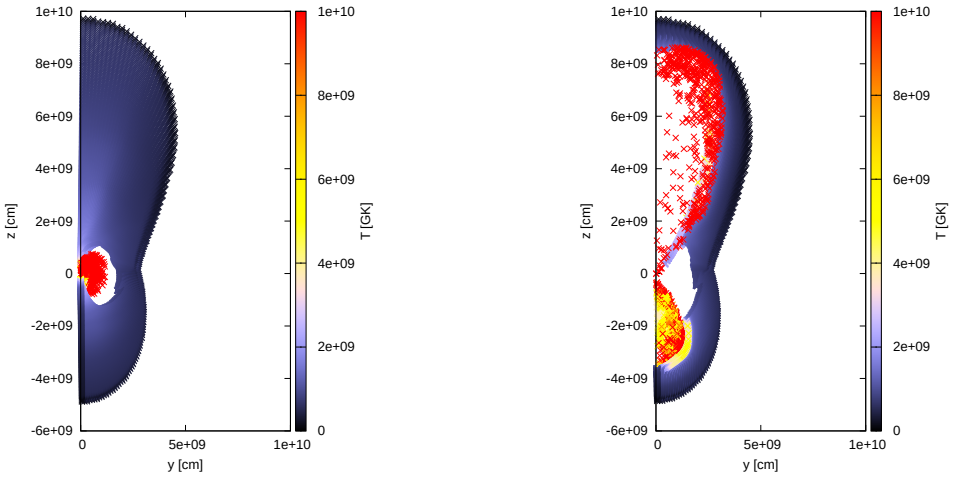

Figure 7.7: Same as Figure 7.6, but with the additional condition $v_{\text{rad}} > 0$ for successfully ejected particles.

vector will point outward. The total mass of ejecta according to the E & $v_{\rm rad}$ criterion is therefore sensitive to the simulation time at which the criterion is applied. Ideally, it would be applied at a time when the shock front has reached the outer layers of the star. This is not possible in this case, because the simulation stops before that point.

Out of the 4.07 $M_\odot$ in the computational domain, 1.93 $M_\odot$ are ejected according to the pure E criterion and 0.91 $M_\odot$ for the E & $v_{\rm rad}$ criterion. We have argued that both criteria do not give a good estimate of the ejecta mass, but should rather be considered an upper and lower limit, respectively. In order to obtain a better idea of the amount (and the composition) of the ejecta, we have tested other criteria. One of them is the condition $\rho(7\text{s}) < 10^{11}$ gcm^{-3}, henceforth labelled "ρ". Clearly, this prescription suffers from the same flaw as the pure E criterion, since all the particles outside the PNS count towards the final ejecta. Another option is to use a purely geometrical approach: We have already found that the shock propagates mainly in a bipolar fashion along the z-axis (see Figure 7.6), while matter around the equator is mostly infalling. Therefore, we can choose an angle θ above and below the equator that distinguishes between ejected and accreted material. Obviously, in order to avoid counting PNS material, we also ask for the ρ criterion to be fulfilled. The concept is illustrated in Figure 7.8 for $\theta = 30°$ (left) and $\theta = 45°$ (right).

We have already established that the ejecta mass is sensitive to the moment when the criteria are applied. The simulation stops at 7s and it can be expected that the most precise results are obtained when the criteria are applied at this moment. However, particles might not fulfil an ejection criterion when the simulation stops, but only later on, for instance when they encounter the shock front and are accelerated away from the center. Thus, we also apply all our criteria at a simulation time of $t = 5$s. By doing this, we are able to identify trends for the behaviour of the ejecta mass and the individual isotopic yields according to all our criteria. The total mass of the ejecta ($M_{\rm ejc}$) as well as the ejected masses of some isotopes are summarized in Table 7.4 for the pure energy (E), the energy with radial velocity ($E + v_{\rm rad}$), the density (ρ), and the two angle criteria (θ^{30} & θ^{45}) taken at 5s and 7s (indicated by the supplements "5" and "7"). The method for the nucleosynthesis calculations with which these yields were obtained is explained in section 7.2.2.

Table 7.4 reveals that the different ejection criteria give very different predictions for the total mass of the ejecta and the yields for ^{16}O and ^{28}Si. However, the values for M(^{44}Ti) and M(^{56}Ni) are very similar for all the criteria when applied at 7s. The predictions for the ejected ^{44}Ti mass lie within a range of 1.14×10^{-5} $M_\odot$ and 1.35×10^{-5} $M_\odot$, the predicted ^{56}Ni mass is between 1.10×10^{-2} $M_\odot$ and 1.39×10^{-2} $M_\odot$. The convergence of the yields for nuclei with higher mass numbers becomes even clearer in Figure 7.9, where the data from Table 7.4 are plotted in dependence of the moment of application.

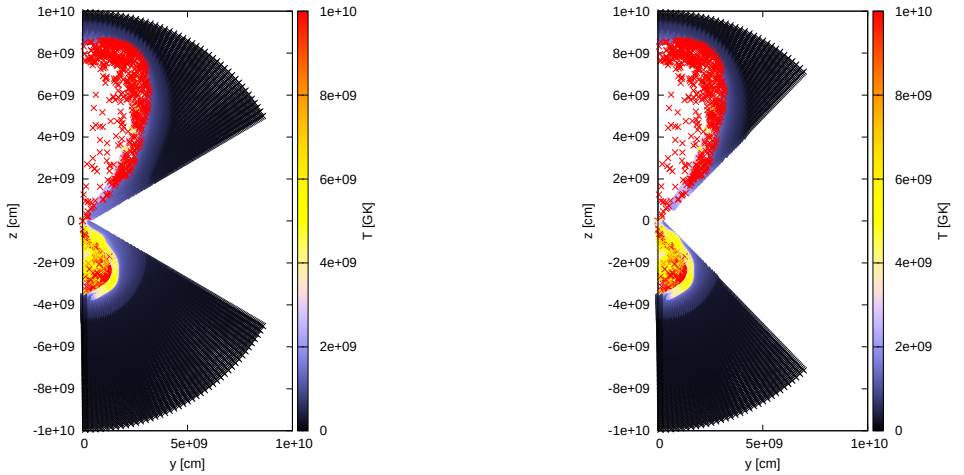

Figure 7.8: Left: Final positions of successfully ejected particles under the assumption that all particles within an angle $\theta = 30°$ above and below the equator are accreted onto the PNS, and all other particles with $\rho < 10^{11}$ gcm^{-3} are ejected. Right: Same, but with $\theta = 45°$.

Several trends are visible in Figure 7.9. First, the predicted total mass of the ejecta slowly decreases with increasing simulation time for four of the five criteria (top left panel). This can be explained by accretion onto the PNS, i.e., accreting particles become gravitationally bound (hence not fulfilling the pure E criterion anymore) and their density increases above 10^{11} gcm^{-3} (failing the ρ criterion). The decreasing trend for the θ criteria is due to particles that are first accelerated by the shock close to the boundary and after a while fall into the equatorial plane, thus not counting towards the ejecta anymore. For the $E + v_{\mathrm{rad}}$ criterion the ejected mass is growing, since the shock is still moving outward and accelerating infalling particles. Furthermore, there is a striking difference between the temporal behaviour of the ^{16}O and ^{28}Si yields on the one hand (Fig. 7.9b & 7.9c) and the ^{44}Ti, ^{56}Ni, and ^{68}Ge yields on the other hand (Fig. 7.9d–7.9f): The former group includes nuclei that are already present in the pre-SN progenitor (mainly in the outer layers), which means that their yields generally follow the trends of the total mass. ^{28}Si shows a slightly deviating behaviour from the total mass, because it is also the fuel for explosive Si burning in high enough temperatures (according to Thielemann et al. 1996, complete Si exhaustion is reached in tracers that reach $T = 5$ GK). The latter nuclei belong to the group of freshly synthesized products of the SN with relatively high mass number. They are localized mainly in the regions with the highest peak temperatures, and the convergence of their yields at $t = 7$s means that most of the corresponding tracer particles are considered ejected in all criteria. Of all our tested criteria, $E + v_{\mathrm{rad}}$ is the physically most motivated, although it has the previously discussed drawback that all the tracer particles outside of the shock radius are not considered ejected, even if they might still become gravitationally

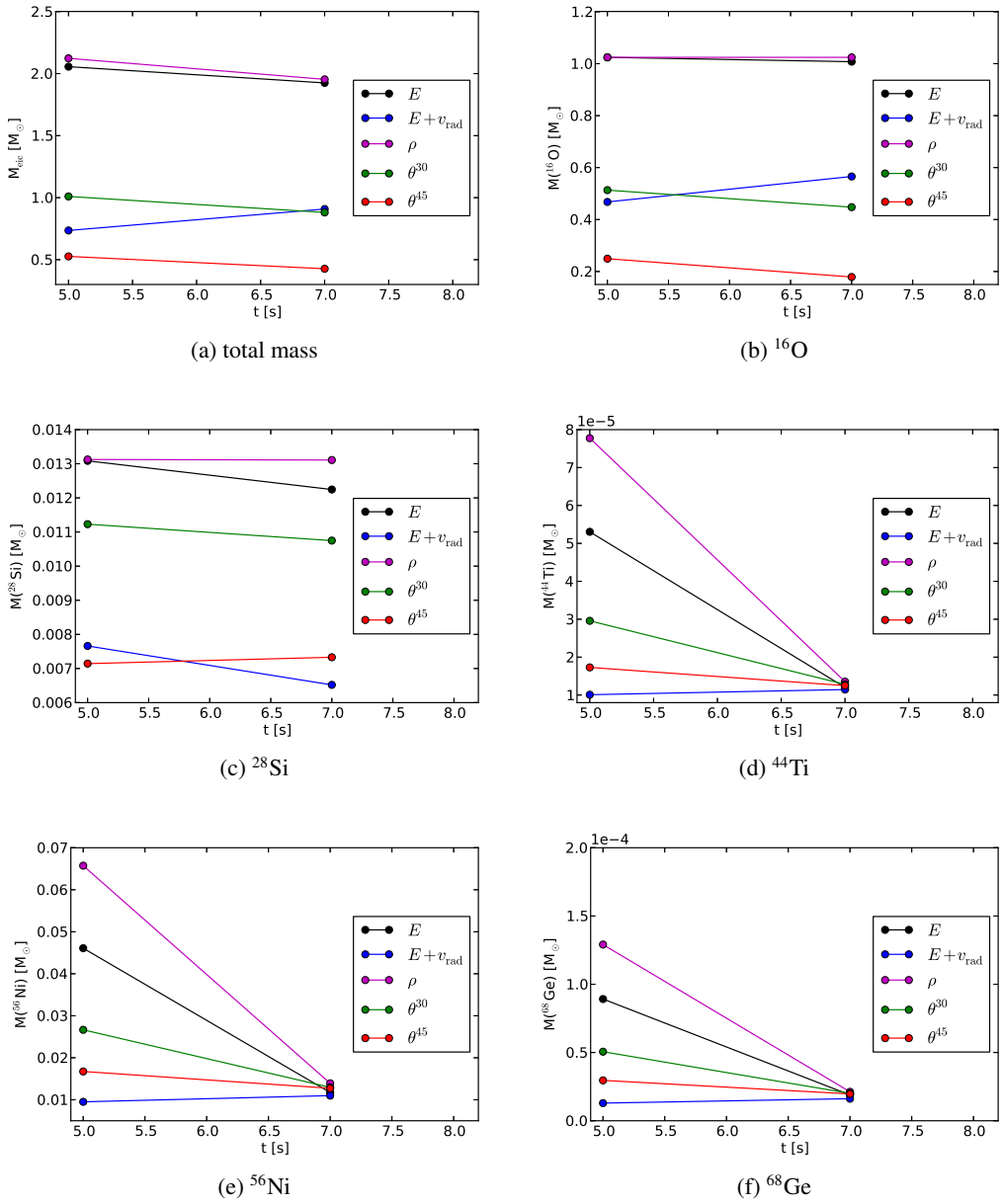

(a) total mass (b) ^{16}O

(c) ^{28}Si (d) ^{44}Ti

(e) ^{56}Ni (f) ^{68}Ge

Figure 7.9: Ejected total mass (a) and yields of several selected isotopes (b)-(f) according to different ejection criteria. See text for explanation.

Crit	M_{ejc} [$M_\odot$]	M(^{16}O) [$M_\odot$]	M(^{28}Si) [$M_\odot$]	M(^{44}Ti) [$M_\odot$]	M(^{56}Ni) [$M_\odot$]
$E(5)$	2.06	1.02	1.31×10^{-2}	5.30×10^{-5}	4.61×10^{-2}
$E(7)$	1.93	1.01	1.22×10^{-2}	1.20×10^{-5}	1.17×10^{-2}
$E + v_{rad}(5)$	0.74	0.47	7.67×10^{-3}	1.01×10^{-5}	9.51×10^{-3}
$E + v_{rad}(7)$	0.91	0.57	6.52×10^{-3}	1.14×10^{-5}	1.10×10^{-2}
$\rho(5)$	2.12	1.02	1.31×10^{-2}	7.77×10^{-5}	6.57×10^{-2}
$\rho(7)$	1.95	1.02	1.31×10^{-2}	1.35×10^{-5}	1.39×10^{-2}
$\theta^{30}(5)$	1.01	0.51	1.12×10^{-2}	2.96×10^{-5}	2.67×10^{-2}
$\theta^{30}(7)$	0.88	0.45	1.07×10^{-2}	1.28×10^{-5}	1.30×10^{-2}
$\theta^{45}(5)$	0.53	0.25	7.14×10^{-3}	1.73×10^{-5}	1.67×10^{-2}
$\theta^{45}(7)$	0.43	0.18	7.33×10^{-3}	1.25×10^{-5}	1.27×10^{-2}

Table 7.4: Total ejecta masses (M_{ejc}) and individual isotopic yields according to different ejection criteria, which are applied at two different times in the simulation (5s and 7s).

unbound at a later point. In order to account for this, we choose a combined final criterion consisting of $E + v_{rad} + \theta^{30}$, i.e., all particles fulfilling either $E + v_{rad}$ or θ^{30} are considered ejected. This can be justified by the notion that all particles with an angle $\theta \geq 30°$ or $\theta \leq -30°$ from the equator will encounter the shock at one point after the end of the simulation and obtain a positive radial velocity. The final positions of the tracers fulfilling $E + v_{rad} + \theta^{30}$ at $t = 7$s are shown in Figure 7.10, together with their peak temperature (right) and the corresponding density (left).

7.2.2 Nucleosynthesis calculation procedure

As the composition of the particles is heavily dependent on their peak temperatures during the simulation (see e.g., Thielemann et al. 1996), we divide them into 20 bins according to their peak temperature in the simulation. Using this method, we are able to make bin-by-bin nucleosynthesis predictions that can be easily applied in the future in order to give estimates also for CCSNe simulations of other progenitors. We choose the $E + v_{rad} + \theta^{30}$ criterion at $t = 7$s, as discussed in the previous section. Table 7.5 lists the number of particles in each temperature bin.

It can be seen that more than half of the ejected particles do not reach a temperature of $T_9 = 1$ (T_9 is a measure of temperature in 10^9 GK), which means that they do not undergo explosive burning and eject material of a composition that is practically unchanged from the pre-collapse composition. For these tracer particles in particular, but to a varying degree also for the tracers in the higher-temperature

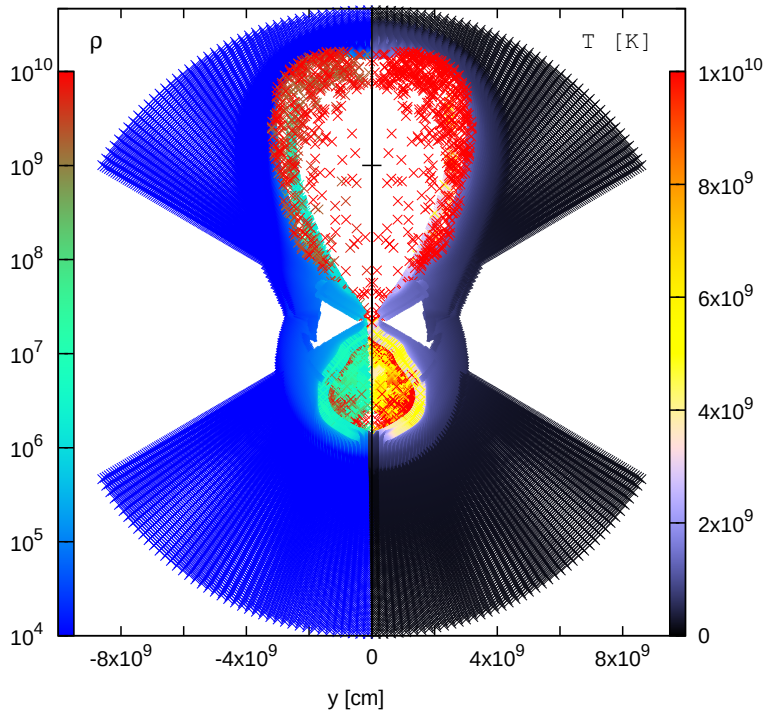

Figure 7.10: Particles fulfilling the $E + v_{\rm rad} + \theta^{30}$ criterion at $t = 7$s. The panel on the right hand side shows the peak temperature (not necessarily at that time), the corresponding density is shown on the left.

bins, the initial abundance composition is very important. We correlate the initial abundances for each particle with the nuclear composition in the progenitor data (Woosley et al. 2002) for the corresponding radius:

$$Y(A,Z)_{trc}(t=0) = Y(A,Z)_{prog}(r = r_{trc,i})\,, \tag{7.2.2}$$

where $Y(A,Z)_{trc}$ and $Y(A,Z)_{prog}$ denote the abundances of nuclear species (A,Z) in the tracer particle and the progenitor, respectively, t is the simulation time, and $r_{trc,i}$ denotes the radius of the tracer particle at $t = 0$. This procedure is applied to all the tracer particles except for the ones in the highest-temperature bin (i.e., with $T_{peak} > 8$ GK), where the initial composition can be derived from nuclear statistical equilibrium (NSE).

The hydrodynamical simulation provides data up to a simulation time $t = 7$ s. In order to make sure that we do not miss any nucleosynthesis processes taking place after that time, we extrapolate for each tracer to the point where the temperature

T_9	N	T_9	N	T_9	N	T_9	N
< 0.8	14096	1.2-1.4	1848	2.4-2.8	727	4.8-5.4	389
0.8-0.9	2038	1.4-1.6	1802	2.8-3.2	356	5.4-6.2	114
0.9-1.0	1616	1.6-1.8	1205	3.2-3.6	213	6.2-7.0	38
1.0-1.1	1441	1.8-2.0	1034	3.6-4.2	305	7.0-8.0	50
1.1-1.2	1221	2.0-2.4	1269	4.2-4.8	196	> 8.0	1416

Table 7.5: Temperature bins and number of ejected tracer particles N in each bin.

drops below 0.01 GK, assuming an expansion with constant velocity. The temperature is calculated at each timestep using the equation of state of Timmes & Swesty (2000). The post-simulation evolution and the input data for the nuclear network are the same as in section 7.1.1.

As the tracer particles from the lower-temperature bins basically expel the unaltered progenitor composition, we do not post-process all the particles from these bins. Instead, we randomly select and post-process a subset from each bin and verify that the ejected composition agrees with the (initial) progenitor composition. Table 7.6 shows the numbers of tracers that have been post-processed for each peak temperature bin.

T_9	N_{pp}	T_9	N_{pp}	T_9	N_{pp}	T_9	N_{pp}
< 0.8	200	1.2-1.4	200	2.4-2.8	400	4.8-5.4	389
0.8-0.9	200	1.4-1.6	200	2.8-3.2	356	5.4-6.2	114
0.9-1.0	200	1.6-1.8	200	3.2-3.6	213	6.2-7.0	38
1.0-1.1	200	1.8-2.0	200	3.6-4.2	305	7.0-8.0	50
1.1-1.2	200	2.0-2.4	400	4.2-4.8	196	> 8.0	1416

Table 7.6: Numbers of randomly selected and post-processed tracer particles (denoted N_{pp}) for each bin.

In total, 5677 tracers have been post-processed, with an emphasis on the tracers in the high-temperature bins. In fact, all of the tracers reaching a peak temperature of at least $T_9 = 2.8$ have been post-processed.

For the low-temperature bins where we do not post-process all the tracers, we calculate the isotopic yields by extrapolating to all tracers in each respective bin taking into account the (individual) mass each tracer particle represents. We do this for each bin by first calculating an average mass fraction for each isotopic species, weighted by the tracer masses, and then multiplying with the total bin mass M_{bin}, gained by summing up the masses of all the tracers in the bin:

$$M_{ejc}^{bin}(A,Z) = \frac{\sum_i X_i(A,Z) M_i}{\sum_i M_i} M_{bin} \,. \tag{7.2.3}$$

Here, $X_i(A, Z)$ is the mass fraction of nucleus (A, Z) and M_i is the mass corresponding to tracer particle i. The sums go over all post-processed tracer particles, while M_{bin} is the sum over all particle masses in the bin. The yields from the individual bins are then added up to obtain the total nuclear yields.

Finally, we account for the fact that the shock will move through the outer layers of the star (which are not included in the computational domain), unbinding material from the helium and hydrogen shells in the process. However, as it has lost a lot of its energy, it does not heat up the material to the temperatures required for explosive nucleosynthesis. Therefore, we add half of the progenitor material starting from an enclosed mass coordinate of 4.07 $M_\odot$ (corresponding to the outer boundary of the computational domain in the simulation) to the ejecta. The factor $1/2$ is derived from the two opening angles of 120°, within which material is considered successfully ejected (see Figure 7.8 left panel). Transferred into a 3D model, this would encompass two solid angles of π sr each, which corresponds to $2\times1/4 = 1/2$ of the star's volume. This procedure adds about 4.885 $M_\odot$ of progenitor material which mainly consists of helium and hydrogen. Note that these considerations inherently lead to the formation of a black hole in the center due to the late accretion onto the PNS, with a mass of about 6 $M_\odot$.

7.2.3 Results

The complete isotopic yields are summarized in Table 7.7. Only isotopes with an ejected mass of at least 10^{-15} $M_\odot$ are included. Note that these are the integrated yields over all ejected particles, as described in section 7.2.2.

In our approach we run each calculation until the temperature drops below 0.01 GK, which means that the calculations for the individual tracer particles do not end at the exact same time. Therefore, the yields in Table 7.7 do not correspond to one specific snapshot in time, which has a significance for unstable isotopes with half-lives of an order $T_{1/2} = 1000$s and shorter. The ^{56}Ni yield of 1.30×10^{-2} $M_\odot$ is very low for a CCSN in this mass range (see e.g., section 7.1.3). Figure 7.9e demonstrates that it is produced in considerably larger amounts (the ρ criterion at 5s indicates 6.57×10^{-2} $M_\odot$ of ejected ^{56}Ni), but the majority of it is accreted onto the PNS in the later stages of the simulation.

Figure 7.11 shows the isotopic [X/Fe] distribution (cf. chapter 3) after decay to stability. Connected data points of the same colour represent different isotopes of the same element. All nuclei with $T_{1/2} < 10^9$ yr are considered to be completely decayed. The solar abundances are from Lodders et al. (2009). The slight over-production of α-elements up to Ti is typical of CCSNe (Thielemann et al., 1996). The high abundances of neutron-deficient isotopes for $Z > 32$ (Ge and beyond) is a clear signature of the νp-process, a mechanism of the rapid proton capture process

Iso	$M/M_\odot$	Iso	$M/M_\odot$	Iso	$M/M_\odot$	Iso	$M/M_\odot$	Iso	$M/M_\odot$
		^{19}Ne	3.28×10^{-11}	^{33}P	9.32×10^{-8}	^{44}K	6.34×10^{-14}	^{49}V	3.92×10^{-6}
^{1}H	2.81×10^{0}	^{20}Ne	2.18×10^{-1}	^{34}P	5.08×10^{-15}	^{45}K	8.60×10^{-15}	^{50}V	6.78×10^{-9}
^{2}H	1.11×10^{-10}	^{21}Ne	2.08×10^{-5}	^{35}P	1.12×10^{-15}	^{39}Ca	4.94×10^{-15}	^{51}V	1.98×10^{-8}
^{3}H	3.00×10^{-12}	^{22}Ne	1.73×10^{-7}	^{27}S	7.27×10^{-12}	^{40}Ca	1.73×10^{-3}	^{52}V	1.13×10^{-11}
^{3}He	7.43×10^{-5}	^{23}Ne	1.96×10^{-12}	^{31}S	5.23×10^{-14}	^{41}Ca	4.39×10^{-6}	^{53}V	7.31×10^{-14}
^{4}He	2.14×10^{0}	^{24}Ne	9.08×10^{-11}	^{32}S	9.66×10^{-3}	^{42}Ca	2.54×10^{-6}	^{54}V	8.76×10^{-15}
^{6}Li	6.48×10^{-11}	^{20}Na	1.63×10^{-11}	^{33}S	1.79×10^{-5}	^{43}Ca	6.44×10^{-7}	^{48}Cr	4.25×10^{-5}
^{7}Li	2.87×10^{-10}	^{21}Na	2.77×10^{-12}	^{34}S	3.49×10^{-6}	^{44}Ca	1.31×10^{-8}	^{49}Cr	3.45×10^{-6}
^{7}Be	1.01×10^{-8}	^{22}Na	4.16×10^{-7}	^{35}S	2.09×10^{-8}	^{45}Ca	1.36×10^{-10}	^{50}Cr	6.31×10^{-6}
^{9}Be	5.47×10^{-11}	^{23}Na	9.96×10^{-6}	^{36}S	8.48×10^{-8}	^{46}Ca	4.55×10^{-12}	^{51}Cr	6.07×10^{-6}
^{10}Be	4.47×10^{-10}	^{24}Na	3.63×10^{-5}	^{37}S	7.06×10^{-13}	^{47}Ca	2.79×10^{-11}	^{52}Cr	5.38×10^{-7}
^{11}Be	8.13×10^{-15}	^{25}Na	2.09×10^{-11}	^{38}S	1.06×10^{-13}	^{48}Ca	1.12×10^{-7}	^{53}Cr	6.20×10^{-8}
^{10}B	4.91×10^{-11}	^{23}Mg	9.72×10^{-13}	^{32}Cl	1.22×10^{-12}	^{49}Ca	2.84×10^{-14}	^{54}Cr	2.03×10^{-7}
^{11}B	9.11×10^{-6}	^{24}Mg	3.48×10^{-2}	^{33}Cl	3.96×10^{-14}	^{40}Sc	9.03×10^{-14}	^{55}Cr	2.41×10^{-12}
^{12}B	4.03×10^{-13}	^{25}Mg	1.59×10^{-5}	^{34}Cl	2.54×10^{-15}	^{41}Sc	1.43×10^{-15}	^{56}Cr	1.20×10^{-11}
^{11}C	3.19×10^{-7}	^{26}Mg	1.84×10^{-7}	^{35}Cl	1.16×10^{-5}	^{42}Sc	1.07×10^{-15}	^{50}Mn	1.10×10^{-15}
^{12}C	1.14×10^{-1}	^{27}Mg	1.04×10^{-9}	^{36}Cl	5.74×10^{-6}	^{43}Sc	4.60×10^{-6}	^{51}Mn	5.88×10^{-6}
^{13}C	8.31×10^{-6}	^{28}Mg	2.06×10^{-8}	^{37}Cl	1.57×10^{-7}	^{44}Sc	1.14×10^{-8}	^{52}Mn	1.48×10^{-5}
^{14}C	6.78×10^{-7}	^{24}Al	2.54×10^{-11}	^{38}Cl	9.99×10^{-11}	^{45}Sc	6.13×10^{-7}	^{53}Mn	9.95×10^{-6}
^{12}N	2.70×10^{-13}	^{25}Al	1.13×10^{-13}	^{39}Cl	6.05×10^{-13}	^{46}Sc	1.16×10^{-9}	^{54}Mn	5.14×10^{-6}
^{13}N	1.92×10^{-8}	^{26}Al	4.16×10^{-7}	^{35}Ar	8.91×10^{-15}	^{47}Sc	1.23×10^{-10}	^{55}Mn	9.11×10^{-7}
^{14}N	2.32×10^{-2}	^{27}Al	2.08×10^{-5}	^{36}Ar	1.98×10^{-3}	^{48}Sc	3.94×10^{-9}	^{56}Mn	1.45×10^{-7}
^{15}N	6.05×10^{-6}	^{28}Al	5.30×10^{-8}	^{37}Ar	7.90×10^{-6}	^{49}Sc	5.79×10^{-9}	^{57}Mn	4.84×10^{-13}
^{16}N	3.46×10^{-10}	^{29}Al	5.34×10^{-10}	^{38}Ar	4.02×10^{-6}	^{50}Sc	2.25×10^{-15}	^{58}Mn	2.55×10^{-15}
^{14}O	5.63×10^{-10}	^{30}Al	4.50×10^{-15}	^{39}Ar	3.39×10^{-8}	^{44}Ti	1.28×10^{-5}	^{59}Mn	1.83×10^{-15}
^{15}O	2.22×10^{-8}	^{27}Si	8.09×10^{-14}	^{40}Ar	3.43×10^{-8}	^{45}Ti	3.05×10^{-6}	^{52}Fe	2.19×10^{-4}
^{16}O	7.38×10^{-1}	^{28}Si	1.52×10^{-2}	^{41}Ar	4.86×10^{-12}	^{46}Ti	5.36×10^{-6}	^{53}Fe	1.01×10^{-6}
^{17}O	1.97×10^{-6}	^{29}Si	1.61×10^{-5}	^{42}Ar	9.19×10^{-12}	^{47}Ti	4.93×10^{-6}	^{54}Fe	7.83×10^{-3}
^{18}O	4.91×10^{-6}	^{30}Si	5.51×10^{-6}	^{36}K	2.86×10^{-13}	^{48}Ti	3.89×10^{-8}	^{55}Fe	1.77×10^{-5}
^{19}O	5.05×10^{-14}	^{31}Si	1.02×10^{-8}	^{37}K	5.23×10^{-15}	^{49}Ti	1.40×10^{-8}	^{56}Fe	7.77×10^{-6}
^{20}O	8.70×10^{-15}	^{32}Si	2.35×10^{-7}	^{38}K	5.43×10^{-7}	^{50}Ti	8.91×10^{-8}	^{57}Fe	6.58×10^{-7}
^{17}F	8.51×10^{-11}	^{28}P	1.49×10^{-12}	^{39}K	1.64×10^{-5}	^{51}Ti	2.04×10^{-13}	^{58}Fe	1.02×10^{-6}
^{18}F	1.15×10^{-5}	^{29}P	7.92×10^{-14}	^{40}K	3.97×10^{-6}	^{52}Ti	2.48×10^{-15}	^{59}Fe	9.20×10^{-8}
^{19}F	8.23×10^{-6}	^{30}P	1.21×10^{-7}	^{41}K	2.12×10^{-8}	^{46}V	1.15×10^{-15}	^{60}Fe	1.90×10^{-6}
^{20}F	3.66×10^{-10}	^{31}P	2.05×10^{-5}	^{42}K	6.13×10^{-10}	^{47}V	3.60×10^{-6}	^{61}Fe	3.68×10^{-14}
^{21}F	9.72×10^{-15}	^{32}P	2.72×10^{-5}	^{43}K	1.39×10^{-11}	^{48}V	3.68×10^{-7}	^{52}Co	1.87×10^{-15}

Iso	M/M$_\odot$	Iso	M/M$_\odot$	Iso	M/M$_\odot$	Iso	M/M$_\odot$	Iso	M/M$_\odot$
^{54}Co	3.97×10^{-13}	^{69}Cu	4.74×10^{-15}	^{72}Ge	1.73×10^{-6}	^{83}Se	6.64×10^{-10}	^{76}Rb	2.30×10^{-12}
^{55}Co	5.34×10^{-5}	^{70}Cu	1.62×10^{-15}	^{73}Ge	3.38×10^{-8}	^{84}Se	2.18×10^{-14}	^{77}Rb	3.19×10^{-10}
^{56}Co	6.54×10^{-5}	^{60}Zn	2.87×10^{-5}	^{74}Ge	2.20×10^{-7}	^{71}Br	1.96×10^{-11}	^{78}Rb	4.75×10^{-11}
^{57}Co	1.30×10^{-5}	^{61}Zn	7.66×10^{-8}	^{75}Ge	2.14×10^{-8}	^{72}Br	2.36×10^{-9}	^{79}Rb	1.62×10^{-10}
^{58}Co	5.91×10^{-6}	^{63}Zn	8.97×10^{-6}	^{76}Ge	4.00×10^{-7}	^{73}Br	6.02×10^{-10}	^{80}Rb	4.79×10^{-12}
^{59}Co	1.16×10^{-6}	^{64}Zn	3.14×10^{-4}	^{77}Ge	5.32×10^{-9}	^{74}Br	2.54×10^{-9}	^{81}Rb	5.08×10^{-9}
^{60}Co	2.16×10^{-6}	^{65}Zn	6.35×10^{-6}	^{78}Ge	4.11×10^{-7}	^{75}Br	2.25×10^{-8}	^{82}Rb	8.32×10^{-9}
^{61}Co	1.14×10^{-7}	^{66}Zn	8.25×10^{-5}	^{67}As	3.70×10^{-9}	^{76}Br	4.96×10^{-8}	^{83}Rb	2.36×10^{-7}
^{62}Co	1.80×10^{-12}	^{67}Zn	4.66×10^{-7}	^{68}As	8.23×10^{-8}	^{77}Br	6.84×10^{-8}	^{84}Rb	1.14×10^{-8}
^{63}Co	4.33×10^{-15}	^{68}Zn	3.37×10^{-6}	^{69}As	1.91×10^{-8}	^{78}Br	7.35×10^{-13}	^{85}Rb	9.11×10^{-8}
^{55}Ni	1.62×10^{-14}	^{69}Zn	9.36×10^{-8}	^{70}As	6.73×10^{-8}	^{79}Br	1.64×10^{-7}	^{86}Rb	2.27×10^{-7}
^{56}Ni	1.30×10^{-2}	^{70}Zn	3.46×10^{-7}	^{71}As	1.34×10^{-7}	^{80}Br	1.57×10^{-10}	^{87}Rb	1.00×10^{-6}
^{57}Ni	2.25×10^{-4}	^{71}Zn	3.69×10^{-15}	^{72}As	5.99×10^{-8}	^{81}Br	2.23×10^{-7}	^{88}Rb	2.75×10^{-10}
^{58}Ni	1.15×10^{-3}	^{72}Zn	2.99×10^{-7}	^{73}As	2.15×10^{-7}	^{82}Br	1.04×10^{-7}	^{89}Rb	4.06×10^{-12}
^{59}Ni	1.27×10^{-4}	^{62}Ga	2.34×10^{-14}	^{74}As	9.92×10^{-9}	^{83}Br	4.75×10^{-8}	^{78}Sr	2.31×10^{-12}
^{60}Ni	1.04×10^{-3}	^{63}Ga	6.53×10^{-9}	^{75}As	1.12×10^{-7}	^{84}Br	2.39×10^{-7}	^{79}Sr	1.61×10^{-11}
^{61}Ni	1.68×10^{-5}	^{64}Ga	1.28×10^{-6}	^{76}As	2.05×10^{-8}	^{85}Br	3.00×10^{-14}	^{80}Sr	1.02×10^{-9}
^{62}Ni	8.54×10^{-5}	^{65}Ga	3.14×10^{-7}	^{77}As	1.57×10^{-8}	^{86}Br	3.84×10^{-14}	^{81}Sr	2.34×10^{-10}
^{63}Ni	4.09×10^{-7}	^{66}Ga	2.34×10^{-6}	^{78}As	3.39×10^{-7}	^{72}Kr	3.22×10^{-12}	^{82}Sr	1.67×10^{-7}
^{64}Ni	2.23×10^{-5}	^{67}Ga	2.43×10^{-6}	^{79}As	2.19×10^{-11}	^{73}Kr	3.44×10^{-12}	^{83}Sr	5.37×10^{-9}
^{65}Ni	3.45×10^{-8}	^{68}Ga	3.62×10^{-8}	^{82}As	2.85×10^{-15}	^{74}Kr	1.60×10^{-9}	^{84}Sr	2.72×10^{-7}
^{66}Ni	2.27×10^{-5}	^{69}Ga	6.83×10^{-7}	^{68}Se	2.92×10^{-8}	^{75}Kr	1.56×10^{-9}	^{85}Sr	2.37×10^{-7}
^{67}Ni	1.86×10^{-15}	^{70}Ga	1.67×10^{-9}	^{69}Se	5.08×10^{-11}	^{76}Kr	1.73×10^{-8}	^{86}Sr	2.95×10^{-7}
^{56}Cu	6.45×10^{-14}	^{71}Ga	9.25×10^{-8}	^{70}Se	2.19×10^{-8}	^{77}Kr	5.95×10^{-9}	^{87}Sr	2.38×10^{-7}
^{57}Cu	4.73×10^{-14}	^{72}Ga	2.52×10^{-8}	^{71}Se	1.09×10^{-8}	^{78}Kr	4.06×10^{-7}	^{88}Sr	7.07×10^{-6}
^{58}Cu	3.87×10^{-12}	^{73}Ga	1.15×10^{-8}	^{72}Se	7.40×10^{-7}	^{79}Kr	3.50×10^{-8}	^{89}Sr	1.05×10^{-8}
^{59}Cu	1.58×10^{-6}	^{74}Ga	2.05×10^{-11}	^{73}Se	5.12×10^{-8}	^{80}Kr	7.84×10^{-7}	^{90}Sr	2.01×10^{-9}
^{60}Cu	2.46×10^{-4}	^{76}Ga	1.68×10^{-15}	^{74}Se	1.64×10^{-6}	^{81}Kr	4.03×10^{-7}	^{91}Sr	2.67×10^{-12}
^{61}Cu	3.80×10^{-5}	^{64}Ge	3.46×10^{-7}	^{75}Se	5.13×10^{-7}	^{82}Kr	3.80×10^{-7}	^{92}Sr	7.58×10^{-13}
^{62}Cu	3.61×10^{-7}	^{65}Ge	7.75×10^{-13}	^{76}Se	2.01×10^{-6}	^{83}Kr	6.42×10^{-8}	^{80}Y	1.50×10^{-12}
^{63}Cu	2.54×10^{-5}	^{66}Ge	1.86×10^{-6}	^{77}Se	3.18×10^{-7}	^{84}Kr	1.45×10^{-6}	^{81}Y	7.61×10^{-12}
^{64}Cu	1.05×10^{-6}	^{67}Ge	2.30×10^{-7}	^{78}Se	3.68×10^{-7}	^{85}Kr	7.46×10^{-7}	^{82}Y	1.42×10^{-13}
^{65}Cu	1.06×10^{-6}	^{68}Ge	2.00×10^{-5}	^{79}Se	4.00×10^{-8}	^{86}Kr	5.80×10^{-6}	^{83}Y	8.20×10^{-12}
^{66}Cu	3.56×10^{-8}	^{69}Ge	6.77×10^{-7}	^{80}Se	1.83×10^{-7}	^{87}Kr	7.04×10^{-10}	^{84}Y	5.52×10^{-14}
^{67}Cu	6.42×10^{-7}	^{70}Ge	1.76×10^{-5}	^{81}Se	6.59×10^{-9}	^{88}Kr	1.14×10^{-10}	^{85}Y	3.38×10^{-10}
^{68}Cu	1.47×10^{-14}	^{71}Ge	1.05×10^{-7}	^{82}Se	1.68×10^{-6}	^{75}Rb	5.04×10^{-13}	^{86}Y	2.66×10^{-9}

Iso	$M/M_\odot$	Iso	$M/M_\odot$	Iso	$M/M_\odot$	Iso	$M/M_\odot$	Iso	$M/M_\odot$
^{87}Y	9.72×10^{-9}	^{90}Zr	3.00×10^{-5}	^{95}Nb	1.15×10^{-10}	^{96}Tc	1.27×10^{-11}	^{98}Pd	4.36×10^{-15}
^{88}Y	2.70×10^{-7}	^{91}Zr	3.80×10^{-8}	^{96}Nb	2.04×10^{-14}	^{97}Tc	2.18×10^{-10}	^{100}Pd	2.59×10^{-15}
^{89}Y	1.67×10^{-6}	^{92}Zr	1.22×10^{-9}	^{97}Nb	4.39×10^{-15}	^{98}Tc	9.96×10^{-13}	^{98}Ag	2.23×10^{-12}
^{90}Y	6.09×10^{-8}	^{93}Zr	1.07×10^{-10}	^{88}Mo	1.60×10^{-13}	^{99}Tc	5.18×10^{-15}	^{99}Ag	2.64×10^{-13}
^{91}Y	7.73×10^{-10}	^{94}Zr	5.04×10^{-11}	^{89}Mo	1.73×10^{-13}	^{92}Ru	3.34×10^{-14}	^{100}Ag	2.03×10^{-14}
^{92}Y	4.21×10^{-12}	^{95}Zr	2.24×10^{-12}	^{90}Mo	1.06×10^{-8}	^{93}Ru	3.49×10^{-15}	^{96}Cd	1.04×10^{-12}
^{93}Y	2.59×10^{-12}	^{96}Zr	8.02×10^{-14}	^{91}Mo	4.24×10^{-10}	^{94}Ru	3.16×10^{-10}	^{97}Cd	8.50×10^{-14}
^{94}Y	1.66×10^{-15}	^{77}Nb	2.71×10^{-14}	^{92}Mo	4.32×10^{-7}	^{95}Ru	4.54×10^{-11}	^{98}Cd	4.58×10^{-12}
^{76}Zr	2.94×10^{-13}	^{78}Nb	1.44×10^{-14}	^{93}Mo	4.89×10^{-8}	^{96}Ru	2.22×10^{-9}	^{99}Cd	4.25×10^{-13}
^{77}Zr	4.11×10^{-13}	^{85}Nb	2.00×10^{-13}	^{94}Mo	2.80×10^{-8}	^{97}Ru	3.48×10^{-12}	^{100}Cd	4.39×10^{-14}
^{78}Zr	4.87×10^{-13}	^{86}Nb	3.67×10^{-13}	^{95}Mo	1.06×10^{-8}	^{98}Ru	1.36×10^{-11}	^{101}Cd	1.57×10^{-15}
^{82}Zr	8.01×10^{-12}	^{87}Nb	1.69×10^{-13}	^{96}Mo	2.77×10^{-10}	^{99}Ru	3.53×10^{-13}	^{97}In	1.37×10^{-13}
^{83}Zr	4.38×10^{-13}	^{88}Nb	8.62×10^{-12}	^{97}Mo	3.30×10^{-12}	^{100}Ru	1.14×10^{-14}	^{98}In	4.07×10^{-12}
^{84}Zr	3.15×10^{-12}	^{89}Nb	1.85×10^{-9}	^{98}Mo	6.75×10^{-14}	^{95}Rh	3.99×10^{-14}	^{99}In	2.69×10^{-13}
^{85}Zr	5.31×10^{-12}	^{90}Nb	8.91×10^{-7}	^{91}Tc	7.09×10^{-14}	^{96}Rh	5.54×10^{-14}	^{100}In	4.25×10^{-14}
^{86}Zr	7.20×10^{-10}	^{91}Nb	4.36×10^{-7}	^{92}Tc	9.00×10^{-12}	^{97}Rh	2.46×10^{-14}	^{101}In	2.34×10^{-15}
^{87}Zr	3.53×10^{-10}	^{92}Nb	1.14×10^{-8}	^{93}Tc	6.62×10^{-10}	^{98}Rh	1.07×10^{-15}	^{99}Sn	7.10×10^{-13}
^{88}Zr	1.92×10^{-7}	^{93}Nb	2.52×10^{-9}	^{94}Tc	1.59×10^{-10}	^{99}Rh	2.20×10^{-13}	^{100}Sn	3.23×10^{-14}
^{89}Zr	3.52×10^{-7}	^{94}Nb	1.23×10^{-9}	^{95}Tc	4.08×10^{-11}	^{96}Pd	8.18×10^{-15}	^{101}Sn	2.33×10^{-15}

Table 7.7: Isotopic yields for the $E + v_{\rm rad} + \theta^{30}$ criterion and with the added material from the outer progenitor layers (see text for explanation). Only isotopes with ejected masses greater than 10^{-15} $M_\odot$ are included.

that allows to bypass the ^{64}Ge waiting point by means of antineutrino captures on free protons, converting them to neutrons which can be captured by ^{64}Ge and other neutron-deficient isotopes (Fröhlich et al., 2006). We would also like to emphasize the efficient production of ^{92}Mo and ^{94}Mo in our calculations, as the origin of these isotopes (along with ^{96}Ru and ^{98}Ru) has been a long-standing puzzle. In general, the ejecta are rather neutron-deficient, with about 70% of the innermost (hottest) ejected particles having an initial Y_e larger than 0.5. The high [^{40}K/Fe] ratio can be explained by its half-life of $T_{1/2} = 1.28 \times 10^9$ yr, which means that we do not consider it decayed in our results.

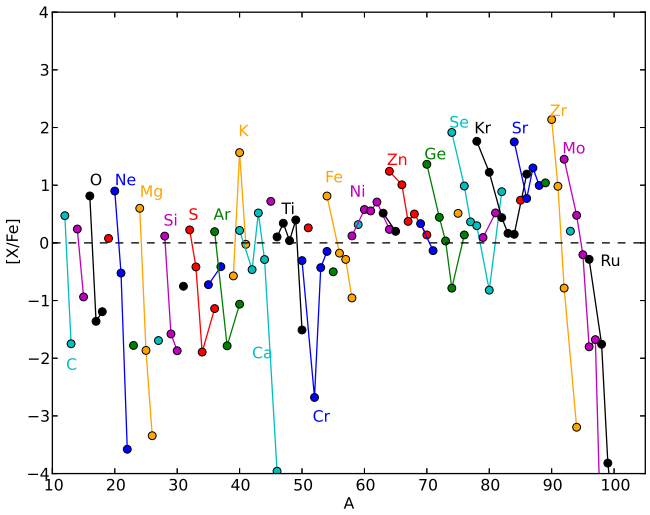

Figure 7.11: Isotopic [X/Fe] values of our 17.0 $M_\odot$ model with the $E + v_{\rm rad} + \theta^{30}$ ejection criterion and added progenitor material from the outer layers (see text), and after the decay of all unstable nuclei with $T_{1/2} < 10^9$ yr. Isotopes of the same element are represented by connected data points of the same colour. The solar abundances are those of Lodders et al. (2009).

7.2.4 11.2 $M_\odot$ progenitor

We are repeating our calculations for the explosion of the s11.2 progenitor model (from the same set from Woosley et al. 2002), which is also discussed in Nakamura et al. (2017). So far, only preliminary results are available. The final positions of the tracer particles fulfilling the ρ criterion reveal a unipolar explosion in positive z-direction (see Figure 7.12). An obvious criterion for ejected particles is to require an angle $\theta \geq +30°$ above the equator (i.e., a much stronger geometric constraint than for the 17.0 $M_\odot$ model), together with the $E + v_{\rm rad}$ condition. The spatial distribution of tracer particles allowed in this prescription is illustrated in Figure 7.13, and the corresponding temperature bin distribution is summarized in Table 7.8.

Although the nucleosynthesis calculations have not been fully performed yet, a comparison of Tables 7.5 and 7.8 allows to make qualitative predictions about the composition of the ejecta in the 11.2 $M_\odot$ case. First, the number of tracers in the $T_9 > 8.0$ bin is significantly larger for the 11.2 $M_\odot$ progenitor than for the 17.0 $M_\odot$ progenitor. One could therefore expect larger yields for the heavy α-nuclei and νp-nuclei. A comparison of the total masses (M_{bin}) of the $T_9 > 8.0$ bins in the two models however reveals that the hottest particles in the 11.2 $M_\odot$ case carry a lower average mass: For the 17.0 $M_\odot$ model $M^{17.0}_{T>8\rm GK} = 3.14 \times 10^{-2}$ $M_\odot$,

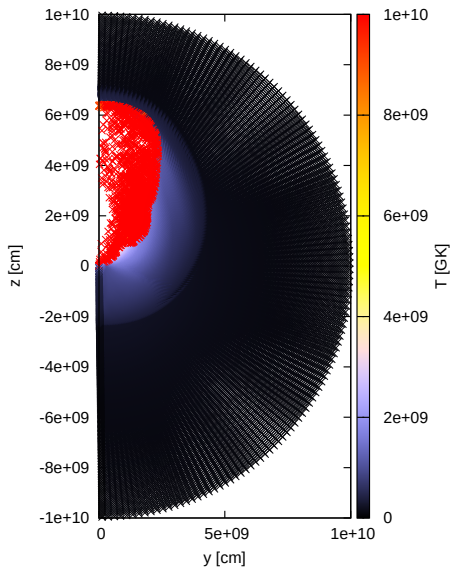

Figure 7.12: Similar to Figure 7.6, but for the ρ criterion and the 11.2 $M_\odot$ model. The positions of the hottest particles (coloured red) indicate a unipolar shock propagation.

T_9	N	T_9	N	T_9	N	T_9	N
< 0.8	17950	1.2-1.4	1068	2.4-2.8	525	4.8-5.4	170
0.8-0.9	1206	1.4-1.6	1142	2.8-3.2	380	5.4-6.2	185
0.9-1.0	1111	1.6-1.8	765	3.2-3.6	380	6.2-7.0	133
1.0-1.1	1073	1.8-2.0	471	3.6-4.2	266	7.0-8.0	38
1.1-1.2	1017	2.0-2.4	649	4.2-4.8	192	> 8.0	1912

Table 7.8: Temperature bins and number of ejected tracer particles N in each bin for the 11.2 $M_\odot$ model.

while the 11.2 $M_\odot$ model yields $M^{11.2}_{T>8\mathrm{GK}} = 1.05 \times 10^{-2}$ $M_\odot$. The choice of θ is more difficult here, as there is a weak shock going in all directions (visible in Figure 7.13). However, it can also be seen that matter behind the shock and close to the center does not fulfil the ejection criterion, as its radial velocity that was temporarily pointing outward has already been turned around at the end of the simulation. We note that the angle of $\theta \geq +30°$ probably represents a lower limit to the ejected mass for the 11.2 $M_\odot$ case.

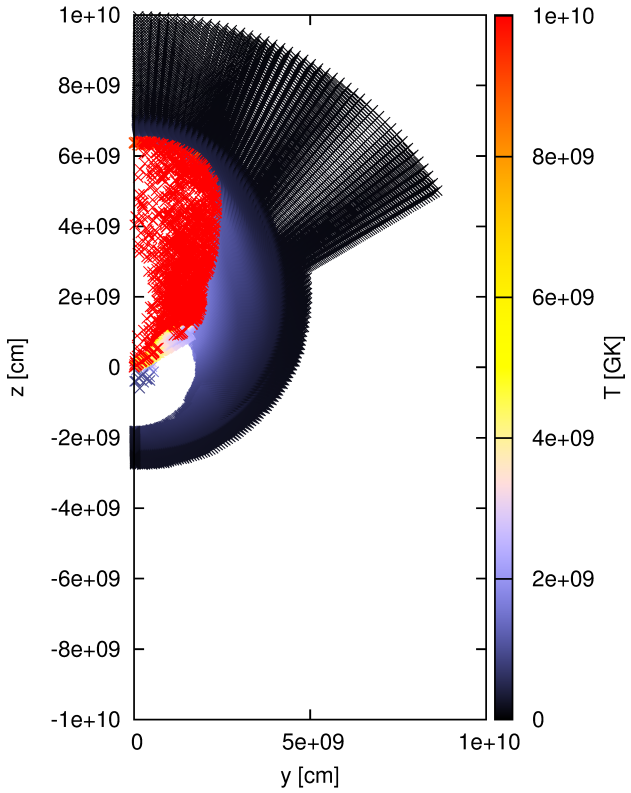

Figure 7.13: Similar to Figure 7.10 (left), but for the 11.2 $M_\odot$ model and only allowing for a positive angle $\theta \geq +30°$.

7.3 Magneto-Hydrodynamically Driven Supernovae

Magneto-hydrodynamically driven (MHD; sometimes also called magnetorotationally driven) SNe are a special class of CCSNe and represent an alternative explosion mechanism to the neutrino-driven SNe. They have been proposed by LeBlanc & Wilson (1970) and revisited in 3D simulations by e.g., Takiwaki et al. (2009); Käppeli (2013). The conceptual idea is that when a differentially rotating star with high magnetic fields collapses, the toroidal magnetic field lines become denser and the magnetic field is amplified due to magnetic flux conservation. Because of the differential rotation, the initially poloidal field lines are wound up along the rotational axis during the collapse and become toroidal, increasing the toroidal field component even further. The ejection of material is powered by the free rotational kinetic energy that is stored in differential rotation, which is defined as the difference between the rotational kinetic energy $T_{\rm rot}$ and the solid-body rotational kinetic energy $T_{\rm rot,solid}$ at the same total angular momentum $L_{\rm tot}$:

$$T_{\rm rot,free} = T_{\rm rot}(L_{\rm tot}) - T_{\rm rot,solid}(L_{\rm tot})\,. \tag{7.3.1}$$

After the stalling of the prompt shock wave, material is accreted, moving through a (hot) shock surface, where the material composition is changed considerably due to photodissociations. Along the inward trajectory, the density also increases, enabling electron captures on free protons and, to a lesser extent, more complex nuclei. The electron captures continue for as long as the material is in the hot and dense region close to the proto-neutron star, leading to a substantial decrease in Y_e. Eventually, neutron-rich material is accelerated and ejected in two high-energy jets at the poles, moving on a spiralling path along the magnetic field lines. The concept is illustrated in Figure 7.14 on the example of three snapshots of a simulation from Käppeli (2013) for a 15 $M_\odot$ progenitor. The entropy per baryon is colour-coded and the magnetic field lines are represented by the white lines. The time values are after core bounce. For this model, Y_e and the asymptotic escape velocity v_∞ are shown in Figure 7.15 for a time 31 ms after core bounce. Note that only zones with positive total energy and positive radial velocity are considered ejected. Since the hydro-code FISH that has been used for this simulation is non-relativistic, the high velocities of $c/4$ achieved in the jets should be considered an upper limit.

Figure 7.15 furthermore shows that the ejected material in the jets is very neutron-rich, with Y_e-values between 0.1 and 0.3. Therefore, the conditions are favourable for the operation of a strong r-process producing material up to and beyond the third r-process peak, which has been shown in Winteler et al. (2012). We have repeated their nucleosynthesis calculations, this time also employing the HFB–14 mass model in addition to the FRDM (1992) model. The results are shown in Figure 7.16. Note that the calculated r-process abundances in MHD SNe generally reproduce the solar r-abundances very well, even around the third peak, in contrast to the shifted peak encountered in NSMs (see chapter 6). This can be explained

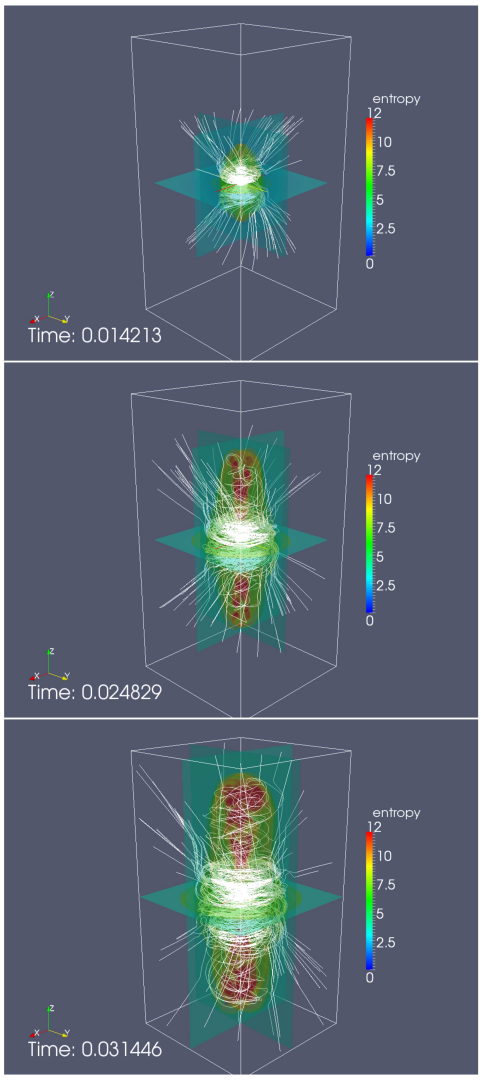

Figure 7.14: MHD SN simulation from Käppeli (2013) depicting the magnetic field lines (white lines) and the entropy per baryon (colours). The three snapshots correspond to different times in the simulation (14 ms, 25 ms, and 31 ms after core bounce). The computational domain is $700 \times 700 \times 1400$ km.

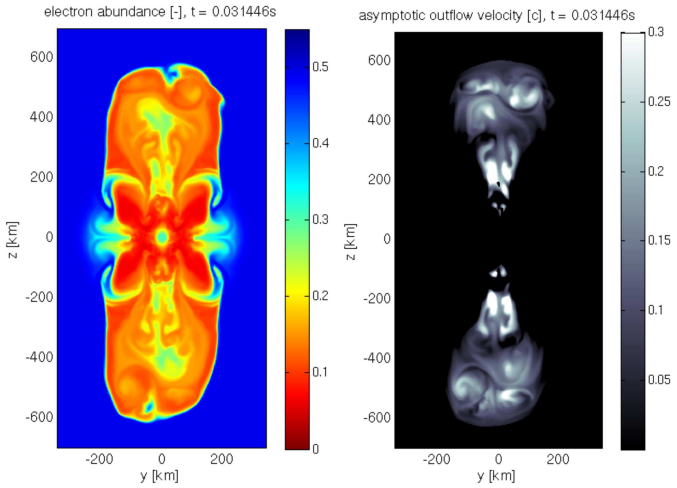

Figure 7.15: Y_e (left) and asymptotic escape velocity (right) in the yz-plane at a post-bounce time of 31 ms for the Käppeli (2013) MHD SN (see also Figure 7.14).

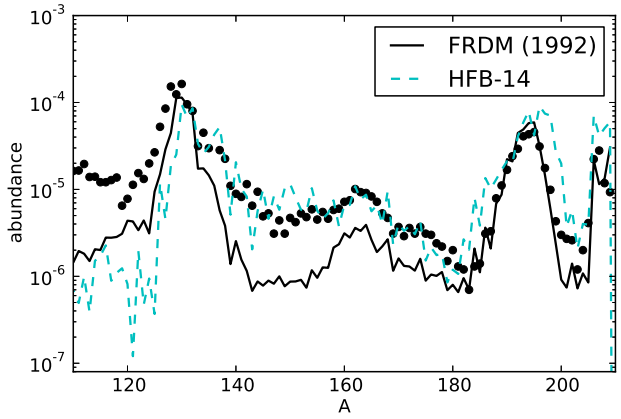

Figure 7.16: R-Process yields for the MHD SN simulation discussed in the text for two mass models (see section 2.4).

by the moderate Y_e, which leads to less fission cycling and in turn to less fission neutrons around the r-process freeze-out.

Käppeli (2013) conclude that the MHD SN mechanism requires extreme conditions in the progenitor with respect to the magnetic field strength and rotation velocity (they use an initial poloidal magnetic field $B_{\rm pol} = 5 \times 10^{12}$ G and an initial ratio of rotational kinetic energy to gravitational binding energy $T_{\rm rot}/|W| \approx 10^{-2}$). Core-collapse progenitors derived from current stellar evolution models generally do not reach these values. However, the low-metallicity progenitors of Woosley & Heger

(2006) achieve high velocities, and the observations of highly magnetized pulsars (*magnetars*) reveal that very large magnetic fields of the order of 10^{15} G are present in some neutron stars in our galaxy. All these considerations lead to the conclusion that if MHD SNe can be realized in nature, they would be very rare, occurring at a rate of about 0.1 – 1 % of all CCSNe. This frequency, coupled with the low Y_e, makes them a very good candidate for the rare r-process site that is needed in order to explain the large scatter in r-process material that is observed in old stars with [Fe/H] < -2 (see Figures 3.1b & 3.2).

Chapter 8

Summary and Conclusions

Over the course of this thesis, the nuclear network WINNET has been extended to run with two new fission fragment distribution models (Kelic et al., 2008; Panov et al., 2008), both of which are considerably more sophisticated than the two previously used models (Panov et al., 2001; Kodama & Takahashi, 1975). The two new models have been applied to r-process calculations in a NSM scenario, with the ABLA07 model especially successful in reproducing the solar second r-process peak. Additional reaction libraries (REACLIB) have been compiled, enabling the use of the ETFSI–Q and HFB–14 mass models in WINNET, as well as introducing two new global sets of β-decays (Marketin et al., 2015; Panov et al., 2015). We have studied the sensitivity of our NSM nucleosynthesis calculations to all these nuclear inputs and reported our findings in Eichler et al. (2015a). One focal point of this work was the position of the third r-process peak, which in comparison to the solar peak is shifted towards higher mass numbers. We found the reason for this behaviour to be late captures of fission neutrons around the freeze-out from (n,γ)–(γ,n) equilibrium. The β-decay predictions of Marketin et al. (2015) are generally faster for nuclei beyond the $N = 126$ shell closure, which accelerates the reaction flux in that region of the nuclear chart and leads to earlier fission and an earlier release of fission neutrons. All neutrons that are captured before the (n,γ)–(γ,n) equilibrium freeze-out do not have an effect on the position of the third peak, and consequently the shift is weakened. There have been several other recent publications underlining the impact of mass models (Mendoza-Temis et al., 2015), fission distribution models (Goriely et al., 2013; Goriely, 2015a) as well as β-decays (see e.g., Lorusso et al. 2015) on r-process nucleosynthesis.

We have included a short chapter on the problems involved with NSMs as r-process sites in the early galaxy, and the possible solution presented by MHD SNe that generate two jets ejecting neutron-rich matter. The low expected frequency of these events matches the observed scatter in the [Eu/Fe] values of metal-poor stars well.

Furthermore, we have performed CCSN nucleosynthesis calculations for the PUSH calibration study (Perego et al., 2015), where we compared our $^{56-58}$Ni and ^{44}Ti yields for a wide range of PUSH parameters and progenitors in the 18 − 21 $M_\odot$ bracket to the observed values of SN 1987A. These considerations revealed the necessity for a late fallback of about 0.1 $M_\odot$ in order to match our $^{56-58}$Ni masses with the observations, which is fully consistent with observational constraints form SN 1987A and explicit fallback calculations for progenitors in this mass range (Chevalier, 1989; Ugliano et al., 2012). However, the ejected ^{44}Ti mass in all our models is too low, confirming a long-standing problem of reproducing this observable in SN 1987A. The fallback necessary to match the other observables has a particularly damaging effect on the ^{44}Ti yield, as it is synthesized in the innermost zones of the ejecta. As we have shown, the yield can be increased when homogeneous mixing of the ejecta is assumed after the mass cut is determined, but before the fallback is applied. Margerin et al. (2014) reported on a new experimentally determined upper limit for the ^{44}Ti$(\alpha, p)^{47}$V reaction, the main destruction channel of ^{44}Ti. Adapting the new (upper limit) ^{44}Ti$(\alpha, p)^{47}$V rate, we have found an increase by about 45 % for the ejected ^{44}Ti mass. In addition, we have investigated the dependence of the ^{57}Ni and ^{58}Ni yields on the mass cut and the position of the boundary between the Si shell to the O shell in the progenitor. As $Y_e < 0.5$ in the Si shell (due to the presence of small amounts of ^{54}Fe) for the progenitors considered here, the synthesis of the slightly neutron-rich isotopes ^{57}Ni and ^{58}Ni is facilitated. From our sample only the 18.0 $M_\odot$ and the 19.4 $M_\odot$ had parts of their Si shells ejected.

The last part of my thesis was dedicated to nucleosynthesis calculations of 2D CCSN long-term simulations from Nakamura et al. (2017). So far, detailed results are only available for the 17.0 $M_\odot$ model. We have carefully studied the implications of five different ejection criteria on the nuclear yields and chosen to assume successful ejection for particles that fulfil $E > 0, v_{\rm rad} > 0$, or $|\theta| \geq 30°$, where θ is the angle measured from the equator. This geometric criterion has been made necessary by the fact that the first requirement does not include particles that have not encountered the shock at the time when the simulation stops, but are expected to do so at a later moment (see Figures 7.6 & 7.7). We have shown that the yields of the heavier α-elements do not greatly depend on the ejection criterion, and find that the ejected mass of ^{56}Ni in our calculations is remarkably low. The results for the SN of the 11.2 $M_\odot$ progenitor will show if this is an anomaly caused by the progenitor structure, or a characteristic of the hydrodynamical simulations. The composition of the final ejecta has a richness of neutron-deficient isotopes of elements with $Z \geq 32$, a trademark of the νp-process (Fröhlich et al., 2006).

Bibliography

Abbott, B. P., Abbott, R., Abbott, T. D., Abernathy, M. R., Acernese, F., Ackley, K., Adams, C., Adams, T., Addesso, P., & Adhikari, et al., R. X. 2016, Physical Review Letters, 116, 061102

Aboussir, Y., Pearson, J. M., Dutta, A. K., & Tondeur, F. 1995, Atomic Data and Nuclear Data Tables, 61, 127

Arcones, A. & Janka, H.-T. 2011, A&A, 526, A160

Arcones, A., Janka, H.-T., & Scheck, L. 2007, A&A, 467, 1227

Arcones, A. & Martínez-Pinedo, G. 2011, PhysRevC, 83, 045809

Argast, D., Samland, M., Thielemann, F.-K., & Qian, Y.-Z. 2004, A&A, 416, 997

Arlandini, C., Käppeler, F., Wisshak, K., Gallino, R., Lugaro, M., Busso, M., & Straniero, O. 1999, ApJ, 525, 886

Arnett, W. D., Bahcall, J. N., Kirshner, R. P., & Woosley, S. E. 1989, ARA & A, 27, 629

Arnould, M. & Goriely, S. 2003, Physics Reports, 384, 1

Audi, G., Wapstra, A., & Thibault, C. 2003, Nuclear Physics A, 729, 337 , the 2003 {NUBASE} and Atomic Mass Evaluations

Banerjee, P., Haxton, W. C., & Qian, Y.-Z. 2011, Physical Review Letters, 106, 201104

Bardeen, J., Cooper, L. N., & Schrieffer, J. R. 1957, Phys. Rev., 106, 162

Bauswein, A., Goriely, S., & Janka, H.-T. 2013, ApJ, 773, 78

Beloborodov, A. M. 2008, AIP Conference Proceedings: Cool Disks, Hot Flows: The Varying Faces of Accreting Compact Objects, 1054, 51

Benlliure, J., Grewe, A., de Jong, M., Schmidt, K.-H., & Zhdanov, S. 1998, Nucl. Phys. A, 628, 458

Bernal, C. G., Page, D., & Lee, W. H. 2013, ApJ, 770, 106

Bethe, H. A. 1990, Reviews of Modern Physics, 62, 801

Bethe, H. A. & Bacher, R. F. 1936, Rev. Mod. Phys., 8, 82

Blinnikov, S., Lundqvist, P., Bartunov, O., Nomoto, K., & Iwamoto, K. 2000, ApJ, 532, 1132

Brack, M., Damgaard, J., Jensen, A. S., Pauli, H. C., Strutinsky, V. M., & Wong, C. Y. 1972, Reviews of Modern Physics, 44, 320

Burbidge, E. M., Burbidge, G. R., Fowler, W. A., & Hoyle, F. 1957, Reviews of Modern Physics, 29, 547

Cameron, A. G. W. 1957, PASP, 69, 201

Chen, B., Dobaczewski, J., Kratz, K.-L., Langanke, K., Pfeiffer, B., Thielemann, F.-K., & Vogel, P. 1995, Physics Letters B, 355, 37

Chevalier, R. A. 1989, ApJ, 346, 847

Chiappini, C., Matteucci, F., & Romano, D. 2001, ApJ, 554, 1044

Chieffi, A. & Limongi, M. 2013, ApJ, 764, 21

Chugai, N. N., Chevalier, R. A., Kirshner, R. P., & Challis, P. M. 1997, ApJ, 483, 925

Colgate, S. A. & White, R. H. 1966, ApJ, 143, 626

Cowan, J. J., Thielemann, F.-K., & Truran, J. W. in preparation

Dessart, L., Ott, C. D., Burrows, A., Rosswog, S., & Livne, E. 2009, ApJ, 690, 1681

Eichler, M., Arcones, A., Käppeli, R., Korobkin, O., Liebendörfer, M., Martinez-Pinedo, G., Panov, I. V., Rauscher, T., Rosswog, S., Thielemann, F.-K., & Winteler, C. 2016, Journal of Physics: Conference Series, 665, 012054

Eichler, M., Arcones, A., Kelic, A., Korobkin, O., Langanke, K., Marketin, T., Martinez-Pinedo, G., Panov, I., Rauscher, T., Rosswog, S., Winteler, C., Zinner, N. T., & Thielemann, F.-K. 2015a, ApJ, 808, 30

Eichler, M., Arcones, A., & Thielemann, F.-K. 2012, Proceedings: Nuclei in the Cosmos XII, 103

Eichler, M., Perego, A., Hempel, M., Fröhlich, C., Ebinger, E., Casanova, J., Liebendörfer, M., & Thielemann, F.-K. 2015b, Proceedings: Nuclear Physics in Astrophysics VII, in press

Epstein, R. I., Colgate, S. A., & Haxton, W. C. 1988, Physical Review Letters, 61, 2038

Fernández, R. & Metzger, B. D. 2013a, MNRAS, 435, 502

—. 2013b, ApJ, 763, 108

Fischer, T., Whitehouse, S. C., Mezzacappa, A., Thielemann, F.-K., & Liebendörfer, M. 2010, A&A, 517, A80

Fong, P. 1956, Physical Review, 102, 434

Fowler, W. A., Caughlan, G. R., & Zimmerman, B. A. 1967, ARA&A, 5, 525

Fraija, N., Bernal, C. G., & Hidalgo-Gaméz, A. M. 2014, MNRAS, 442, 239

Fransson, C. & Kozma, C. 2002, New Astronomy Review, 46, 487

Freiburghaus, C., Rosswog, S., & Thielemann, F.-K. 1999, ApJL, 525, L121

Fröhlich, C., Hauser, P., Liebendörfer, M., Martínez-Pinedo, G., Thielemann, F.-K., Bravo, E., Zinner, N. T., Hix, W. R., Langanke, K., Mezzacappa, A., & Nomoto, K. 2006, ApJ, 637, 415

Fuller, G. M., Fowler, W. A., & Newman, M. J. 1980, ApJ Suppl., 42, 447

—. 1982, ApJ Suppl., 48, 279

—. 1985, ApJ, 293, 1

Gadioli, E. & Hodgson, P. E. 1992, Pre-Equilibrium Nuclear Reactions (Clarendon Press, Oxford)

Gaimard, J.-J. & Schmidt, K.-H. 1991, Nucl. Phys. A, 531, 709

Goriely, S. 2015a, The European Physical Journal A, 51

—. 2015b, Nuclear Physics A, 933, 68

Goriely, S., Bauswein, A., & Janka, H.-T. 2011, ApJL, 738, L32

Goriely, S., Bauswein, A., Just, O., Pllumbi, E., & Janka, H.-T. 2015, MNRAS, 452, 3894

Goriely, S., Hilaire, S., & Koning, A. J. 2008, A&A, 487, 767

Goriely, S., Hilaire, S., Koning, A. J., Sin, M., & Capote, R. 2009, Phys. Rev. C, 79, 024612

Goriely, S., Samyn, M., & Pearson, J. M. 2007, Phys. Rev. C, 75, 064312

Goriely, S., Sida, J.-L., Lemaître, J.-F., Panebianco, S., Dubray, N., Hilaire, S., Bauswein, A., & Janka, H.-T. 2013, Physical Review Letters, 111, 242502

Grebenev, S. A., Lutovinov, A. A., Tsygankov, S. S., & Winkler, C. 2012, Nature, 490, 373

Grefenstette, B. W., Harrison, F. A., Boggs, S. E., Reynolds, S. P., Fryer, C. L., Madsen, K. K., Wik, D. R., Zoglauer, A., Ellinger, C. I., Alexander, D. M., An, H., Barret, D., Christensen, F. E., Craig, W. W., Forster, K., Giommi, P., Hailey, C. J., Hornstrup, A., Kaspi, V. M., Kitaguchi, T., Koglin, J. E., Mao, P. H., Miyasaka, H., Mori, K., Perri, M., Pivovaroff, M. J., Puccetti, S., Rana, V., Stern, D., Westergaard, N. J., & Zhang, W. W. 2014, Nature, 506, 339

Grossman, D., Korobkin, O., Rosswog, S., & Piran, T. 2014, MNRAS, 439, 757

Hahn, O. & Strassmann, F. 1939, Naturwissenschaften, 27, 11

Handy, T., Plewa, T., & Odrzywołek, A. 2014, ApJ, 783, 125

Hix, W. R. & Thielemann, F.-K. 1999, Journal of Computational and Applied Mathematics, 109, 321

Honda, S., Aoki, W., Ishimaru, Y., & Wanajo, S. 2007, ApJ, 666, 1189

Hüdepohl, L., Müller, B., Janka, H.-T., Marek, A., & Raffelt, G. G. 2010, Physical Review Letters, 104, 251101

Iliadis, C. 2007, Nuclear Physics of Stars (Wiley-VCH Verlag)

Jerkstrand, A., Fransson, C., & Kozma, C. 2011, A & A, 530, A45

Just, O., Bauswein, A., Pulpillo, R. A., Goriely, S., & Janka, H.-T. 2015, MNRAS, 448, 541

Käppeli, R. Y. 2013, PhD thesis, Universität Basel

Kelic, A., Ricciardi, M. V., & Schmidt, K.-H. 2008, Proceedings: Dynamical Aspects of Nuclear Fission, World Scientific, 6, 203

Kelic, A., Valentina Ricciardi, M., & Schmidt, K.-H. 2009, ArXiv e-prints

Kodama, T. & Takahashi, K. 1975, NuPhA, 239, 489

Korobkin, O., Rosswog, S., Arcones, A., & Winteler, C. 2012, MNRAS, 426, 1940

Kozma, C. & Fransson, C. 1998a, ApJ, 496, 946

—. 1998b, ApJ, 497, 431

Kratz, K.-L., Farouqi, K., & Möller, P. 2014, ApJ, 792, 6

Larsson, J., Fransson, C., Östlin, G., Gröningsson, P., Jerkstrand, A., Kozma, C., Sollerman, J., Challis, P., Kirshner, R. P., Chevalier, R. A., Heng, K., McCray, R., Suntzeff, N. B., Bouchet, P., Crotts, A., Danziger, J., Dwek, E., France, K., Garnavich, P. M., Lawrence, S. S., Leibundgut, B., Lundqvist, P., Panagia, N., Pun, C. S. J., Smith, N., Sonneborn, G., Wang, L., & Wheeler, J. C. 2011, Nature, 474, 484

Lattimer, J. M. & Schramm, D. N. 1974, ApJL, 192, L145

LeBlanc, J. M. & Wilson, J. R. 1970, ApJ, 161, 541

Lee, W. H., Ramirez-Ruiz, E., & López-Cámara, D. 2009, ApJL, 699, L93

Limongi, M. & Chieffi, A. 2006, ApJ, 647, 483

Lodders, K., Palme, H., & Gail, H.-P. 2009, Landolt Börnstein

Lorusso, G., Nishimura, S., Xu, Z. Y., et al. 2015, Physical Review Letters, 114, 192501

Mamdouh, A., Pearson, J. M., Rayet, M., & Tondeur, F. 1998, Nuclear Physics A, 644, 389

Margerin, V., Murphy, A. S. J., Davinson, T., Dressler, R., Fallis, J., Kankainen, A., Laird, A. M., Lotay, G., Mountford, D. J., Murphy, C. D., Seiffert, C., Schumann, D., Stowasser, T., Stora, T., Wang, C. H.-T., & Woods, P. J. 2014, Physics Letters B, 731, 358

Marketin, T., Huther, L., & Martínez-Pinedo, G. 2015, ArXiv e-prints:1507.07442

Martin, D., Perego, A., Arcones, A., Thielemann, F.-K., Korobkin, O., & Rosswog, S. 2015, ApJ, 813, 2

Martínez-Pinedo, G., Fischer, T., Lohs, A., & Huther, L. 2012, Physical Review Letters, 109, 251104

Martínez-Pinedo, G., Kelic, A., Langanke, K., Schmidt, K.-H., Mocelj, D., Fröhlich, C., Thielemann, F.-K., Panov, I., Rauscher, T., Liebendörfer, M., Zinner, N. T., Pfeiffer, B., Buras, R., & Janka, H.-T. 2006, Proceedings of the International Symposium on Nuclear Astrophysics - Nuclei in the Cosmos, IX, 64

Mathews, G. J., Mengoni, A., Thielemann, F.-K., & Fowler, W. A. 1983, ApJ, 270, 740

Matteucci, F., Romano, D., Arcones, A., Korobkin, O., & Rosswog, S. 2014, MNRAS, 438, 2177

Mayer, M. G. 1949, Physical Review, 75, 1969

Mendoza-Temis, J. d. J., Wu, M.-R., Langanke, K., Martínez-Pinedo, G., Bauswein, A., & Janka, H.-T. 2015, Phys. Rev. C, 92, 055805

Metzger, B. D., Arcones, A., Quataert, E., & Martínez-Pinedo, G. 2010a, MNRAS, 402, 2771

Metzger, B. D., Martínez-Pinedo, G., Darbha, S., Quataert, E., Arcones, A., Kasen, D., Thomas, R., Nugent, P., Panov, I. V., & Zinner, N. T. 2010b, MNRAS, 406, 2650

Metzger, B. D., Piro, A. L., & Quataert, E. 2008, MNRAS, 390, 781

Meyer, B. S. 1989, ApJ, 343, 254

Meyer, B. S., Mathews, G. J., Howard, W. M., Woosley, S. E., & Hoffman, R. D. 1992, ApJ, 399, 656

Möller, P., Madland, D. G., Sierk, A. J., & Iwamoto, A. 2001, Nature, 409, 785

Möller, P., Myers, W. D., Sagawa, H., & Yoshida, S. 2012, Physical Review Letters, 108, 052501

Möller, P., Nix, J. R., & Kratz, K.-L. 1997, Atomic Data and Nuclear Data Tables, 66, 131

Möller, P., Nix, J. R., Myers, W. D., & Swiatecki, W. J. 1995, Atomic Data and Nuclear Data Tables, 59, 185

Möller, P., Pfeiffer, B., & Kratz, K.-L. 2003, Phys. Rev. C, 67, 055802

Möller, P., Sierk, A. J., Ichikawa, T., & Sagawa, H. 2016, Atomic Data and Nuclear Data Tables, 109, 1

Mumpower, M. R., McLaughlin, G. C., & Surman, R. 2012, Phys. Rev. C, 86, 035803

Myers, W. D. & Swiatecki, W. J. 1969, Annals of Physics, 55, 395

—. 1974, Annals of Physics, 84, 186

—. 1999, Phys. Rev. C, 60, 014606

Nakamura, K., Takiwaki, T., Kuroda, T., & Kotake, K. 2015, PASJ

Nakamura et al. 2017, in preparation

Ning, H., Qian, Y.-Z., & Meyer, B. S. 2007, ApJL, 667, L159

NuDat2. 2009, National Nuclear Data Center, information extracted from the NuDat 2 database, URL http://www.nndc.bnl.gov/nudat2/

O'Connor, E. & Ott, C. D. 2011, ApJ, 730, 70

Otsuki, K., Tagoshi, H., Kajino, T., & y. Wanajo, S. 2000, ApJ, 533, 424

Panov, I. V., Freiburghaus, C., & Thielemann, F.-K. 2001, Nuclear Physics A, 688, 587

Panov, I. V., Kolbe, E., Pfeiffer, B., Rauscher, T., Kratz, K.-L., & Thielemann, F.-K. 2005, Nuclear Physics A, 747, 633

Panov, I. V., Korneev, I. Y., Rauscher, T., Martínez-Pinedo, G., Kelić-Heil, A., Zinner, N. T., & Thielemann, F.-K. 2010, A&A, 513, A61

Panov, I. V., Korneev, I. Y., & Thielemann, F.-K. 2008, Astronomy Letters, 34, 189

Panov, I. V., Lutostansky, Y. S., & Thielemann, F. K. 2015, Bull. Russ. Acad. Sci. Phys., 79, 437

Pearson, J. M., Nayak, R. C., & Goriely, S. 1996, Physics Letters B, 387, 455

Perego, A., Hempel, M., Fröhlich, C., Ebinger, K., Eichler, M., Casanova, J., Liebendörfer, M., & Thielemann, F.-K. 2015, ApJ, 806, 275

Perego, A., Rosswog, S., Cabezón, R. M., Korobkin, O., Käppeli, R., Arcones, A., & Liebendörfer, M. 2014, MNRAS, 443, 3134

Petermann, I., Langanke, K., Martínez-Pinedo, G., Panov, I. V., Reinhard, P.-G., & Thielemann, F.-K. 2012, European Physical Journal A, 48, 122

Piran, T., Korobkin, O., & Rosswog, S. 2014, ArXiv e-prints: [1401.2166]

Podsiadlowski, P., Morris, T. S., & Ivanova, N. 2007, in American Institute of Physics Conference Series, Vol. 937, Supernova 1987A: 20 Years After: Supernovae and Gamma-Ray Bursters, ed. S. Immler, K. Weiler, & R. McCray, 125–133

Rauscher, T. 2011, International Journal of Modern Physics E, 20, 1071

Rauscher, T., Heger, A., Hoffman, R. D., & Woosley, S. E. 2002, ApJ, 576, 323

Rauscher, T. & Thielemann, F.-K. 2000, Atomic Data and Nuclear Data Tables, 75, 1

Roberts, L. F., Kasen, D., Lee, W. H., & Ramirez-Ruiz, E. 2011, ApJL, 736, L21

Roberts, L. F., Reddy, S., & Shen, G. 2012, Phys. Rev. C, 86, 065803

Roederer, I. U. 2013, AJ, 145, 26

Roederer, I. U., Lawler, J. E., Sobeck, J. S., Beers, T. C., Cowan, J. J., Frebel, A., Ivans, I. I., Schatz, H., Sneden, C., & Thompson, I. B. 2012, ApJS, 203, 27

Rosswog, S., Korobkin, O., Arcones, A., Thielemann, F.-K., & Piran, T. 2014, MNRAS, 439, 744

Rosswog, S., Piran, T., & Nakar, E. 2013, MNRAS, 430, 2585

Schenk, O. & Gärtner, K. 2004, Future Generation Computer Systems, 20, 475 , selected numerical algorithms

Schmidt, K.-H., Kelić, A., & Ricciardi, M. V. 2008, EPL (Europhysics Letters), 83, 32001

Seeger, P. A., Fowler, W. A., & Clayton, D. D. 1965, ApJS, 11, 121

Seitenzahl, I. R., Timmes, F. X., & Magkotsios, G. 2014, ApJ, 792, 10

Shibagaki, S., Kajino, T., Mathews, G. J., Chiba, S., Nishimura, S., & Lorusso, G. 2015, ArXiv e-prints

Shigeyama, T. & Nomoto, K. 1990, ApJ, 360, 242

Simmerer, J., Sneden, C., Cowan, J. J., Collier, J., Woolf, V. M., & Lawler, J. E. 2004, ApJ, 617, 1091

Sneden, C. & Cowan, J. J. 2003, Science, 299, 70

Sneden, C., Cowan, J. J., & Gallino, R. 2008, Ann.Rev.Astron.Astrophys., 46, 241

Spitoni, E., Matteucci, F., Recchi, S., Cescutti, G., & Pipino, A. 2009, A&A, 504, 87

Steinberg, E. P. & Wilkins, B. D. 1978, ApJ, 223, 1000

Strutinsky, V. M. 1967, Nuclear Physics A, 95, 420

—. 1968, Nuclear Physics A, 122, 1

Takiwaki, T., Kotake, K., & Sato, K. 2009, ApJ, 691, 1360

Tanvir, N. R., Levan, A. J., Fruchter, A. S., Hjorth, J., Hounsell, R. A., Wiersema, K., & Tunnicliffe, R. L. 2013, Nature, 500, 547

Tatsuda, S., Hashizume, K., Wada, T., Ohta, M., Sumiyoshi, K., Otsuki, K., Kajino, T., Koura, H., Chiba, S., & Aritomo, Y. 2007, in American Institute of Physics Conference Series, Vol. 891, Tours Symposium on Nuclear Physics VI, ed. M. Arnould, M. Lewitowicz, H. Emling, H. Akimune, M. Ohta, H. Utsunomiya, T. Wada, & T. Yamagata, 423–426

Thielemann, F.-K., Hashimoto, M.-A., & Nomoto, K. 1990, ApJ, 349, 222

Thielemann, F.-K., Nomoto, K., & Hashimoto, M.-A. 1996, ApJ, 460, 408

Timmes, F. X. & Swesty, F. D. 2000, ApJS, 126, 501

Travaglio, C., Röpke, F. K., Gallino, R., & Hillebrandt, W. 2011, ApJ, 739, 93

Ugliano, M., Janka, H.-T., Marek, A., & Arcones, A. 2012, ApJ, 757, 69

Umeda, H. & Nomoto, K. 2002, ApJ, 565, 385

—. 2008, ApJ, 673, 1014

Utrobin, V. P. & Chugai, N. N. 2005, A & A, 441, 271

Wanajo, S., Sekiguchi, Y., Nishimura, N., Kiuchi, K., Kyutoku, K., & Shibata, M. 2014, ArXiv e-prints

Wehmeyer, B., Pignatari, M., & Thielemann, F.-K. 2015, MNRAS, 452, 1970

Wilkins, B. D., Steinberg, E. P., & Chasman, R. R. 1976, Phys. Rev. C, 14, 1832

Wilson, J. R. 1985, in Numerical Astrophysics, ed. J. M. Centrella, J. M. Leblanc, & R. L. Bowers, 422

Winteler, C. 2011, PhD thesis, University of Basel

Winteler, C., Käppeli, R., Perego, A., Arcones, A., Vasset, N., Nishimura, N., Liebendörfer, M., & Thielemann, F.-K. 2012, ApJL, 750, L22

Woosley, S. E. 1988, ApJ, 330, 218

Woosley, S. E. & Heger, A. 2006, ApJ, 637, 914

Woosley, S. E., Heger, A., & Weaver, T. A. 2002, Reviews of Modern Physics, 74, 1015

Woosley, S. E. & Howard, W. M. 1978, ApJS, 36, 285

Woosley, S. E. & Weaver, T. A. 1995, ApJS, 101, 181